TÉCNICO LISBOA

Numerical Investigation on the Comparability of Simulations and Experiments at the NACA 64418 Airfoil

Miguel Afonso Antunes

Thesis to obtain the Master of Science Degree in

Aerospace Engineering

Supervisors: M.Sc. Maximilian Ehrle
Prof. Luís Rego da Cunha de Eça

Examination Committee

Chairperson: Prof. Fernando José Parracho Lau
Supervisor: Prof. Luís Rego da Cunha de Eça
Member of the Committee: Prof. João Manuel Ribeiro Costa Baltazar

January 2021

TÉCNICO LISBOA

University of Stuttgart
Germany

Numerical Investigation on the Comparability of Simulations and Experiments at the NACA 64418 Airfoil

Miguel Afonso Antunes

Thesis to obtain the Master of Science Degree in

Aerospace Engineering

Supervisors: M.Sc. Maximilian Ehlre
Prof. Luís Rego da Cunha de Eça

Examination Committee

Chairperson: Prof. Fernando José Parracho Lau
Supervisor: Prof. Luís Rego da Cunha de Eça
Member of the Committee: Prof. João Manuel Ribeiro Costa Baltazar

January 2021

To my mother.

To my father.

To my grandmother, Maria.

And to my grandfather, José.

Acknowledgments

Above all, I would like to acknowledge Maximilian Ehrle, my supervisor at the IAG, for giving me the opportunity to write my master's thesis there and allowing me to work by my own while still pointing me in the right direction. I also thank him for making me feel welcome in Germany since the first day, for all his continuous patience when addressing my doubts and for everything that he taught me. I would also like to thank Prof. Luís Eça, my supervisor at IST, for all the useful advice and helpful comments.

I am grateful to the IAG, for providing the computational tools necessary for this work and to the Laminar Wind Tunnel group that was involved in the experimental measurements and post processing of the data used in this thesis.

I am also grateful for the financial support provided by the Erasmus+ program.

I thank all my friends that supported me throughout the way. A special thank you to my dear friends Inês and Francisco, for all the laughs and conversations that made everything easier, especially when stress levels were high.

To Laura, for her unceasing support and all the moments we shared that helped shaping this journey into a one of a kind. A thank you to her family as well for all their kindness and for always making me feel home.

Lastly, I would love to thank my incredible parents and grandparents, without whom I could not stand where I stand today, for all the love, support and continuous encouragement they have always given me.

Resumo

Foi realizada uma campanha experimental no Túnel de Vento Laminar do IAG, relativa a um perfil NACA64418 extrudido, em condições de perda de sustentação a baixa velocidade. Subsequentemente, é feita uma investigação numérica sobre a influência de diferentes modelos de turbulência e condições fronteira para representar as paredes do túnel, utilizando o DLR TAU-Code. A abordagem inicial com o método RANS estacionário, revelou que a condição de fronteira symmetry plan, com o modelo $k-\omega$ SST, tem a melhor concordância com as experiências. Particularmente em termos de padrão de separação a $\alpha = 16°$, ao contrário das combinações symmetry plan/Spalart Allmaras e euler wall/SST. Posteriormente, as simulações URANS utilizando a combinação symmetry plan/SST, revelaram um aumento na concordância com as experiências para os ângulos de ataque mais elevados. A análise espectral e dos perfis de velocidade e tensões de Reynolds da esteira, revelam um movimento pulsante e periódico no regime de perda de sustentação, não observado nas experiências, e também a previsão de uma camada de corte mais estável nas simulações. Porém, é possível uma boa concordância qualitativa. Ademais, a validade da abordagem URANS foi confirmada. Finalmente, as investigações com URANS utilizando a condição euler wall revelaram-se incapazes de capturar flutuações, algo que foi resolvido com o uso de métodos híbridos RANS/LES. As adaptações da malha para a condição viscous wall revelaram um problema de fluxo de junção na interacção entre a camada limite da parede e a da asa, requerindo assim desenvolvimento adicional.

Palavras-chave: CFD; URANS; Turbulência; Separação.

Abstract

A measurement campaign was carried out at the Laminar Wind Tunnel of the IAG, regarding an extruded NACA64418 airfoil in low-speed stall conditions. Consequently, a numerical investigation on the influence of different turbulence models and boundary conditions for representing the tunnel walls is performed using the DLR TAU-Code as the flow solver. An initial RANS approach was undertaken and showed that the symmetry plane boundary condition, together with Menter's $k-\omega$ SST model, yielded the best agreement with the experiments. Particularly, concerning the separation pattern for $\alpha = 16°$, unlike the symmetry plane/SA and euler wall/SST cases. Subsequently, a time resolved URANS simulation with the symmetry plane/SST combination for 3 angles of attack ($\alpha = 8°$, $\alpha = 12°$, $\alpha = 16°$), showed an increased agreement with the experiments for the higher angles of attack. The spectral analysis and investigation of the wake's streamwise velocity and Reynolds stresses profiles revealed a periodic pumping motion of the stall, which could not be seen in the experiments, and the prediction of a more stable shear layer by part of the numerical approach. However, good qualitative agreement with the experiments was possible. Furthermore, the validity of the URANS approach was confirmed. Finally, investigations with the URANS approach for the euler wall condition revealed an inability to capture fluctuations that was solved with the use of hybrid RANS/LES methods. Adaptions of the grid for the viscous wall condition revealed a junction flow problem in the interaction between the wall's boundary layer and the wing, thus requiring further development.

Keywords: CFD; URANS; Turbulence; Flow Separation.

Contents

List of Tables

List of Figures

Nomenclature

Greek symbols

α	angle of attack.
β	$k-\omega$ SST model constant
β^*	$k-\omega$ SST model constant
δ	boundary layer thickness
δ_{ij}	Kronecker delta
Γ	period
γ	gas constant
μ	dynamic viscosity
μ_t	eddy viscosity
ν	kinematic viscosity
ν_t	kinematic eddy viscosity
ω	specific turbulence dissipation rate
ρ	density.
σ	SA model constant
σ_ω	$k-\omega$ SST model constant
σ_k	$k-\omega$ SST model constant
$\sigma_{\omega 2}$	$k-\omega$ SST model constant
τ_{ij}	viscous stress tensor; Reynolds stress tensor
θ	$k-\omega$ SST model constant.

Roman symbols

a_1	$k-\omega$ SST model constant

AR	aspect ratio
b	wing span
L	characteristic length for Strouhal number
C	Courant number
c	chord length
C_1	SA model constant
C_2	SA model constant
C_D	coefficient of drag
C_L	coefficient of lift
C_p	pressure coefficient
$C_{M_{c/4}}$	coefficient of moment at quarter chord
C_{w1}	SA model shield function
Cf_x	streamwise friction coefficient
E	total energy
e	internal specific energy
f	frequency
f_w	SA model control function
$f_{\nu 1}$	SA model damping function
g_1	$k-\omega$ SST model function
h	specific enthalpy
K	experimental correction factor
k	turbulent kinetic energy
M	Mach number
$\vec{n}$	unit normal vector (outward pointing)
P	$k-\omega$ SST model production term
p	pressure
p_0	total reference pressure
p_∞	static reference pressure

p_i static pressure at each pressure tap

q_j heat flux vector

R specific gas constant

Re Reynolds number

Re_x Reynolds number for characteristic length x

S scalar representative of the general strain tensor for the SA model

S_{ij} mean strain rate tensor

Sr Strouhal number

Δt time interval; time step

Δt_c convective time scale

T temperature

t time

Tu turbulence intensity level

U total flow velocity

u, v, w velocity components

u_i i^{th} velocity component

ΔV cell volume

x, y, z cartesian position components

x_i i^{th} position component

$x_{rod,cal}$ rod length of the hot-wire probe obtained in calibration

x_{rod} rod length of the hot-wire probe

$x_{TE,cal}$ distance between trailing edge and hot-wire probe obtained in calibration

x_{trav} x position of the hot-wire probe

Subscripts

∞ reference condition

exp experimental

i, j, k general coordinates indexes

max maximum

min minimum

rms root mean square

$steady$ steady

Superscripts

$-$ Reynolds averaged mean value; mean

’ fluctuating part of Reynolds decomposition; uncorrected variables; experimental coordinate system

” fluctuating part of Favre decomposition

˜ Favre mass averaged mean value

Acronyms

CFD	Computational Fluid Dynamics
CFL	Courant-Friedrichs-Lewy
DLR	German Aerospace Center (Deutsches Zentrum für Luft- und Raumfahrt)
FFT	Fast Fourier Transform
IAG	Institute of Aerodynamics and Gas Dynamics
LES	Large Eddy Simulation
LWT	Laminar Wind Tunnel
PSD	Power Spectral Density
RANS	Reynolds Averaged Navier Stokes
SA	Spalart-Allmaras Model
SC	Stall Cell
SST	Menter's k-ω Shear Stress Transport Model
TAU	DLR TAU Code
URANS	Unsteady Reynolds Averaged Navier Stokes

Chapter 1

Introduction

In our world, aerodynamics plays a major role in the way we live our life. The invention of aircraft changed the way we travel, wind turbines shaped the way we produce energy and rockets revolutionized how we look into the universe. The application of aerodynamics has in the most various industries, without a doubt, revolutionized the way they operate and even created new ones, such as the previously mentioned. With the exponential growth of industry, nowadays, more than ever, the world is faced with the need to find more sustainable solutions for the way it operates. The three sustainability pillars are defined as society, environment and economy. Aerodynamics, together with the technologies associated with it, is able to contribute for these pillars with a wide range of sectors. Some examples are the improved efficiency in environmentally sustainable energies, such as wind energy, and more economically sustainable tools, as is the case of Computational Fluid Dynamics (CFD).

Ever since the beginning of CFD history, this tool has been indispensable in the aeronautics industry for the analysis of complex flows. Eventually other industries, such as the automotive and naval, started using CFD as a way to improve their design methodology as well. However, it is still much a complement to other forms of testing, such as wind tunnel or flight tests. The trend in some industries, such as the automotive, is to decrease the number of physical models used as prototypes and start relying more on numerical methods for development. The growth of both CFD and technology, has allowed for the development of better turbulence modelling, and the possibility to use grids with a higher number of cells and higher order schemes. This increased accuracy has proved that CFD is, without a doubt, a powerful tool that allows for cheaper and more sustainable predictions in the design stage. An example of a powerful CFD tool is the DLR-TAU Code (TAU) used in this thesis. This tool was developed by the Deutsches Zentrum für Luft- Und Raumfahrt (DLR), the german aerospace center. TAU is a flow-solver code based on the compressible Navier-Stokes equations with a wide range of applications that is currently used not only by the DLR, but also by universities and the aeronautical industry as is the example of Airbus.

These factors, among others, have vastly contributed for the great improvement of numerical results seen in the past years. However, the goal is to always improve the current methods and keep moving them as close to reality as possible.

1.1 Motivation

There is no doubt that accurate predictions of flow physics are essential in order to create efficient engineering solutions and for certain purposes, the prediction of flow separation, particularly, is a mandatory requirement to achieve this goal. The use of numerical methods to make these assessments is a key tool, however the flow in this regime is characterized by a complex, non-linear, transient behaviour and a compromise between available computational power and numerical methods is necessary. To fully cover the entire spectra of flow physics, further development of numerical methods is required. As previously mentioned, the use of experimental testing methods has always been the most direct path to make design decisions due to its ability of expanding the view over the phenomena that takes place for the given flow conditions. However, it also presents some limitations due to the role that wind tunnel walls play on the results, such as the effect of blockage (see section 3.3 for more detailed information on this topic). Besides these inherent limitations to wind tunnel testing, this approach is also an excellent way to make an assessment of the behaviour of different numerical methods. Through comparison between numerical results and experimental data, more knowledge can be gathered about the numerical models in question thus allowing to understand their strengths and limitations so that they can be applied in the right conditions and be further developed.

An example of a complex flow behaviour can be found in the results from a measurement campaign on an extruded NACA 64418 airfoil in low-speed stall conditions, conducted in the Laminar Wind Tunnel (LWT) from the Institute of Aerodynamics and Gas Dynamics (IAG) of the University of Stuttgart. Representative and simplified flow cases such as the aforementioned are preferably used in numerical methods verification given that they significantly decrease the computational cost when compared with more complex geometries, such as full aircraft configurations, for example.

The previously mentioned need to pursue the improvement of numerical methods as a way to benefit sustainable development allied with the existence of a test case in the desirable regime, serves as the primary motivation for this work.

1.2 Objective

The main objective of this work is to study the comparability between experimental wind tunnel results and numerical results regarding the complex, non-linear flow observed in low-speed stall conditions on an extruded NACA 64418 airfoil at a Reynolds number of 2.5×10^6. In the experimental campaign, no tripping methods were used. For the appropriate angles of attack, different models of the flow governing equations shall be used as well as different approaches for representing the wind tunnel walls, hereafter discriminated.

Turbulence models:

- k-ω SST
- Spallart-Almaras

Boundary conditions imposed on the walls:

- Symmetry Plane
- Euler Wall
- Viscous Wall

As a starting point, a steady state RANS approach to the problem shall be used. The purpose of this initial steady analysis is due to the fact that steady simulations are less time consuming, thus making it a fit approach for parametric studies. This will allow the evaluation of the polar curves for different turbulence models and boundary conditions. When unsteady nature phenomena is involved, it is not possible to capture it without time resolving methods, so the next step shall be using an URANS approach to the problem for a selection of angles of attack. A more detailed explanation of the turbulence models can be found in chapter 2 and regarding the boundary conditions and angle of attack selection in chapter 4.

The statements regarding the comparability between results shall be made using the following quantitative and qualitative results available from the experimental test:

- Force coefficients
- Pressure distributions
- Flow separation and stall cells
- Wake velocity and Reynolds stresses profiles
- Spectral analysis on streamwise velocity

1.3 Relevance for the Aerospace Sector

The relevance of this work for the Aerospace sector lies, as previously mentioned, in the need of further understanding the strenghts and limitations of the tools that are at its disposition for design. The aerospace sector has largely benefited from the development of numerical methods due to their time and cost saving characteristics, when compared with the other resources available, but deeper insight through comparison with experimental data, for example, allows to push the boundaries further and increase the reliability of these methods as design tools. Ultimalety, the knowledge gained from this work can be translated into more reliable predictions of flow separation and transferred to the analysis of such regime on transport aircraft. This will result in a more accurate prediction of the flight envelope thus benefiting the industry in different points such as increased security, less weight, better aerodynamic efficiency, etc.

1.4 Thesis Outline

This work is divided into 6 different chapters. In the following chapter, a literature review regarding works that are relevant for the subject of this thesis is done followed by an introduction to the CFD tool used for the simulations and, ultimately, a theoretical review of the flow governing equations and turbulence modelling. In Chapter 3, an overview of the measurement campaign performed at the Laminar Wind Tunnel is presented in terms of the different measurement techniques that were applied, the necessary corrections for wind tunnel results, the mounting system and the coordinate system that was used. Later, in chapter 4, the numerical setup for the problem is described in terms of grid generation and its properties as well as boundary conditions and the criteria used in the selection of the angle of attack. In the next chapter (5), the results are presented and the different numerical solutions are compared to their equivalent experimental ones. Some remarks regarding particularities of the boundary conditions and turbulence models used are also pointed out. At last, in chapter 6, the conclusions from the comparison of the solutions are drawn and discussed and, ultimately, suggestions for future work are presented.

Chapter 2

Literature Review and Fundamentals

The purpose of this chapter is to lay down an overview of some work developed in similar flow conditions as to the one covered in this thesis and the relevant observations that were made by the authors. Following this, a description of the flow solver's characteristics is presented as well as some theoretical aspects of flow physics and computational fluid dynamics principles.

2.1 Three Dimensional Flow Patterns in Stall Conditions

The post stall/on stall flow regime has been broadly investigated due to the sudden change of lift and drag as a consequence of flow separation. In an early study regarding such conditions, Winkelman and B.Barlow [1] reported the existence of "owl shaped" structures on the suction side of their rectangular wing model through elementary flow visualization techniques and concluded that that the birth of such structures was not a tip effect but a consequence of a periodic breakdown of the separated region. Nowadays, according to the literature consensus, these structures are know as stall cells (SCs) and are described as a pair of symmetric counter-rotating swirling vortices, being the principal mean flow structures in this regime. Weihs and Katz [2] also laid down one of the first explanations for the appearance of this three dimensional structure attributing it to the result of a two dimensional separation line as a consequence of a Crow-type instability where a chain of vortex rings is formed through the interaction of two-counter rotating vortices that amplify small oscillations in their shape. The mechanism suggested by them is represented in Figure 2.1. Some work in this field worth mentioning as well, is the more theoretical approach by Rodriguez and Theofilis [3] that through the use of global instability analysis and at a low $Re = 200$, explain the appearance of stall cells as a result of spanwise instabilities. Overall, there is consensus that these structures are dynamic and can be unstable in so far as, without any change in the conditions, they can move in the spanwise direction or change in size and number. An effort has been made to investigate the origin, behaviour and effects of SC but a great deal of this investigation has been performed by means of experimental testing and few work so far has been undertaken on this matter using numerical methods.

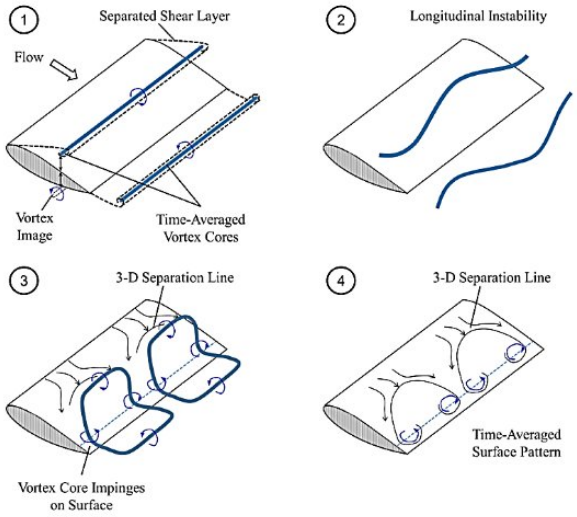

Figure 2.1: Stall cell formation mechanism suggested by Weihs and Katz [2]

Among others, Zarutskaya and Arieli [4] investigated stall cell behaviour using the RANS approach in parallel with experimental investigation. The numeric results showed a highly complex flowfield in the areas of reversed flow and it was found that the turbulence model had a quantitative influence without affecting the basic flow structure. Later, Manolesos et al. [5], also used the RANS approach to investigate on this matter in both two dimensional and three dimensional approaches. On their model, the rectangular wing was modelled with an inviscid wall on the one and a symmetry boundary condition on the other side. Their findings, at a $Re = 10^6$, showed a 3° delay in comparison with experimental data but, as in the work of Zarutskaya and Arieli [4], qualitative analysis was also possible. With this investigation, they managed to draw some new conclusions regarding the behaviour of SC's. It was found that the SC's vortices evolution in the wake is in strong interaction with the separation line vortex and the trailing edge vortex. A closer look at the wing wake showed that this was pushed upstream at the centre of the SC and downwards at the sides by the stall cell's vortices. Also, the pressure distribution, as the distance from the stall cell's vortices increased, became more similar to that of a 2D flow. Regarding force coefficients, due to delay in stall cell formation, an under prediction of the drag coefficient (C_D) was reported and the lift coefficient (C_L) was over predicted, although the trends in their evolution were similar to the experimental ones.

Ragni and Ferreira [6] conducted an experiment of particular interest to this work given the fact that the rectangular wing used was obtained from an extrusion of the same NACA64418 airfoil as used in this work and at a Reynolds number of the same magnitude, $Re = 10^6$, albeit the aspect ratio (AR) of their model was 4 while the one used in this work had a value of 1.22. Their results show the existence of a SC pattern in a range of angles of attack from 9° to 20°. Their examination of single velocity and vorticity components revealed vortical features aligned with the streamwise direction that contributed to the deformation of the shear layer in both spanwise and vertical direction. They suggest that the origin of SC's comes from the instability caused by the breaking of the shear layer and that the shedding is decoupled from the SC's mechanism.

For this work, the available results from the experimental investigation also allowed to identify the presence of stall cells by means of flow visualization techniques. Given the low number of numerical research on the topic, this thesis aims to also provide some new information regarding the influence that different numerical approaches, namely time resolving ones, might have on the representation of such structures.

2.2 Flow Solver

The DLR TAU-Code (TAU) [7–9] was the flow solver used for all the CFD analysis present in this work. This software is a modern unstructured CFD solver based on the compressible Navier-Stokes equations (presented in the next section) and it is able to deal with complex geometries over a wide range of Mach numbers and with either viscid or inviscid flow. A Low Mach preconditioning is also available for incompressible calculations. TAU employs hybrid unstructured grids formed by tetrahedrons, pyramids, prisms and hexahedrons, and although it does not include a grid generation feature, it comprises modules that allow for grid modification.

The parallel partitioning module allows for grids to be partitioned in a defined number of domains for parallel computation and it is one of TAU's most relevant features considering its high efficiency. The use of a multi-grid technique that obtains coarse grids by fusing fine grid volumes is also possible to implement in the pre-processing. This technique allows for a faster convergence and efficiency.

The time integration is based on an explicit Runge-Kutta scheme with a LU-SGS scheme as linear solver, the latter has proved being efficient given its stability with almost no time step restrictions. The LU-SGS is also beneficial due to its low memory requirements, low operation counts and the fact that it can be parallelized with ease. The dual time stepping of Jameson [10] is turned on when dealing with unsteady calculations. This approach executes the time integration by reaching successive steady states in a fictional dual time.

The spatial discretization is performed by using a second-order accurate central scheme for both viscid and inviscid terms. For the latter, there is also the possibility of using different upwind schemes. During the course of this work, a first order upwind scheme for the inviscid terms was selected at the start of every simulation due to its higher stability and faster convergence. After achieving convergence, the scheme was switched to a second order accurate central scheme in order to obtain a more accurate solution.

In regards of transition and turbulence modelling, TAU contains a variety of models for the closure problem of the Reynolds Averaged Navier Stokes. The option to resolve parts of the spectrum instead of completely modelling is also possible through the use of Large Eddy Simulation (LES) and hybrid RANS/LES methods. For eddy viscosity turbulence modelling, some of the available models include one equation models such as the Spalart Allmaras and variations of the same such as the Spalart Allmaras model with Edward's modification, as well as two equation models like Menter's SST and Wilcox's $k-\omega$ model.

2.3 Governing Equations

As mentioned in the previous section, the TAU flow solver is based on the compressible Navier-Stokes equations [11]. This set of equations is derived from the fundamental governing equations of fluid dynamics: the continuity, momentum and energy equations. These equations lay the fundamental principles for fluid flow: mass is conserved, Newton's second law and energy is conserved.

The instantaneous compressible Navier-Stokes equations [12] are the following:

Continuity Equation

$$\frac{\partial \rho}{\partial t} + \frac{\partial}{\partial x_i}(\rho u_i) = 0 \tag{2.1}$$

Momentum Equation

$$\frac{\partial}{\partial t}(\rho u_i) + \frac{\partial}{\partial x_j}(\rho u_j u_i) = -\frac{\partial p}{\partial x_i} + \frac{\partial \tau_{ij}}{\partial x_j} \tag{2.2}$$

Energy Equation

$$\frac{\partial}{\partial t}\left[\rho\left(e + \frac{1}{2}u_i u_i\right)\right] + \frac{\partial}{\partial x_j}\left[\rho u_j\left(h + \frac{1}{2}u_i u_i\right)\right] = \frac{\partial}{\partial x_j}(u_i \tau_{ij}) - \frac{\partial q_j}{\partial x_j} \tag{2.3}$$

Where t is time, ρ is the local density, u_i and x_i are the i^{th} velocity and position components, respectively, p is the local pressure, e the internal specific energy, h the specific enthalpy, τ_{ij} the viscous stress tensor and q_j the heat-flux vector. To complete the underdetermined system of equations, one more equation is necessary. This can be achieved by adding the state equation into the system [13]:

$$p = \rho R T \tag{2.4}$$

Where R is the specific gas constant and T the temperature. The state equation introduces a new variable into the system, but considering the calorically perfect gas approximation, the system can be closed. The following substitution is then applied:

$$p = (\gamma - 1)\rho(E - \frac{|u|^2}{2}) \tag{2.5}$$

Where E is the totally energy defined as:

$$E = e + \frac{|u|^2}{2} \tag{2.6}$$

With the system closed, we are now able to solve it, however, when dealing with a flow that contains an extense range of both length and time scales, while presenting an unsteady and three dimensional behaviour, it becomes extremely costly, both from a computational resources and time point of view, to consider all the instantaneous quantities into our solution. One way to tackle this problem is using the Reynolds or Favre averaging methods by decomposing the field variables into a mean and fluctuating part, which will be discussed in the next section.

2.4 Favre-Reynolds Averaged Navier Stokes Equations

Reynolds [14], in 1895, presented a paper to the Royal Society of London with a new method to approach turbulence modelling that is now known as the Reynolds Averaged Navier Stokes (RANS) method [15]. This new concept for statistical turbulence modelling allows for a decrease in both time and computational cost when compared with actually solving the Navier-Stokes equations. The foundation for RANS begins with the decomposition of the velocity in two different components:

$$u = \bar{u} + u' \tag{2.7}$$

Where $\bar{u}$ denotes the mean value and u' the fluctuating component of velocity.

There are different ways of performing the averaging to obtain the mean, for this case the following are of interest [12]:

Time Averaging

$$\bar{u} = \lim_{\Delta t \to \infty} \frac{1}{\Delta t} \int_{t}^{t+\Delta t} u dt \tag{2.8}$$

This averaging method is appropriate for stationary turbulence. In this type of turbulent flow, the average does not vary with time, turning the flow into space dependent instead of time dependent when Δt, the time interval, is large enough in comparison with the turbulent fluctuation's typical time scale.

Ensemble Averaging

$$\bar{u} = \lim_{N \to \infty} \frac{1}{N} \sum_{n=1}^{N} u_n \tag{2.9}$$

This is the most general type of averaging and it can be idealized as an example in terms of N measurements from identical experiments.

When dealing with a compressible medium, besides velocity and pressure fluctuations, density and temperature fluctuations must also to be taken into account [12]. The mechanism proposed by Osbourne Reynolds, when applied to a compressible flow, introduces additional terms that significantly increase the complexity of the problem. To solve this, the density-weighted averaging procedure introduced by Favre [16] is applied. When using this method, the instantaneous velocity is customarily decomposed in the following way:

$$u = \tilde{u} + u'' \tag{2.10}$$

Where, analogous to the Reynolds decomposition, $\tilde{u}$ is the mass-averaged part of the velocity and u'' the fluctuating part. The mass-average of the velocity, as introduced by Favre, can then be calculated by:

$$\tilde{u_i} = \frac{1}{\bar{\rho}} \lim_{\Delta t \to \infty} \int_{t}^{t+\Delta t} \rho(x,t) u_i(x,t) dt \tag{2.11}$$

This method allows the elimination of density fluctuations from the averaged equations (unlike Reynolds averaging) thus simplifying the problem. However, one has to keep in mind that it does not erase their effect on turbulence.

Applying the decomposition from equation (2.7) to ρ, p and q_j, and the decomposition from equation (2.10) to the other variables, the equations of mean motion for continuity, momentum and energy are obtained:

$$\frac{\partial \bar{\rho}}{\partial t} + \frac{\partial}{\partial x_i}(\bar{\rho}\tilde{u_i}) = 0 \tag{2.12}$$

$$\frac{\partial}{\partial t}(\bar{\rho}\tilde{u_i}) + \frac{\partial}{\partial x_j}(\bar{\rho}\tilde{u_j}\tilde{u_i}) = -\frac{\partial p}{\partial x_i} + \frac{\partial}{\partial x_j}\left[\overline{\tau}_{ji} - \overline{\rho u_j'' u_i''}\right] \tag{2.13}$$

$$\begin{aligned} &\frac{\partial}{\partial t}\left[\bar{\rho}\left(\tilde{e} + \frac{\tilde{u_i}\tilde{u_i}}{2}\right) + \frac{\overline{\rho u_i'' u_i''}}{2}\right] + \frac{\partial}{\partial x_j}\left[\bar{\rho}\tilde{u_j}\left(\tilde{h} + \frac{\tilde{u_i}\tilde{u_i}}{2}\right) + \tilde{u_j}\frac{\overline{\rho u_i'' u_i''}}{2}\right] \\ &= \frac{\partial}{\partial x_j}\left[-\bar{q} - \overline{\rho u_j'' h''} + \overline{\tau_{ji} u_i''} - \overline{\rho u_j'' \tfrac{1}{2} u_i'' u_i''}\right] \frac{\partial}{\partial x_j}\left[\tilde{u_i}\left(\bar{\tau}_{ij} - \overline{\rho u_i'' u_j''}\right)\right] \end{aligned} \tag{2.14}$$

When compared with the original Navier-Stokes equations, new independent unknowns emerge as a result of the averaging method, this is where the crucial problem of turbulence modelling arises. The new terms are referred to as Reynolds-stresses and together they compose the Reynolds stress tensor, τ_{ij}:

$$\tau_{ij} = -\overline{\rho u_i'' u_j''} \tag{2.15}$$

In order to close the problem, additional equations are necessary and they can be implemented through different turbulence models.

2.5 Turbulence Models

For this thesis, two eddy viscosity models were selected for the closure problem: the Spalart-Allmaras (SA), presented by Spalart and Allmaras [17] and the k-ω Shear Stress Transport (SST) developed by Menter [18] . The foundation for eddy viscosity models, such as the aforementioned, is based on the concept of eddy viscosity (μ_t). As proposed by the Boussinesq hypothesis, eddy viscosity serves as a way to introduce a flow-properties-dependent turbulent viscosity to represent turbulent mixing or diffusion, similar to fluid viscosity in laminar flows [15].

$$-\overline{\rho u_i'' u_j''} = 2\mu_t\left(S_{ij} - \frac{1}{3}\frac{\partial \tilde{u_k}}{\partial x_k}\delta_{ij}\right) - \frac{2}{3}\bar{\rho}k\delta_{ij} \tag{2.16}$$

Where S_{ij} is the mean strain-rate tensor and δ_{ij} the Kronecker delta.

Both models incorporate additional transport equations to close the problem. In the case of the SA model, one single equation for the eddy viscosity is introduced, while the wall distance is used to deal with the dissipation, representing a serious limitation for the one equation model. On the other hand, in

a two equation model such as the k-ω SST, a second transport equation is introduced from which the length scale can be derived.

2.5.1 Spallart-Allmaras Model

The SA model is a one-equation turbulence model extensively used in external aerodynamics. The terms included in the one transport equation of this model can be expressed conceptually as follows [15]:

$$\frac{D\nu_t}{Dt} = Generation - Destruction + Diffusion \tag{2.17}$$

The representation of these 3 terms results in the following equation:

$$\frac{D\nu_t}{Dt} = C_1\nu_t S + \frac{1}{\sigma}\frac{\partial}{\partial x_j}\left(\nu_t\frac{\partial\nu_t}{\partial x_j}\right) + \frac{C_2}{\sigma}\left(\frac{\partial\nu_t}{\partial x_j}\right)^2 - C_{w1}f_w\left(\frac{\nu_t}{y}\right)^2 \tag{2.18}$$

Where ν_t is the kinematic eddy viscosity, C_1, C_2, σ are constants whose values need to be calibrated, S a scalar representative of the general strain tensor, f_w a control function and C_{w1} is chosen in a way that the transport equation correctly predicts the log-law layer. The appearance of the wall distance in the last term of equation (2.18) expresses how the SA model is dependent on the prescription of a length scale, which is accomplished through f_w. This function varies between 0 and 1, depending if the region is within the log-law region (f_w=1) or in free shear layers ($f_w = 0$), and it is calibrated to extend the model's range of applicability to the outermost part of a boundary layer and to boundary layers subjected to adverse pressure gradients.

However, the previous formulation is only valid for regions beyond the viscous sublayer. The introduction of a damping function, $f_{\nu 1}$ allows the extension of the model to the wall regions:

$$\nu_t = f_{\nu 1}\tilde{\nu_t} \tag{2.19}$$

Where $\tilde{\nu_t}$ is the kinematic eddy viscosity that would prevail without the viscous sublayer [15]. The derivation of the transport equation, the development of the control function and the calibration of the constants results in the following equation for the SA model:

$$\frac{D\tilde{\nu_t}}{Dt} = C_1\tilde{\nu_t}S + \frac{1}{\sigma}\frac{\partial}{\partial x_j}\left((\tilde{\nu_t}+\nu)\frac{\partial\tilde{\nu_t}}{\partial x_j}\right) + \frac{C_2}{\sigma}\left(\frac{\partial\tilde{\nu_t}}{\partial x_j}\right)^2 - C_{w1}f_w\left(\frac{\tilde{\nu_t}}{y}\right)^2 \tag{2.20}$$

2.5.2 k-ω SST Model

The k-ω SST (SST) model is a two-equation eddy viscosity model and, same as the SA model, it is also extensively used in external aerodynamics applications. The two new transported variables introduced by the model are the turbulent kinetic energy, k, and the specific turbulence dissipation rate, ω. k is used to determine the turbulent energy and ω, the length scale. The SST model can be seen as an hybrid between the two-equation eddy viscosity models, $k-\omega$ and $k-\epsilon$. As explained by Leschziner [15],

the k-ω model shows advantages in the near wall regions without having to resort to damping functions, but it reveals some problems in the low-shear region. On the other hand, the k-ϵ model performs more competently in the low-shear region. Menter took these observations as a motivation to blend both models which resulted in an improved prediction of flow separation under adverse pressure gradients.

The blending of both models is, formally, effected with the use of a weighted average that operates on the corresponding models coefficients:

$$C_{eff} = FC_{k-\omega} + (1-F)C_{k-\epsilon} \tag{2.21}$$

where F denotes a blending function ensuring that the k-ω model dominates in the region near the wall and that the k-ϵ dominates in the free stream [15].

The two-equation model is given by the following [18]:

$$\frac{\partial(\rho k)}{\partial t} + \frac{\partial(\rho u_j k)}{\partial x_j} = P + \frac{\partial}{\partial x_j}\left[(\mu + \mu_t\sigma_k)\frac{\partial k}{\partial x_j}\right] - \beta^*\rho k\omega \tag{2.22}$$

$$\frac{\partial(\rho\omega)}{\partial t} + \frac{\partial(\rho u_j \omega)}{\partial x_j} = \frac{\theta}{\nu_t}P + \frac{\partial}{\partial x_j}\left[(\mu + \mu_t\sigma_\omega)\frac{\partial \omega}{\partial x_j}\right] + 2(1-F)\frac{\rho\sigma_{\omega 2}}{\omega}\frac{\partial k}{\partial x_j}\frac{\partial \omega}{\partial x_j} - \beta\rho\omega^2 \tag{2.23}$$

P is a production term and σ_k, σ_ω, $\sigma_{\omega 2}$, γ, β^* and β are constants that can take up to two different values, depending on which model (k-ω or k-ϵ) is dominating in a specific region. Therefore one set of values for the constants should be used in the near wall region and another in free shear layers.

For the SST model [18], Menter also introduced a 'shear-stress limiter' thus redefining the eddy viscosity as:

$$\mu_t = \frac{\rho a_1 k}{max(a_1\omega, \frac{\partial U}{\partial y}g_1)} \tag{2.24}$$

Where a_1 is a constant and g a function limited between 1 for the boundary layer and 0 for free shear flow. This new definition ensures that, in an adverse pressure gradient boundary layer, the production of k is larger than its dissipation thus satisfying Bradshaw's assumption that the shear stress in the boundary layer is proportional to the turbulent kinetic energy while the original formulation, $\mu_t = \rho\frac{k}{\omega}$, is used for the rest of the flow.

Chapter 3

Experimental Measurements

3.1 Wind Tunnel and Measurement Techniques Overview

The measurement campaign was conducted at the LWT from the Institute of Aerodynamics and Gasdynamics of the University of Stuttgart. The LWT, as described by Würz et al. [19], is an open return wind tunnel with a closed test section area of 0.73x2.73 m^2 and length of 3.15m. The test section is surrounded by a low-pressure chamber which prevents air from passing into the test section through leaks. One of the LWT's characteristics worth of highlighting is its very low turbulence intensity level (Tu). It features a Tu of less than 2·10^{-4} at 60 m/s in the range of 10-5000 Hz, due to its 100:1 contraction ratio and five screens to minimize turbulence fluctuations.

For this campaign, several experiments were performed at different angles of attack and at two Reynolds numbers of 1.25×10^6 and 2.5×10^6, with the latter being the focus of this work . In order to evaluate the flow's properties, the following techniques were used:

- Measurement of lift and drag polars
- Surface static pressure distributions
- Oil flow surface visualizations
- Hot-wire wake measurements
- Visualizations of the recirculation area by means of a high frequency camera and smoke injection

For this thesis, the data collected from the experimental polars, pressure distributions, oil flow visualization and hot-wire wake measurements was used to establish a comparison with the numerical results. More detailed information regarding how these techniques were performed can be found further in this chapter.

3.2 Model and Mounting System

The model used in the experiments was obtained from the extrusion of a NACA 64418 airfoil. The chord length (c) measures 0.6 meters and its span (b) covers the full distance of 0.73 meters between the wind tunnel walls. The model was mounted vertically on the tunnel disc between the wind tunnel walls, as seen in Figure 3.1, and the gaps between the wing and the tunnel walls were sealed with adhesive tape. The centre of the tunnel disc denotes the origin of the fixed tunnel coordinate system. The x-axis is in downstream direction, whereas the y-axis points to the suction side of the airfoil.

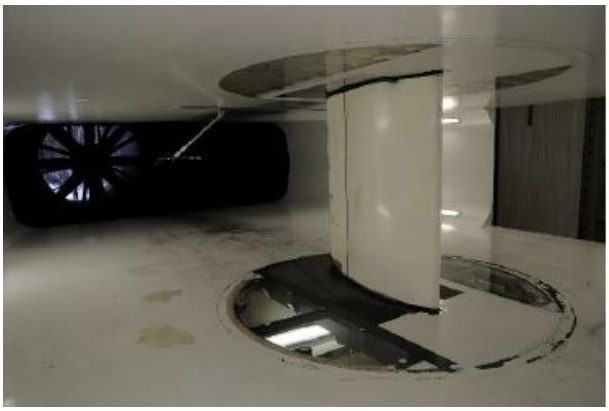

Figure 3.1: Wing Setup in the Laminar Wind Tunnel.

3.3 Wind Tunnel Corrections

Several effects related with the wind tunnel walls have an influence on the flow's properties. Thus, their contribution to the measured values has to be taken into account. D.Althaus [20], in his report, presents a description of the effects caused by solid blockage, streamline curvature, wake blockage as well as buoyancy, and how to account for them in the particular case of the LWT. For the data collected from the measurements, the following standard corrections are applied:

$$C_L = K_{C_L} C'_L \tag{3.1}$$

$$C_D = K_{C_D} C'_D \tag{3.2}$$

$$C_{M_{c/4}} = K_{C_M} C'_{M_{c/4}} \tag{3.3}$$

$$\alpha = K_\alpha \alpha' \tag{3.4}$$

The primed variables represent the uncorrected ones that are then multiplied by their respective correction factor K. More information on how these factors are calculated can be found in appendix A.

3.4 Lift and Drag Measurements

The measurement of the lift force in the LWT is performed through an experimental integration of the pressure distribution along the two opposite vertical wind tunnel walls [19]. This system, when compared with balance measurements, allows to avoid any gap between the wind tunnel walls and the model. For the measurement of drag, the wake rake is integrated. The rake is positioned behind the trailing edge and automatically travels into the middle of the wake while aligning itself with the local flow direction and its width is selected according to the expected drag.

3.5 Pressure Measurements

The surface pressure distribution was obtained by using static surface pressure taps. More information regarding the location of the taps can be found in [19] and an illustration is shown in figure 3.2.

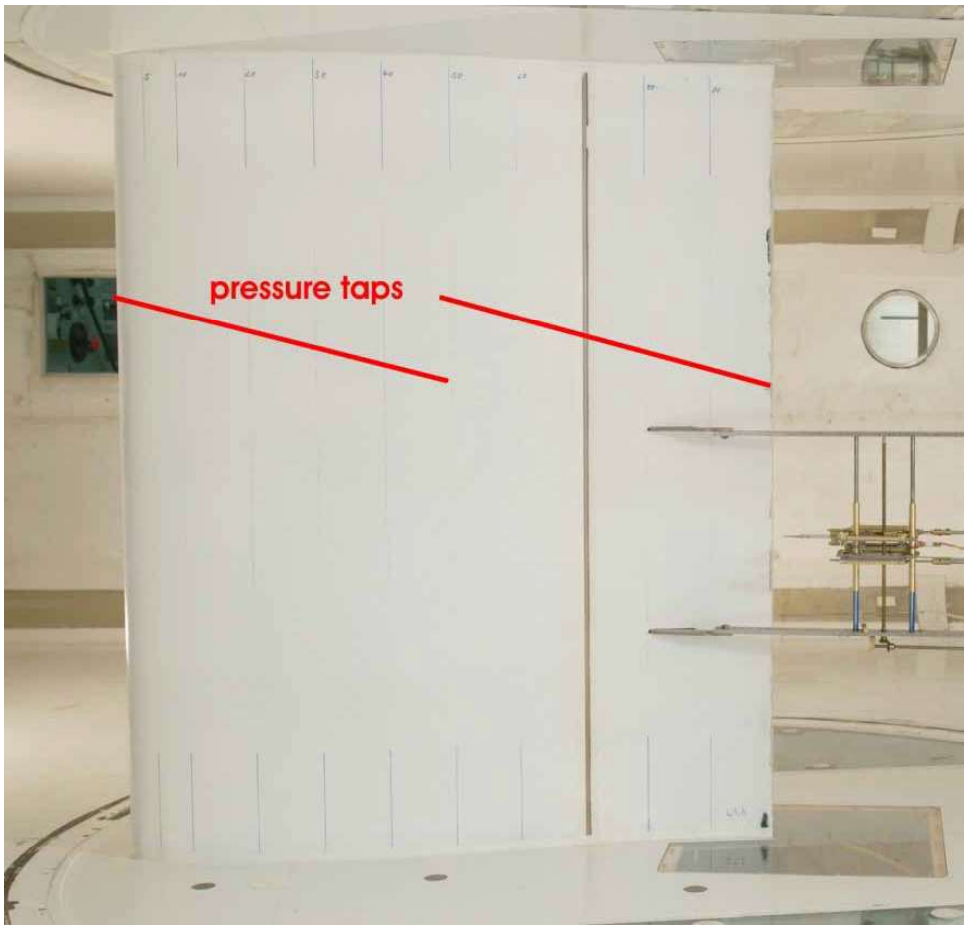

Figure 3.2: Pressure taps position - pressure side perspective.

The reason behind such disposition is so that it should prevent any upstream tap from disturbing the downstream one.

500 samples were averaged for each measurement and the definition used for the computation of the pressure coefficient, C_p, was the following:

$$C_p = 1 - \frac{p_0 - p_i}{p_0 - p_\infty} \tag{3.5}$$

Where p_0 is the total reference pressure in settling chamber of the wind tunnel, p_i the static pressure at each tap and p_∞ the static reference pressure in the test section. The C_p distribution was not corrected due to that being a very costly and complex operation [19].

3.6 Oil Flow Visualization

The oil flow visualization technique allows us to visualize the separation pattern on the suction side of the wing. The paint is composed of a black pigment and kerosene mixture. Firstly, the oil is sprayed on the model followed by the setting of the desired angle of attack. This procedure was performed for every angle of attack that underwent this technique. For angles of attack within the separation region, distinct cellular patterns were reported as well as a non uniform separation line. Given the vertical mounting of the model, one must take into account that gravity might influence the surface's oil distribution pattern. Figures 3.3 to 3.6, show the pictures taken during this experiment for 4 angles of attack. For all the following figures, the freestream flow is flowing upwards and the gravity vector points from right to left.

Figure 3.3: Oil flow for $\alpha = 10°$

Figure 3.4: Oil flow for $\alpha = 12^\circ$

Figure 3.5: Oil flow for $\alpha = 15^\circ$

Figure 3.6: Oil flow for $\alpha = 16^\circ$

3.7 Hot-Wire Measurements and Traversing System

The hot-wire measurements consist of 15 series, including repeats. All runs, except for one at $\alpha = 12°$, were performed at $\alpha = 15°$ and for each position about 440000 temporal samples were captured during approximately 10 seconds. The hot-wire probe uses the standard y-z traversing system of the tunnel and manual positioning in the x-direction. The traversing system used is fixed and does not rotate with the model when the angle of attack is altered, therefore, throughout the experiment, the probe axis was aligned with the tunnel centre line. For each traversing profile the distance to the model's trailing edge was adjusted by moving the rod as illustrated by the sketch in Figure 3.7.

The probe's x position, x_{trav}, relative to the tunnel coordinate system is given by

$$x_{trav} = x_{TE,cal} + x_{rod} - x_{rod,cal} + 0.75c + x_{c/4} \tag{3.6}$$

Where $x_{c/4}$ represents the model's quarter chord position, x_{rod} the rod length, $x_{TE,cal}$ is the distance of the probe relative to the trailing edge, obtained during a calibration at $\alpha = 0°$ and $x_{rod,cal}$ the corresponding rod length.

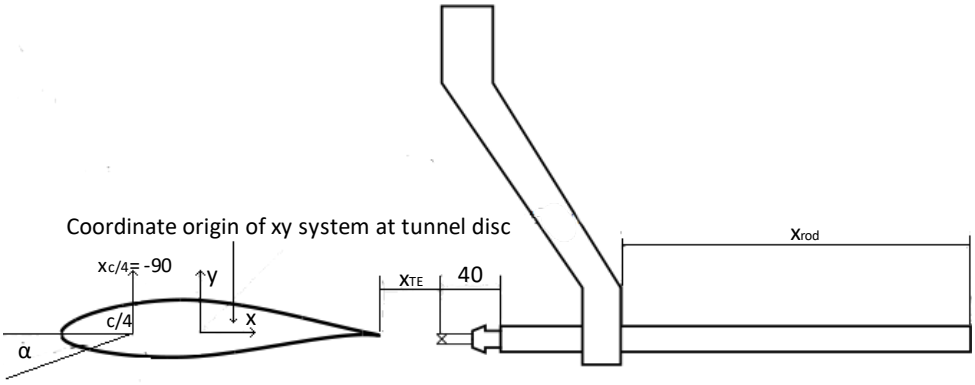

Figure 3.7: Sketch of the mounting configuration for the hot-wire traverses.

For the numerical simulations, unlike the experimental measurements, a coordinate system centred at the wing's leading edge and that does not rotate with an increase in the angle of attack was used. The vertical component of both coordinate systems differs in its nomenclature, with z being used for the numerical thus, for simplicity's sake, whenever comparing the vertical component between the numerical and experimental system, y shall be used as the generalized nomenclature for the vertical position. In order to be able to compare numerical and experimental results from the same position, it was necessary to transform the coordinates system from the numerical solution into the experimental one. This was achieved by rotating the numerical coordinate system by α degrees along the spanwise axis, followed by a translation in the y and x axes. The translation is given by the following formulas:

$$x' = x - 0.24 \cdot cos\alpha \tag{3.7}$$

$$y' = y + 0.24 \cdot sin\alpha \tag{3.8}$$

Where x' and y' are the transformed positions to the experimental coordinate system, x and y the positions in the numerical coordinate system and 0.24 the distance between the leading edge and the origin of the xy system at the tunnel disc. An illustration of the original numerical coordinate system and the transformed one can be found in Figure 3.8 below.

(a) Original system (numerical)

(b) Transformed system (experimental)

Figure 3.8: Illustration of coordinate system transformation.

Chapter 4

Numerical Setup

The aim of this chapter is to provide a description of the numerical setup used to model the experimental campaign test conditions. Firstly, a characterization of the grid and boundary conditions that were used is given, as well as the fundamental ideas to transform the grid in order to suit the needs of particular boundary condition types. This is followed by an explanation of the angle of attack selection criteria and, ultimately, an overview of the simulation parameters and different numerical techniques applied in the calculations.

4.1 Grid Generation

Prior to this work, a hybrid grid of the NACA 64418 testcase with the wingspan and chord length of the measurements in the LWT was created to meet the criteria for hybrid RANS/LES simulations by following guidelines as the ones presented in the report of Spalart [21]. The work developed using this grid was deemed satisfactory and therefore this hybrid grid was extended for the investigation of wall effects using steady and unsteady RANS calculations present in this thesis.

The grid was generated by spanwise extrusion of a 2-D circular shaped grid centered at the airfoils's leading edge and was composed by approximately 20 million cells. The circle has a radius of 50 times the chord length in order to guarantee that the inflow/outflow regions are sufficiently far away from the wing so that there is no influence from the wing at the boundaries. The width of the grid is equal to the wing's span ($0.73m$) so that the wing extends from one boundary to the other as in the experimental test. The hybrid grid comprises a more refined, structured area covering the near wing and wake region and a coarser, prisms one, covering the remaining of the domain as shown in Figure 4.1. The structured block consists of approximately 14.7 million hexahedral elements with a characteristic cell size of $0.01m$ whereas the unstructured block is formed by approximately 5.3 million prism cells.

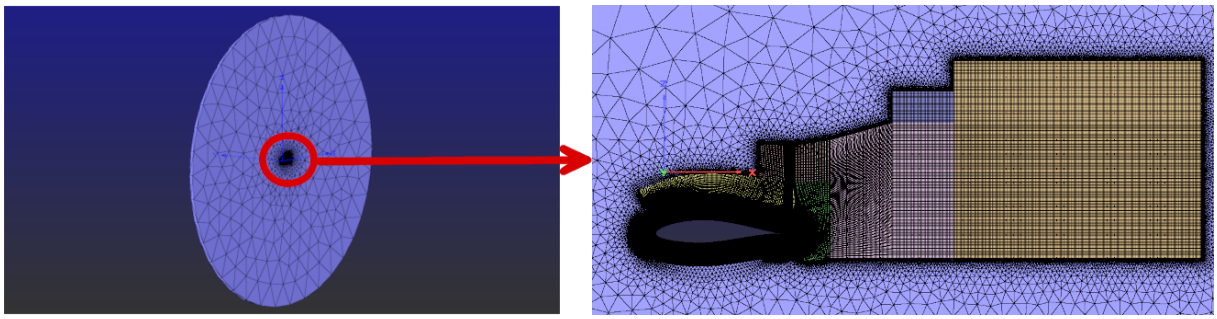

Figure 4.1: Grid.

The wing's surface is divided into three areas: suction side, pressure side and trailing edge. This set is formed by 49536 cells equally spaced through 129 points in the spanwise direction and with a cell size of approximately $\Delta y/c = 0.0095$. The chordwise geometry was divided into 195 points. The leading edge and trailing edge areas, due to their geometric complexity, have a higher concentration of cells when compared with the remaining of the wing surface, as shown in Figure 4.2 thus following the recommendations of the AIAA Drag Prediction Workshop [22] for chordwise spacing. It is worth noting that due to the increased computational cost associated with switching to three dimensional simulations, the chordwise and spanwise spacing is increased when compared with the recommendations for a two dimensional case.

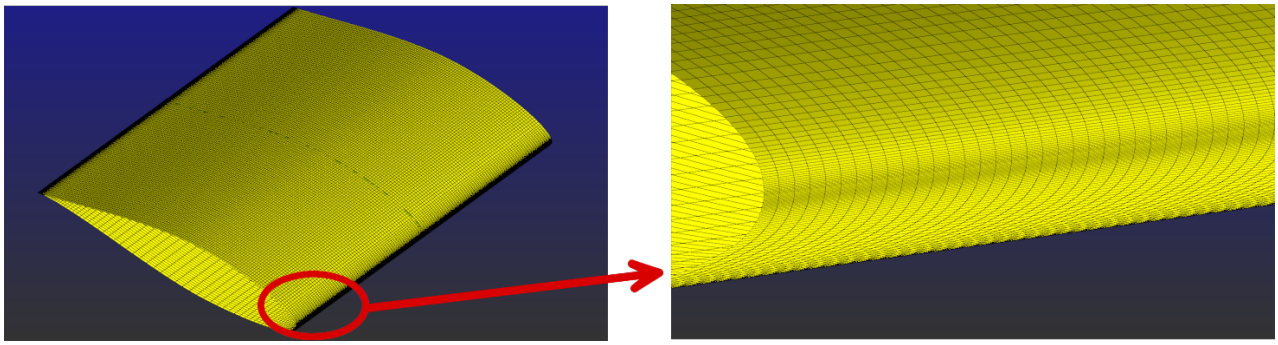

Figure 4.2: Wing surface grid.

When setting a no-slip condition on the airfoil surfaces, a higher resolution for the near wall cells is required in order to accurately capture the boundary layer physics and ensure a proper y^+ value on the viscous surfaces. For this purpose, a hexahedron layer consisting of 65 layers was extruded in the normal direction of the wing's surface (Figure 4.3).

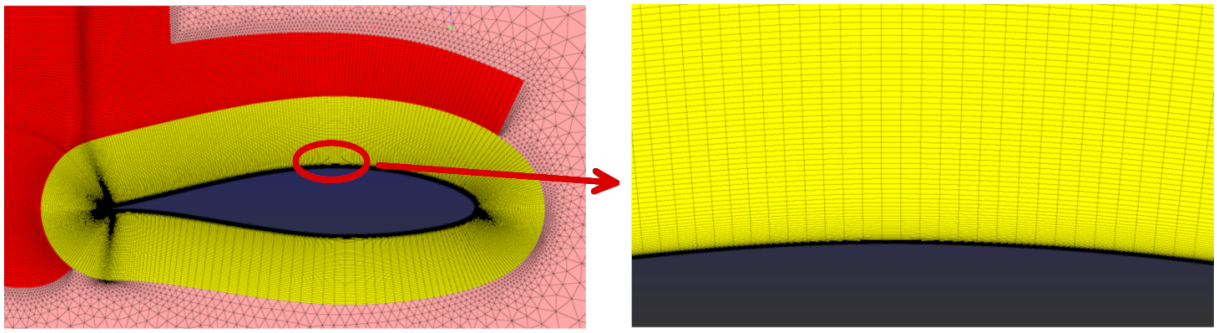

Figure 4.3: Hexahedron layers on wing surface.

4.2 Boundary Conditions

TAU offers a wide range of treatments that can be assigned to the model's boundaries, and selecting the appropriate one is an important matter considering that they introduce new constraints into the simulations. For this model, the flow was treated as compressible and the following regions need to be assigned a boundary condition type: the inflow/outflow region, the walls and the wing.

The inflow/outflow boundary was assigned the **farfield** option. This boundary condition defines an inflow/outflow boundary far away from the investigated configuration for external flow. With this boundary treatment, the presence of the configuration should hardly influence the state of the flow variables at the boundary as in an infinite domain (see [13]). For the inflow region, four variables have to be specified: the three velocity components and the temperature.

$$u = u_\infty, \qquad T = T_\infty \tag{4.1}$$

The density, ρ, is extrapolated from the first inner grid point of the domain.

For the outflow region, the following condition is prescribed:

$$\rho = \rho_\infty \tag{4.2}$$

With the velocity and temperature values being extrapolated from the first inner grid point of the domain. Following this prescription of the flow conditions, the fluxes crossing the boundaries are computed by solving a Riemann problem [23].

Figure 4.4 depicts the area covered by this boundary condition in blue.

As the wing is intended to be modelled as a wall with viscous effects, the boundary type was set to **viscous wall**. This boundary condition defines a solid, adiabatic wall that accounts for both viscid and inviscid effects. As noted in [24], the following overall constraints are defined at the wall when this boundary condition is set:

$$\vec{u} = 0, \qquad (\vec{\nabla} T) \cdot \vec{n} = 0, \qquad (\vec{\nabla} \rho) \cdot \vec{n} = 0 \tag{4.3}$$

Where $\vec{u}$, T and ρ are the velocity, temperature and density at the boundary, respectively, and $\vec{n}$ the normal vector to the boundary.

Investigating the type of boundary treatment's influence on the flow field is one of the main goals for this work and therefore, as mentioned in section 1.2, for the modelling of the left and right wind tunnel walls, the **symmetry plane**, **euler wall** and **viscous wall** options were selected.

The **symmetry plane** boundary condition defines a plane respective to which the flow is symmetrical. This symmetry is handled by setting all fluxes in the wall-normal direction to zero. Notably, the following conditions are applied:

$$\vec{u} \cdot \vec{n} = 0, \qquad (\vec{\nabla} T) \cdot \vec{n} = 0, \qquad (\vec{\nabla} \rho) \cdot \vec{n} = 0 \tag{4.4}$$

When using the **euler wall** condition, a solid adiabatic wall is defined, identical to the viscous wall condition, however all viscous effects are neglected.

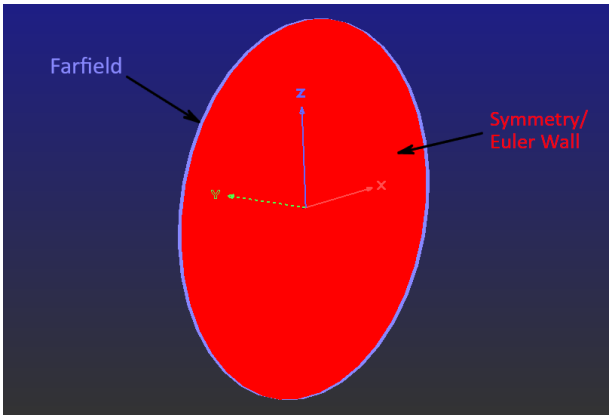

Figure 4.4: Boundary Conditions

With the implementation of the **viscous wall** boundary condition to the tunnel walls a new problem arises, unlike when using the **symmetry plane** or **euler wall** conditions where no viscous effects are considered. This boundary type implies the development of a boundary layer starting at the inlet of our model, like it happens in real conditions. Therefore, the distance between the flow-inlet boundary and the wing needs to be accounted for, as well as the cells resolution in the near-wall region. For this purpose, different grid adaptations of the one just presented were made, in order to fulfil the requirements for viscous walls. Further detail about the overall fundaments for the viscous wall treatment can be found in the next section and the different approaches to solve the problem shall be discussed in the next chapter.

4.3 Grid Adjustments for Viscous Walls

In order to make the grid suitable for modelling the wind tunnel walls as viscous walls, increased resolution on the walls was necessary by means of a hexahedral layer extrusion that could capture the

boundary layer physics. Several iterations of the grid were made, and the composition of the final one shall be described next.

In order to capture the boundary layer phenomenon that occurs in the wind tunnel walls as accurately as possible, the distance between the flow-inlet and the wing model was calculated based on the wall's boundary layer thickness, δ, when reaching the model. The value of δ was not measured, but it is estimated to be approximately 30 mm according to reports from the LWT.

For calculating the distance x from the wing to the flow-inlet, the Reynolds number for x (Re_x) was used together with the equation for the thickness of turbulent boundary layers along a flat plate:

$$Re_x = \frac{\rho u x}{\mu} \tag{4.5}$$

$$\delta = \frac{0.37x}{Re_x^{1/5}} \tag{4.6}$$

Where in equation (4.5) u, ρ and μ are the inlet flow values for velocity, density and dynamic viscosity, respectively. Substituting the known values into both equations yielded a value of $x = 1.975m$.

As mentioned in the previous section, to resolve the boundary layer, an increase of the near wall cell's resolution is mandatory. This was achieved by means of a prisms and hexaheadrals layer extrusion on each wall. The calculation was performed with the aid of a python script for boundary layer mesh calculation and the inputs are listed in the table below.

Table 4.1: Inputs for prism and hexahedral layer calculation.

Desired y^+	1
Number of Prism Layers	45
Reynolds Number	2.5×10^6
Characteristic Length	$0.6m$

The selection of the chord length for the characteristic length instead of the $1.975m$ is to assure that the prism layer outputs are set correctly for resolving the wall boundary layer in the near wing region.

The structured region of the previous grid was kept and rotated accordingly to the desired angle of attack due to the new imposed boundary conditions that will be addressed. The circular domain was transformed into a rectangular one with a more uniform cell size, as shown in Figure 4.5, with a height of 40 times the chord lenght in both directions and and extension of 24 times the chord length downstream of the trailing edge. The final grid was composed by approximately 31 million cells.

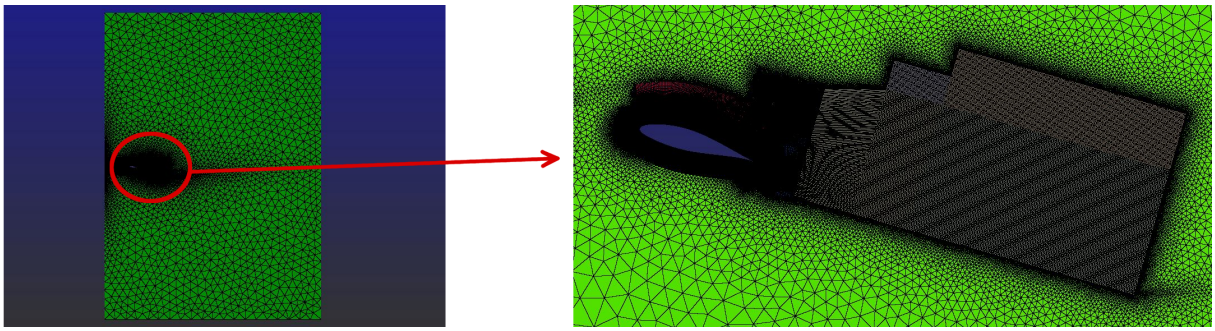

Figure 4.5: Grid for viscous walls condition.

The tunnel inlet wall was assigned the **engine exhaust** boundary condition which fixates the Mach number at the inlet whereas the outlet wall was assigned the **engine inflow** which is used to control the outlet's pressure in order to match the wind tunnel's reference pressure at the exit. The top and bottom walls were defined as non viscous walls (**euler wall** boundary condition) only for this particular grid.

4.4 Angle of Attack Selection

The angle of attack selection was based on the available data from the experiments, mainly the results provided by the polar measurements and the angles selected for the hot-wire runs (12° and 15°). From the experimental lift polar curve in Figure 4.6, the decrease in slope for $\alpha > 8°$ evidences the beginning of flow separation. For the steady RANS simulations, 9 different angles of attack were selected: $0°$, $5°$, $8°$, $10°$, $12°$, $14°$, $15°$, $16°$ and $17°$. The increment decrease between successive angles of attack is justified by the increased complexity of the flow physics caused by flow separation as the angle of attack increases.

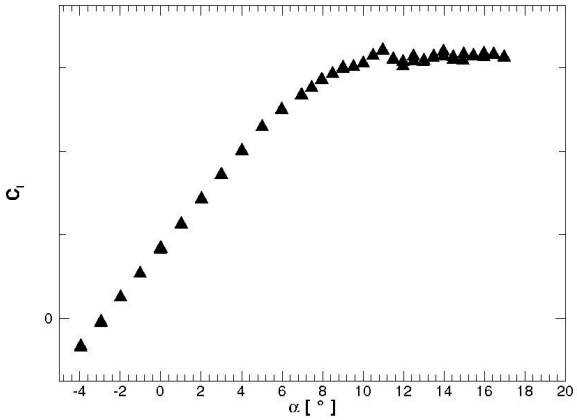

Figure 4.6: Experimental lift coefficient polar curve

For the unsteady RANS simulations, one has to take into account the increased computational cost when compared with the steady version thus the angle of attack selection was narrowed to 3 angles:

$8°$, $12°$ and $16°$. Through this selection we can identify three different regimes of flow physics as the $\alpha = 8°$ case is located at the onset of flow separation, $\alpha = 12°$ is at an initial stage of the separation and $\alpha = 16°$ at a more advanced phase of flow separation. Previous numerical investigation conducted at the IAG showed, using hybrid RANS/LES methods, that there was a delay of $1°$ from the numerical results to the experimental ones. This correlation, which shall also be investigated in this work, is the reason behind the selected angle of attack $(16°)$ in the more advanced phase of flow separation when the data available from wake measurements is for $\alpha = 15°$.

4.5 Flow Solver and Simulation Parameters

4.5.1 Pre-Processing

As stated in chapter 2, TAU offers in its pre-processing module, the parallel partitioning option which divides the grid into a given number of domains as well as the chance to use a multi-grid technique in order to accelerate convergence. For this work, according to the computational power available, the grid was either divided into 432 or 216 domains. For each grid, 4 grid multi-levels were used and a w-cycle was selected for the calculations.

4.5.2 Overall Parameters

As a way to accelerate convergence, the discretization of the inviscid fluxes, at the start of every simulation, was set to a first order upwind scheme. The first order upwind discretization allows for a more stable and faster convergence when beginning the calculations. Once the calculation converged and the acceptable maximum residual value was reached, the inviscid fluxes discretization type was changed to a second order central discretization scheme. The switch from the first order upwind to the second order central scheme allows the calculation to reach a more accurate solution by means of decreasing the numerical and artificial dissipation. The 4^{th} order dissipation coefficient was set to 128 which generates slightly lower dissipation than the standard 2^{nd} order central discretization scheme.

The flow reference properties were set to the same values as the ones that were found during the experimental testing and are listed in table 4.2 below.

Table 4.2: Flow reference properties

Reynolds Reference Length	$0.6m$
Reference Temperature	$288K$
Reference Density	$1.18471kg/m^3$
Mach Number	0.185
Reynolds Number	2.5×10^6
Gas Constant (γ)	1.4

The turbulence intensity was also set for the same value that is encountered in the LWT, 0.1%.

4.5.3 Convergence Criteria

TAU, similar to other CFD codes, yields residual values that can be used to monitor the evolution and convergence of the simulation. The monitoring can be made through the global density residual and/or through the force coefficients residual (C_L and C_D). The C_L and C_D residual represent the change in the force coefficient between the current and former iteration. For this case, given the flow conditions, more attention was given to the force coefficients residual since they are computed from the surface pressure. Usually, a decrease up to 4 or 5 orders of magnitude without any oscillations is a good indicator of convergence.

4.5.4 Unsteady Parameters

As mentioned in chapter 2, TAU uses a dual time stepping method for time accurate computations. The selection of the physical time step size for the unsteady calculations is based on the convective time scale of the flow. The reference length for the calculation of this scale is based on the chord length of the wing, $c = 0.6m$ and on the reference Mach number of $M_\infty = 0.185$. For the reference conditions, this Mach number translates into a flow velocity, (U_∞), of 62.94 m/s. Therefore, the convective time scale of the flow can be calculated as follows:

$$\Delta t_c = \frac{c}{U_\infty} \tag{4.7}$$

This results in a convective time scale of approximately $9.5 \times 10^{-3} s$. In combination with the spatial discretization, 100 time steps per convective time scale, resulted in a physical time step size of $9.5 \times 10^{-5} s$. In order to save computational power, all the URANS simulations were started from the final iteration of their RANS counterpart.

At the beginning of this chapter, it was noted that the original grid was developed to fulfil hybrid RANS/LES turbulence modelling criteria. A rough assessment of the physical time step size's suitability for this grid can be made through the Courant–Friedrichs–Lewy (CFL) condition. This condition requires that the full numerical domain of dependence must contain the physical domain of dependence ([25]). The CFL condition can be verified accordingly to the value of the Courant number (C) which correlates the grid spacing and the time scale.

The Courant number, for isotropic cells as is approximately the case within the structured region, can be defined as follows:

$$C = \frac{U \Delta t}{\sqrt[3]{\Delta V}} \tag{4.8}$$

Where U is the total velocity, Δt the physical time step size and ΔV the cell volume.

The results obtained from the URANS simulations shall then later be used to make a recommendation for the time step size of future hybrid RANS/LES approach to the same case in order for a target Courant number close or less than 1 to be obtained in the regions of interest i.e. separated flow and wake regions.

4.6 y^+ Evaluation

An assessment of the grid's suitability for RANS methods can be performed by inspection of the wings surface y^+ values. For viscous turbulent flows, a y^+ value equal or inferior to 1 is required on viscous surfaces in order to guarantee the suitability between the grid and the model. In figures 4.7 and 4.8 the surface y^+ values were plotted on the wing's suction side for the symmetry plane boundary condition at $\alpha = 16°$, using both the SST and SA model. The freestream flow is flowing along the x axis.

For the SST case, in figure 4.7, the leading edge region shows values above the limit. These high values can be dismissed given that the required y^+ value is only targeted for the turbulent flow regions. A smaller region with a higher y^+ value can also be identified near the center of the wing however, overall the y^+ values can be considered suitable for using RANS methods. The SA case in figure 4.8, as in the SST, presents higher values for y^+ in the leading edge area but the rest of the wing falls within the desired limit making it also suitable for RANS methods.

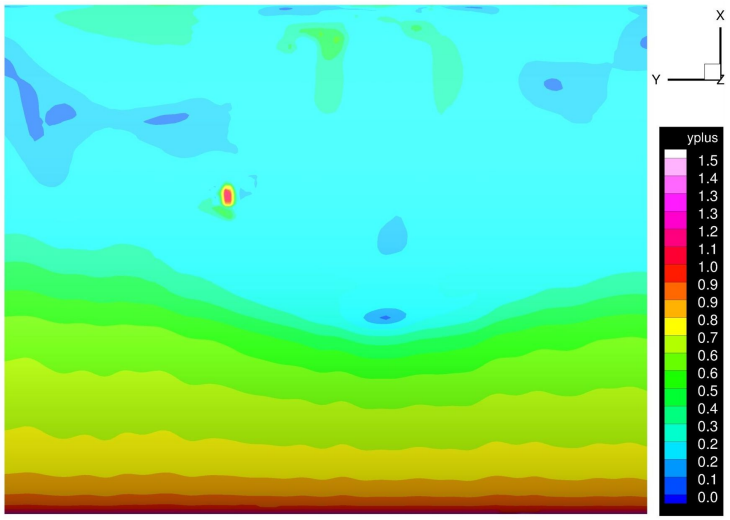

(a)

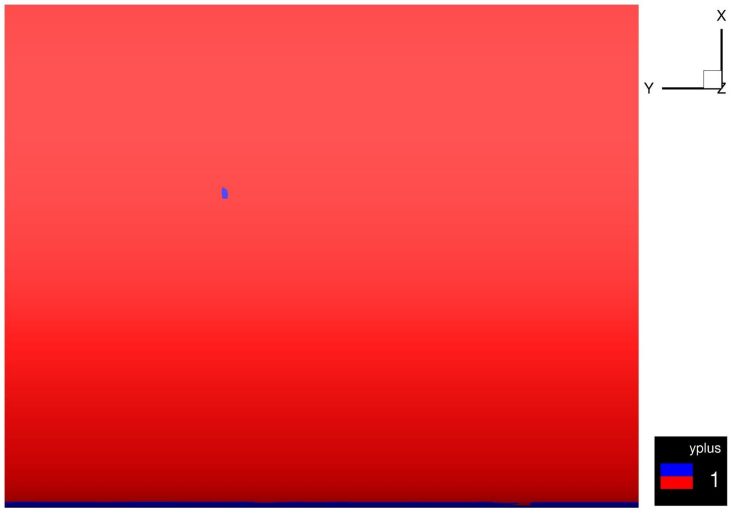

(b)

Figure 4.7: Suction side y^+ distribution for symmetry plane/SST case with $\alpha = 16°$.

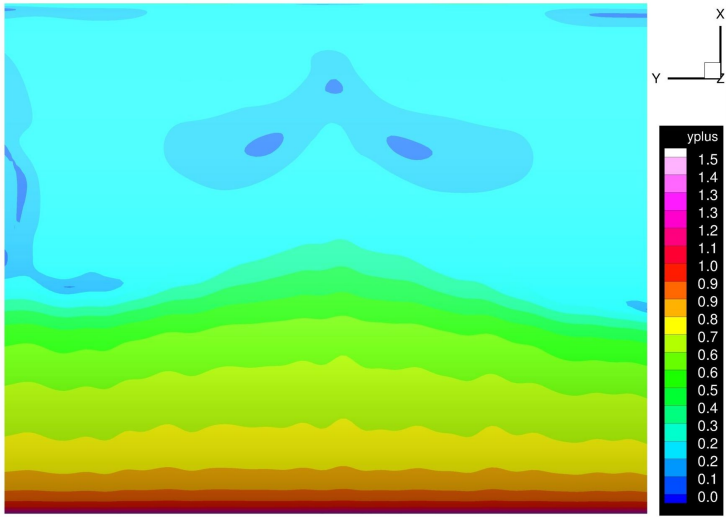

(a)

(b)

Figure 4.8: Suction side y^+ distribution for symmetry plane/SA case with $\alpha = 16°$

Chapter 5

Results

This chapter's goal is to present the results obtained from the different numerical approaches and assess their comparability with the experimental data. Such comparisons are given in terms of force coefficient values, pressure distributions, separation patterns, wake velocity and Reynolds stresses profiles and, finally, by means of a spectral analysis. Further in the chapter, a remark on initial results for more complex modelling approaches is given.

5.1 Steady RANS

5.1.1 Force Coefficients

For the steady approach, the C_L and C_D polars were computed using the SST and SA model for symmetry walls and the SST model for euler walls. The evolution of the numerical solution and its convergence lies strongly upon the selected model and the flow conditions. The latter, in this case, is determined by the angle of attack. Thus, flow conditions associated with lower angles of attack, are expected to return lower residual values due to the weaker unsteadiness in the flow when compared with a higher α regime. This was indeed verified, for lower angles of attack (up to $\alpha = 8°$) both models showed a higher decrease in the force residual values, reaching decreases up to 8 orders of magnitude for the SST and 9 orders of magnitude for the SA. In the higher angle of attack region, when the flow is characterized by strong separation, the SST model verified a residual decrease up to 6 orders of magnitude and the SA up to 8.

Figure 5.1 depicts the aforementioned polar curves and the experimental one.

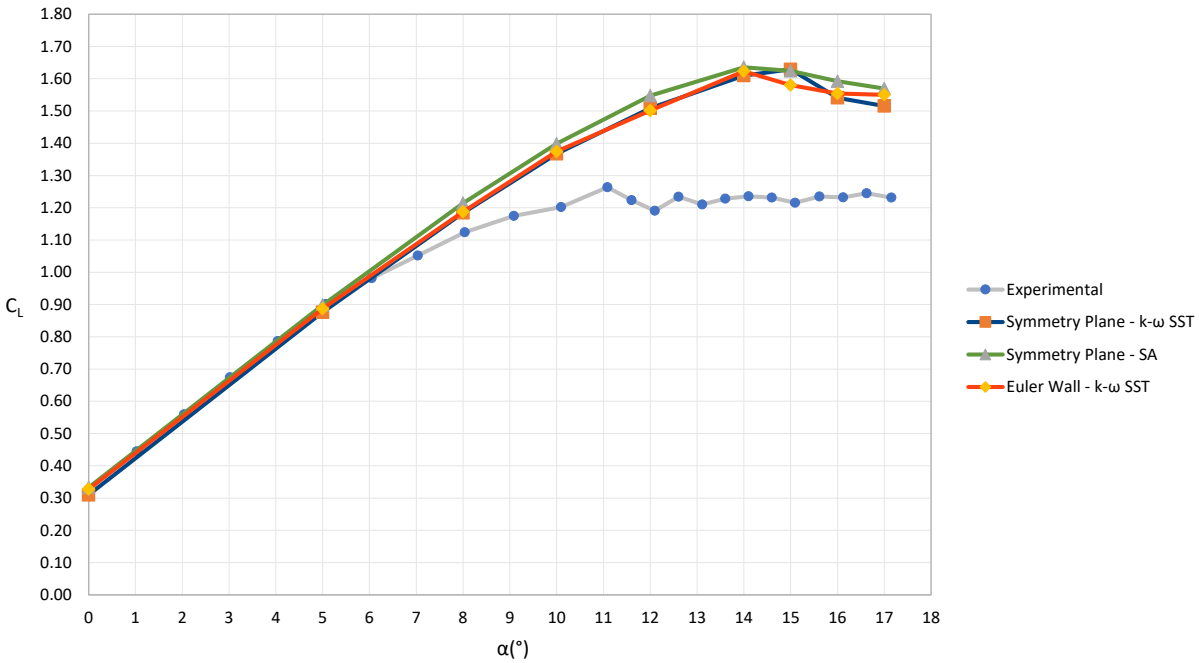

Figure 5.1: Steady RANS Lift coefficient polar curve.

The pressure based conditions in which the simulations are being performed, together with the large unsteady motion that characterizes flow separation is a problem for this approach and it is also necessary to understand the amount of length and time scales that RANS ignores. Also, the assumption of fully turbulent conditions surely influences the flow behaviour given that the models are not prepared for accurately predicting transition to turbulent flow and they most likely place it earlier than in the test results. Consequently, they cannot as well predict the formation of the laminar separation bubble that occurs in the combination of this airfoil with these flow conditions.

When inspecting the plot, it is clear that all cases failed in correctly predicting the experimental values of the lift coefficient in the stall regime. Flow separation occurred later and higher values of C_L were predicted in all cases. The stall regime was achieved with a $4°$ delay when using the SST model with symmetry plane and it improved slightly ($3°$ delay) for the other two cases. For lower angles of attack ($\alpha = 0°$, $\alpha = 5°$ and $\alpha = 8°$), a very good agreement with the experimental results was achieved by all 3 cases with a minimum deviation of 0.34% when using euler walls with the SST model and a maximum deviation of 6.31% for $\alpha = 8°$ when using the combination symmetry plane/SA. This good correlation between experimental results and numerical for the lower angels of attack, evidences that there is not a setup problem associated with the calculations but that in fact, once flow separation starts playing in, around $\alpha = 7°$, there is a major shift in the prediction of the flows physics. This evidences the need of using time resolved methods to tackle the unsteady nature of the flow.

Figure 5.2, depicts the streamwise friction coefficient (Cf_x) when using the symmetry plane/SST combination at $\alpha = 10°$ for the midspan position. The fact that, on the suction side, the streamwise friction coefficient keeps decreasing upstream of the leading edge and towards the trailing edge, indi-

cates that the model does not predict the transition to turbulent flow within this interval as it would be expected in these conditions. The disparity between numerical and experimental results in figure 5.1 is, as previously mentioned, a consequence of this inability by part of the turbulence model in dealing with transition from laminar to turbulent flow.

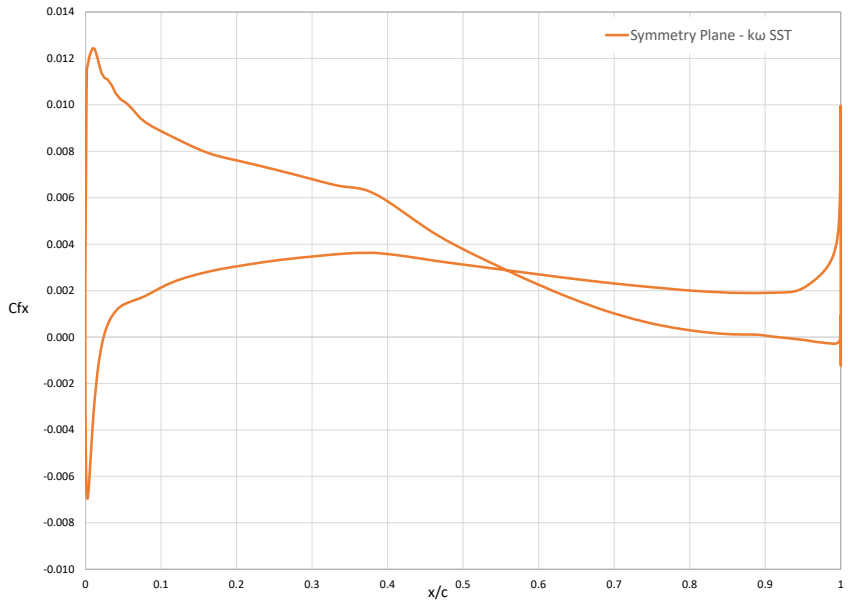

Figure 5.2: Cf_x at $\alpha = 10°$.

In terms of drag coefficient prediction, the results for all the cases are shown in figure 5.3 below.

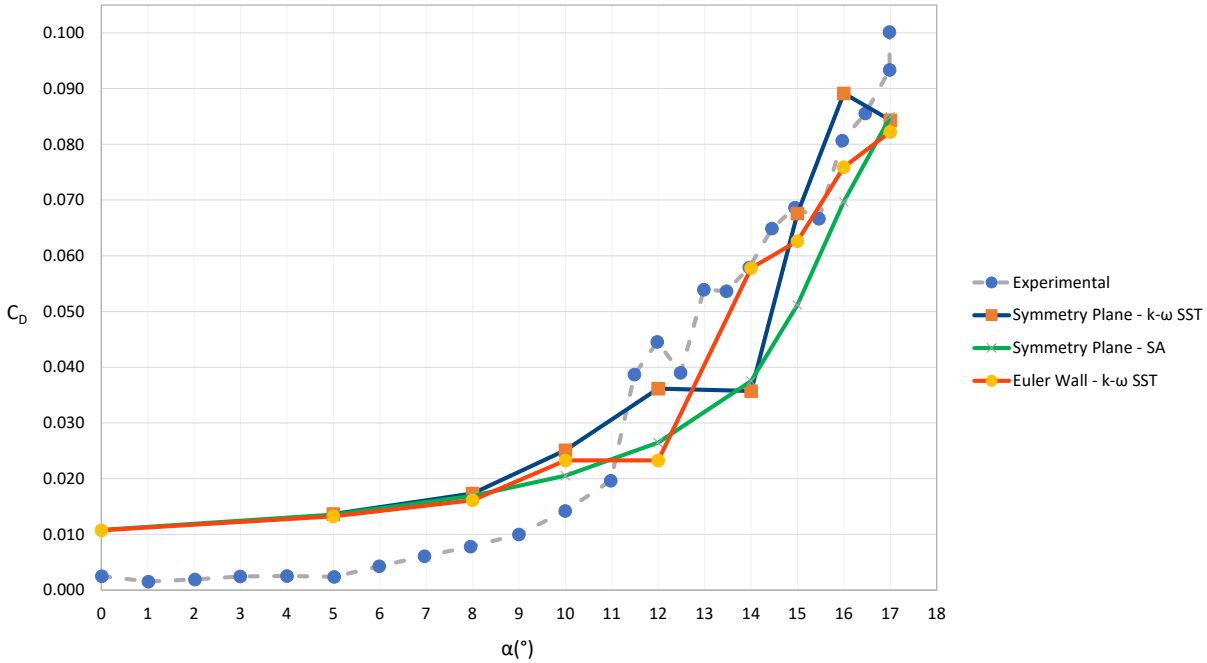

Figure 5.3: Steady RANS drag coefficient polar curve.

For all cases, the drag coefficient is overly predicted in the low angle of attack region. This is also an effect of the fully turbulent flow conditions around the wing, unlike in the experiments, which cause the drag coefficient to increase. However, the earlier separation in the experimental causes a steep increase in the drag coefficient making it under predicted from $\alpha = 11°$ onwards. The symmetry plane/SA and euler wall/SST cases verified this under-prediction trend while the symmetry plane/SST combination predicted a higher C_D at $\alpha = 16°$, from where on it became under-predicted again.

The over prediction of lift allied with the under prediction of drag, meet the work of Manolesos et al. [5] that attributed this effect to the delayed formation of stall cells which will be investigated further in sections 5.1.3 and 5.2.3.

5.1.2 Pressure Distributions

In this next section, the comparisons between experimental and numerical results will be made by means of the pressure coefficient on the wing's surface. An initial overview regarding the location of the data points used will be given, followed by the assessment of the pressure data results. The results will be shown for 3 angles of attack. The first one being $\alpha = 5°$ as a reference point, given the good agreement reached in the previous section, followed by the cases were flow separation is stronger and that were simulated using the URANS approach: $\alpha = 12°$ and $\alpha = 16°$.

5.1.2.1 $\alpha = 5°$

As a starting point for the pressure coefficient distributions comparison, the results obtained for a lower angle of attack were plotted, given the good agreement between steady RANS and experiments shown in the previous section. Figure 5.4 depicts the Cp distributions for all the steady RANS cases and the experimental. The slightly lower C_L value obtained from the simulations is visible through the under-prediction of the minimum pressure point as well as in the intervals of $x/c = 0$ to $x/c = 0.5$ and $x/c = 0.7$ to $x/c = 0.8$ as it is shown in the figure. Among the factors that might contribute to these deviations, the inability to capture the transition from the laminar regime to turbulent at lower angles of attack is something that must be considered given that fully turbulent conditions are being assumed with the selected models. Overall, it can be stated that all cases were able to make a satisfying prediction of the Cp distribution for a low angle of attack.

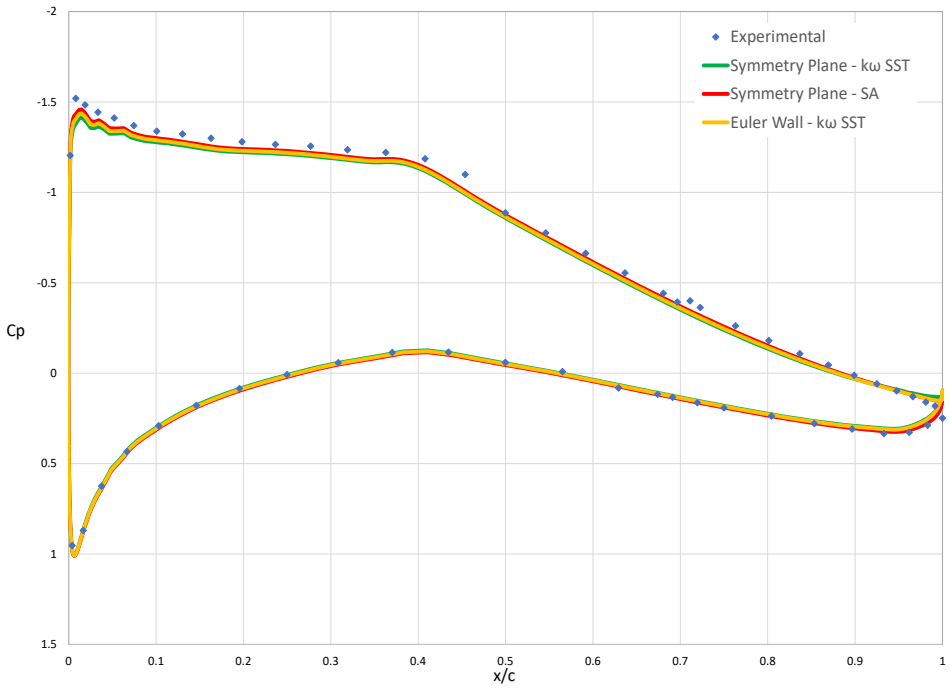

Figure 5.4: Cp distribution at midspan position for Steady RANS with $\alpha = 5°$

5.1.2.2 $\alpha = 12°$

The $\alpha = 12°$ case, unlike the two previous cases, is within the region where the numerical results discrepancy from the experimental ones is more accentuated. The results from the steady cases are shown in figure 5.5 and it becomes clear that the steady approach has problems in predicting the flows physics on the suction side due to its highly unsteady nature. From the experimental results, one can identify the flow's separation region from $x/c = 0.5$ to $x/c = 1$ due to the constant Cp value verified in this area. Regarding the numerical results, on the pressure side, there is a slight over-prediction starting at $x/c = 0.1$ and, on the suction side, there is an over-prediction as well starting from the suction peak until $x/c \approx 0.65$, from where on, the results became under-predicted up to the trailing edge. Overall the symmetry plane/SST and euler wall/SST combinations show better agreement than the symmetry plane/SA one. The constant Cp values from approximately $x/c = 0.65$ on, reveal a later separation point in the numerical results.

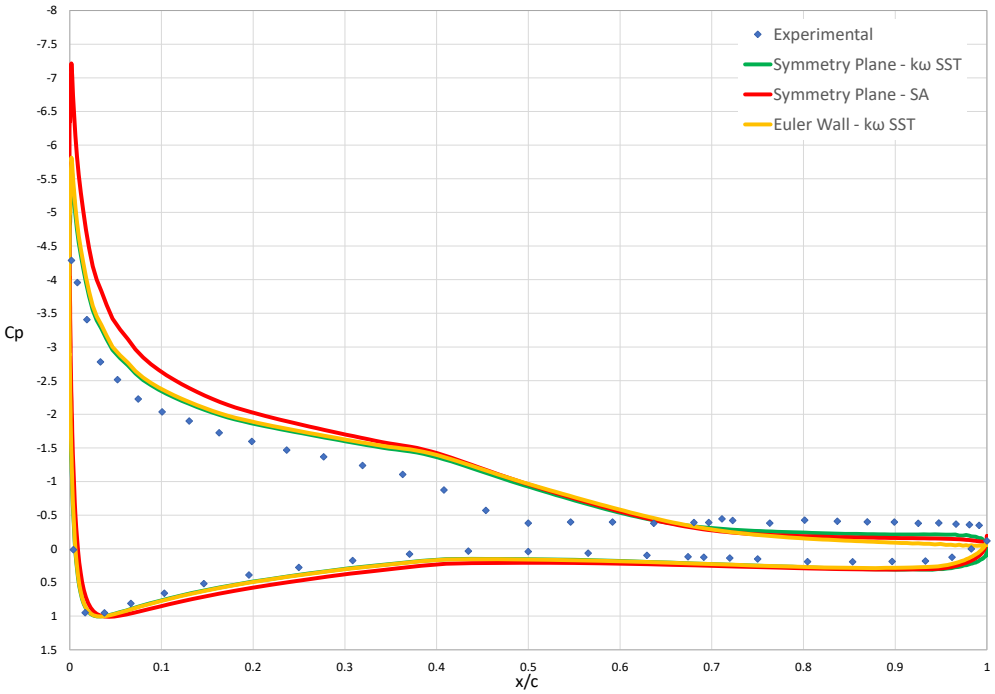

Figure 5.5: Cp distribution at midspan for Steady RANS with $\alpha = 12°$

5.1.2.3 $\alpha = 16°$

Figure 5.6 depicts the Cp distributions for all the steady RANS simulations performed together with the experimental results for $\alpha = 16°$. For this particular case, the symmetry plane/SST combination reached a decrease of 4 orders of magnitude both in the force and density residuals, the symmetry plane/SA a decrease of 5 orders of magnitude in the force coefficients and 4 orders of magnitude in the density residual, while the euler wall/SST combination achieved a decrease of 5 orders of magnitude in the force residuals and of 3 in the density residual. For all cases, given the flow conditions, oscillations in the residuals were visible, thus revealing the difficulty of the steady approach in dealing with this flow regime.

In the force coefficient's comparison from the previous chapter, there was a clear difference between the calculations and the experiments within this flow regime. An initial look at the Cp distributions shows that the suction peak predicted by the simulations, below $Cp = -7$ for all cases, is much lower than the experimental one of approximately $Cp = -5.5$, with the symmetry plane/SST predicting the weakest suction peak amongst the three numerical cases. It is also clear, as in the previous cases, that the suction side of the airfoil has a more significant impact in the discrepancy between computational and experimental results given the large region of flow separation that was identified and the consequent unsteady behaviour that is not able to be captured by steady RANS. The symmetry plane/SST combination reveals a better agreement with the experimental results and predicts the start of the constant Cp zone associated with flow separation closely to the experimental one. Taking into account the three dimensionality of the flow and that the Cp distributions were plotted for the midspan position, the differences found between the numerical approaches shall be further investigated in the next section when

analysing the flow separation patterns.

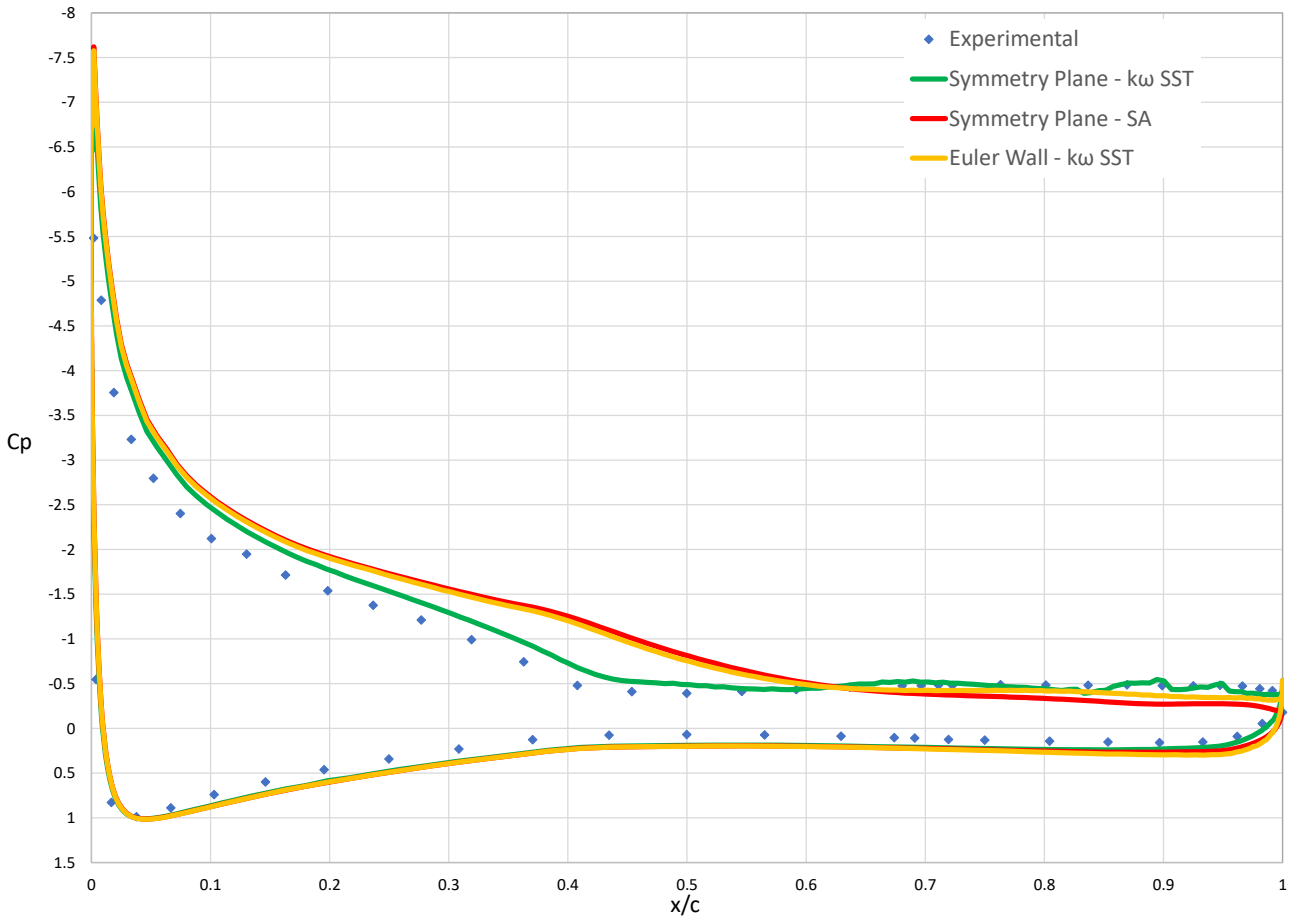

Figure 5.6: Cp Distribution over Wing for Steady RANS with $\alpha = 16°$.

5.1.3 Flow Separation and Stall Cells

In the experimental runs, for $\alpha = 10^\circ$ (Figure 3.3), the separation line revealed a sinusoidal wave pattern whose front extended from $x/c = 0.8$ up to $x/c = 0.6$. Near the wind tunnel walls, a small separation area is also visible which pushed the separation line forward again. As the angle of attack increased, the wave length of the separation line increased and, from $\alpha = 12^\circ$ (figure 3.4) onwards, it became limited by the wind tunnel walls so that only one cell fits into the span. Also, distinctive cellular patterns i.e. stall cells, were identifiable on the surface in the near wall region. This shape became constant from this point on, only moving further up the chord as the angle of attack increased. For $\alpha = 15^\circ$ and $\alpha = 16^\circ$, shown in figures 3.5 and 3.6 respectively, the reported separation pattern was very similar, with the separation line maxima located at around $x/c = 0.42$ for $\alpha = 15^\circ$ and at $x/c = 0.4$ $\alpha = 16^\circ$. Available videos from the experimental test also show that the separation line follows an approximately stationary behaviour.

For all the figures shown in this section, the areas with a positive friction coefficient along the x axis ($Cf_x > 0$) are shown in red whereas the ones with $Cf_x < 0$ are represented in blue. The transition line between the red and blue area, depicts the separation front where $Cf_x = 0$ and the freestream flow is flowing along the x axis.

5.1.3.1 $\alpha = 12^\circ$

Figure 5.7 shows the separation patterns obtained for all steady cases with $\alpha = 12^\circ$ for which the experimental separation line maximum was located at approximately $x/c = 0.5$. The one cell separation pattern identified in the experiments and shown in figure 3.4 was unable to be reproduced. The symmetry plane/STT combination revealed the earliest separation point along the chord, located at $x/c = 0.63$ and also the minimum value in the separation line ($x/c = 0.93$), resembling the wavy motion reported by the experiments at $\alpha = 10^\circ$ in figure 3.3. This resemblance might be caused by the delay in stall cells formation in the numerical solution as it was also encountered by Manolesos et al. [5]. The symmetry plane/SA and euler wall/SST cases, captured a straighter separation line oscillating between $x/c = 0.63$ and $x/c = 0.76$ for the former and between $x/c = 0.74$ and $x/c = 0.85$ for the latter. In terms of stall cells, the formation of this pattern was clearly visible for the symmetry plane/SST combination, unlike in the other two cases.

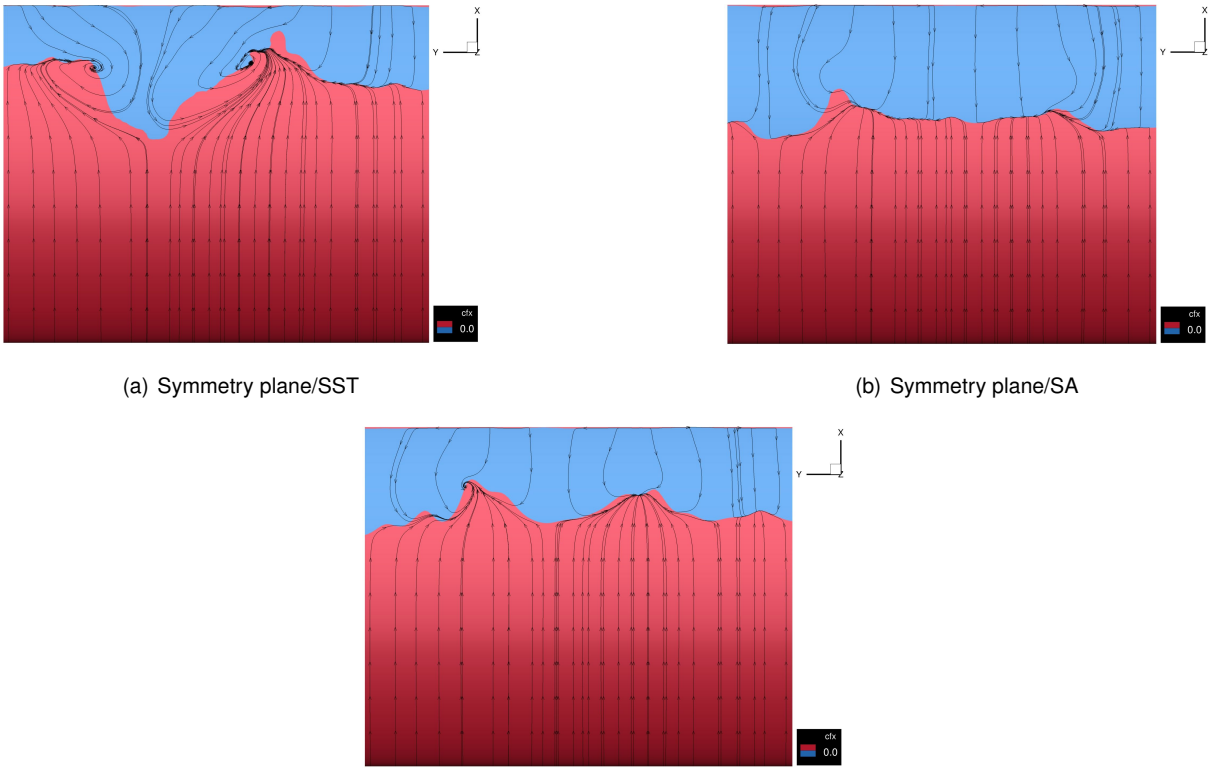

(a) Symmetry plane/SST

(b) Symmetry plane/SA

(c) Euler wall/SST

Figure 5.7: Cf_x and streamlines on suction side for $\alpha = 12°$

5.1.3.2 $\alpha = 16°$

Figure 5.8 shows the results obtained with the steady simulations for $\alpha = 16°$. The symmetry plane/SA and euler wall/SST combinations, showed in (b) and (c) respectively, although having the separation line maximum located just slightly above the experimental one, $x/c = 0.435$ for symmetry plane/SA and $x/c = 0.43$ for euler wall/SST, revealed to be inadequate in correctly predicting the separation pattern showed in figures 3.5 and 3.6, placing the pair of counter rotating vortices in the center of the wing and capturing a very different separation line shape. The symmetry plane/SST combination (figure 5.8 (a)), on the other hand, managed to more accurately reproduce the separation pattern. It showed a good agreement in the midspan region by placing the separation line maxima at approximately the $x/c = 0.42$ region with the deviations increasing as we move closer to the wall. However, three vortex structures can be identified on the surface whereas only two were reported from the experimental run. The differences in Cp distributions found in the previous section are explained by the discrepancies found in the separation patterns presented here.

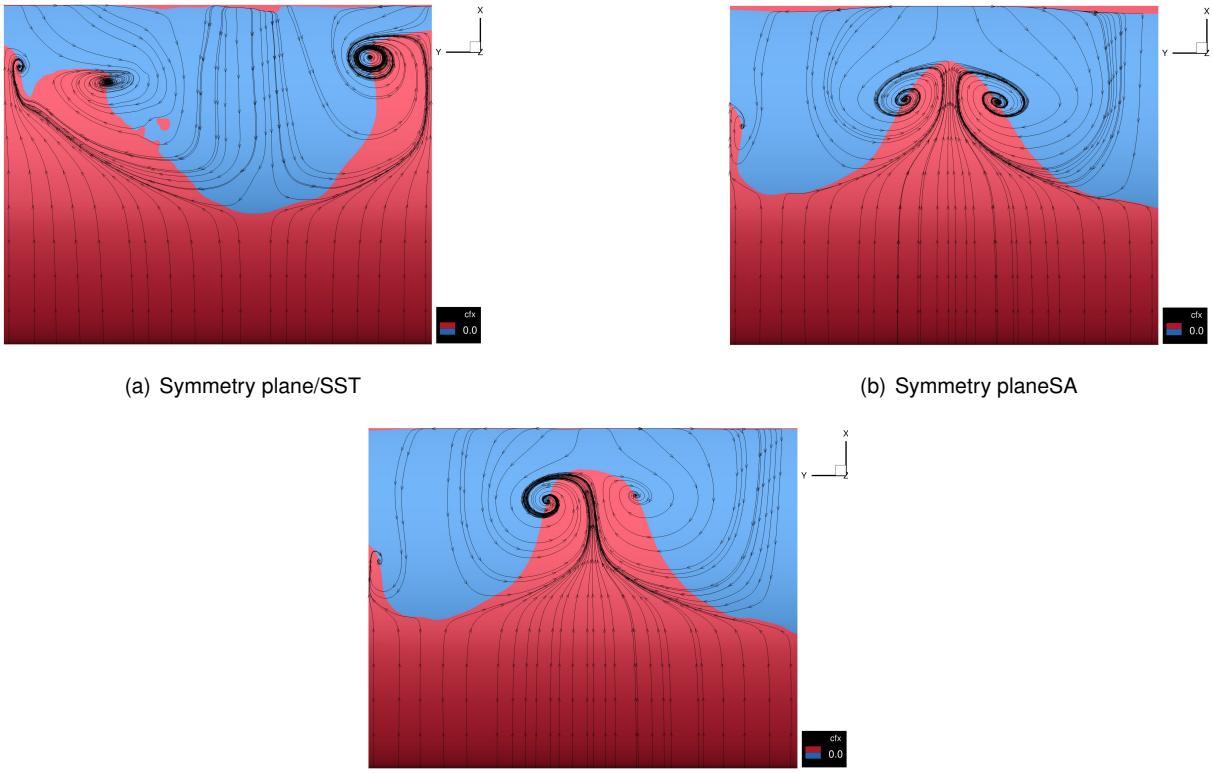

(a) Symmetry plane/SST

(b) Symmetry planeSA

(c) Euler wall/SST

Figure 5.8: Cf_x and streamlines on suction side for $\alpha = 16°$

In terms of force coefficients prediction, the three combinations showed similar results, with the symmetry plane/SA and euler wall/SST cases evidencing a slightly better behaviour regarding the C_L evolution in figure 5.1. When looking at the pressure distributions and separation patterns, it could be argued that for the $\alpha = 12°$ case, there is not a combination that clearly overcame the others in terms of predictions however, the $\alpha = 16°$ case, showed very distinct separation patterns between the symmetry plane/SST combination and the other two, that reflected itself in the Cp distribution. The pair of counter-rotating vortices predicted by the former, showed good correlation in terms of their spanwise position and rotation direction. Given this significant gap in the separation pattern prediction and taking into account that the results from the wake analysis that will be performed in a later section for $\alpha = 16°$ at the midspan position are strongly influenced by the separation location, the symmetry plane/SST combination was chosen for the beginning of the unsteady RANS investigation.

5.2 Unsteady RANS

5.2.1 Force Coefficients

As mentioned in chapter 4, for the time accurate calculations, 3 angles of attack were selected ($8°, 12°$ and $16°$). For the reasons pointed out in the previous section, the starting point for the unsteady simulations was the symmetry plane/SST combination and throughout the course of the work, this combination yielded the most satisfying results in terms of the URANS approach. Thus, from now on, when referring to URANS, it will always be to the symmetry plane/SST case up to section 5.3, where the particularities of time resolving methods with the euler wall boundary condition will be addressed. The number of time steps that were able to be performed is highly dependent on the time range available. Thus, for this particular work, the available time allowed to simulate 11380 time steps for each angle of attack, which does not guarantee statistical convergence for all cases.

5.2.1.1 $\alpha = 8°$

In the experimental testing, the lowest α case ($8°$), marked the beginning of unsteady behaviour in the flow around the wing. The results from the steady calculations, both for the SST and SA model, also revealed a small separation area starting in the trailing edge therefore, the unsteady calculations for this α are expected to present a weak time dependent behaviour. The progress of C_L and C_D over time is depicted in figure 5.9 below.

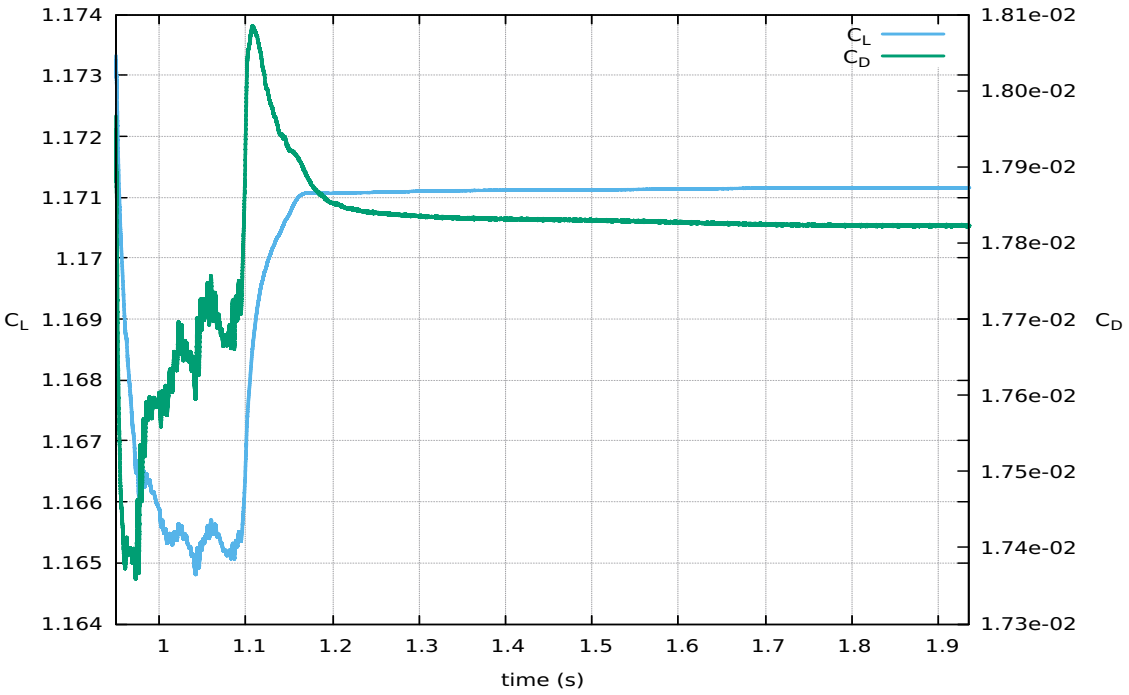

Figure 5.9: C_L and C_D over time for $\alpha = 8°$

As expected, the solution evolved into an almost steady state as time progressed. Small oscillations are still visible in the plot, likely due to trailing edge instabilities at an early stage of flow separation.

Computing the mean starting from where the solution started to settle ($t = 1.4s$), reveals a mean C_L value of 1.171. This value is slightly closer to the experimental one ($C_{L_{exp}} = 1.142$) than the steady solution ($C_{L_{steady}} = 1.184$).

5.2.1.2 $\alpha = 12°$

For the next case, the angle was increased by $4°$ up to $\alpha = 12°$. The flow conditions for this angle of attack are expected to reflect a stronger unsteady behaviour than the previous one given the increase of the separation region. The C_L and C_D progress is shown in figure 5.10.

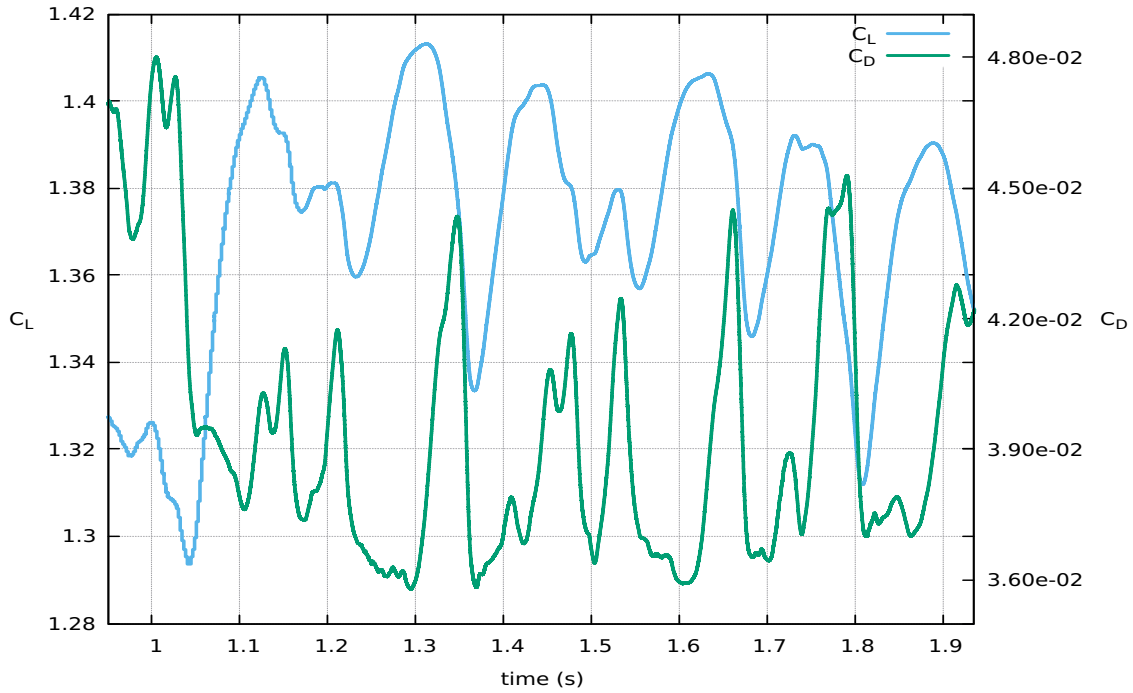

Figure 5.10: C_L and C_D over time for $\alpha = 12°$

As stated, the increase in the angle of attack and consequently the separation area, caused the force coefficients to oscillate more over time in comparison with the $\alpha = 8°$ case. The simulation was performed for 11380 time steps but it was unable to attain statistical convergence, meaning that changes in the mean flow were still occurring as the simulation time progressed. Large scale motion can be seen, as well as smaller scale fluctuations. A deeper insight on the frequencies that are being captured in this simulation, will be given in 5.2.5 as mean to investigate the validity of URANS for this case. However, the maximum within the interval of values in which the C_L is inserted over time ($C_L = 1.41$), is still lower than the one obtained in the steady calculation for the same case $C_{L_{steady}} = 1.51$, being an initial good indicator of the better performance of the time resolving approach.

5.2.1.3 $\alpha = 16°$

The last case of the unsteady calculations focus is the $\alpha = 16°$ case shown in figure 5.11.

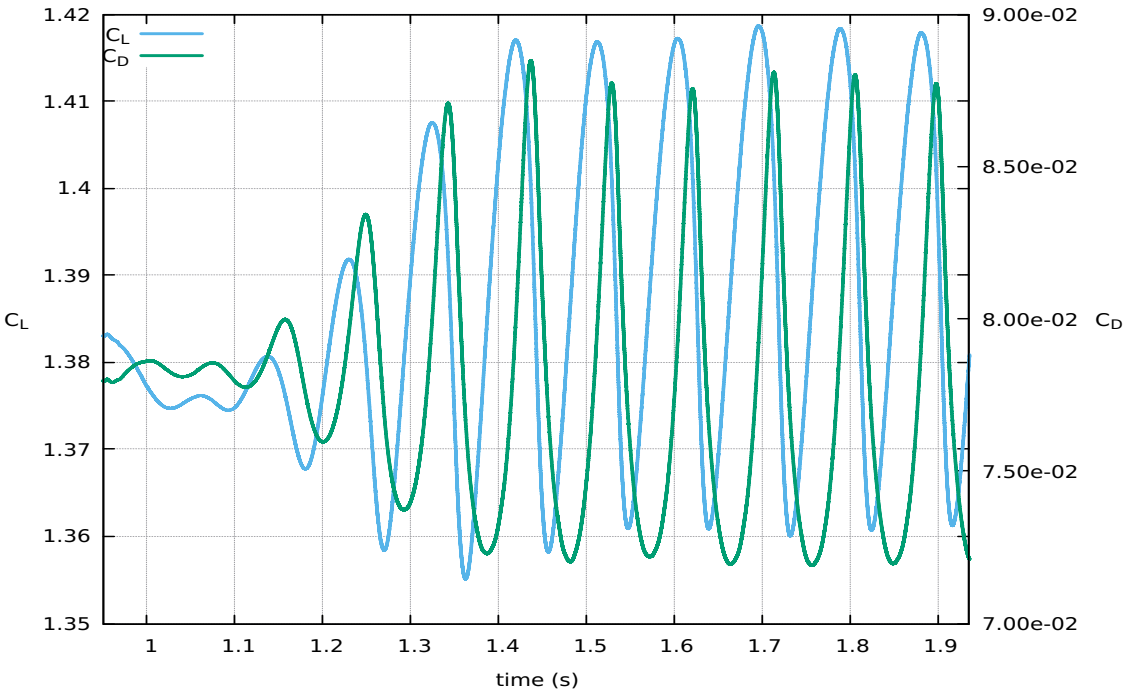

Figure 5.11: C_L and C_D over time for $\alpha = 16°$.

Again, like in the previous case, the flow conditions produced strong oscillations over time both in terms of C_L and C_D. However, this new flow regime enabled the capture of a periodic behaviour, showing that URANS might be a good choice to simulating these flow conditions given that no medium scale fluctuations are present in the force coefficients. Starting from around $t = 1.4s$, the unsteady behaviour is almost fully established and behaving in cycles with a mean period of $\overline{\Gamma} = 0.092s$. The simulation can not be considered statistically converged as there are still oscillations in both the minimum and maximum values of C_L and C_D however, it can be deemed satisfying. This fact suggests that there might be a larger scale phenomena taking place that can not be captured by the current time step. The mean C_L value for this case, taken from the point where the unsteadiness started to settle onwards is of $C_L = 1.385$ thus also decreasing in comparison with the steady calculations $C_{L_{steady}} = 1.54$ and moved closer to the experimental value $C_{L_{exp}} = 1.25$. Again, this mean C_L value is dependant on the time interval that one chooses to compute it but it is worth pointing out that even so, the mean C_L for this unsteady calculation will always be lower than the one from the steady calculations given the maximum value obtained ($C_L = 1.42$), therefore showing again the need of using time resolving methods for such flow conditions.

When using the RANS approach, there is no guarantee that the turbulence model is able to filter every frequency, thus further investigation regarding the frequencies obtained for the $\alpha = 12°$ and $\alpha = 16°$ is given later in section 5.2.5 by means of a spectral analysis.

5.2.2 Pressure Distributions

In this section, as in the steady RANS one, the pressure coefficient on the wing's surface will be compared with the experimental data and the differences between the steady approach and unsteady will be shown by means of the results obtained for the same case: symmetry wall/SST. A more detailed analysis will be performed for the $\alpha = 16°$ case given the near statistically converged behaviour reported in the previous section. The mean pressure coefficient ($\overline{Cp}$) for the unsteady cases refers to the mean obtained at the last time step of the run and for all the wing surface plots presented, the freestream is flowing along the x axis.

5.2.2.1 $\alpha = 8°$

The $\alpha = 8°$ case is within the region where the discrepancy between the steady RANS results and the experimental ones begins. The origin of such behaviour, as pointed out before, most likely lies within the appearance of small scale fluctuations in trailing edge due to initial flow separation, and it was captured by the unsteady run. Figure 5.12 shows the mean Cp distribution for the unsteady run and the Cp distributions for the steady and experimental cases. The plot reveals a small deviation in the results for the pressure side but a slightly more accentuated one the suction side near the trailing edge. In this case, RANS and URANS capture approximately the same pressure distribution which might be due to small scale fluctuations within this flow regime that cannot be simulated with the URANS approach.

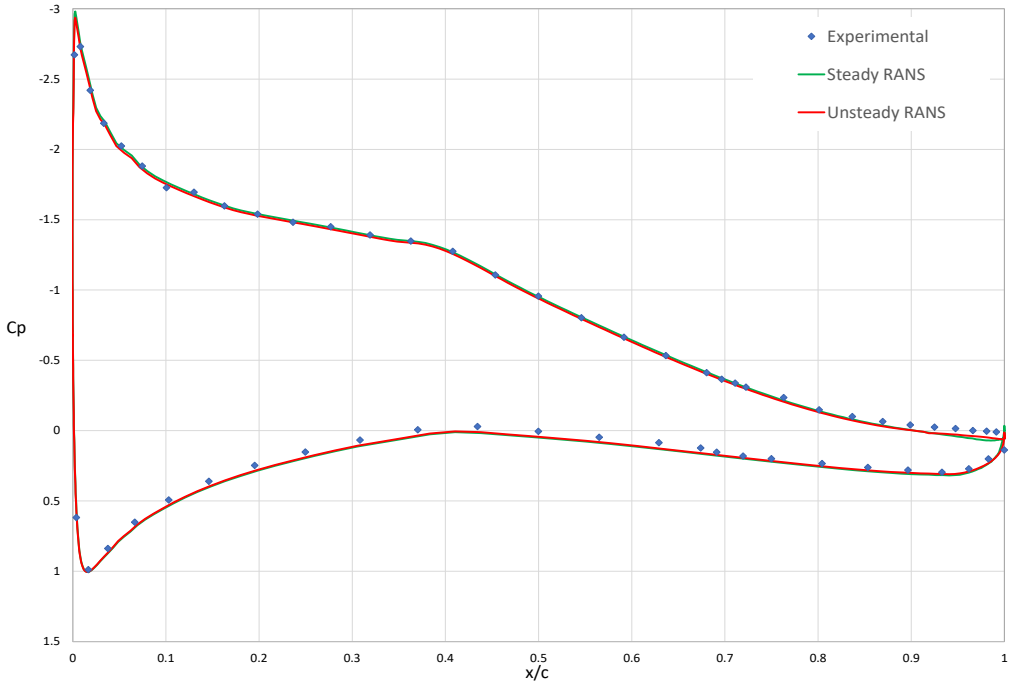

Figure 5.12: RANS vs URANS Cp distribution at midspan for $\alpha = 8°$

Computing the root mean square values of the pressure coefficient (Cp_{rms}), provides a better understanding into which areas of the wing reveal a stronger deviation within the $\overline{Cp}$ values over time. Figure 5.13 shows the Cp_{rms} values for the suction side of the wing and it is clear that, given the range of the

values, there are very small fluctuations over the wing ($Cp_{rms_{max}} = 0.008$). However, the higher Cp_{rms} values concentrated in the trailing edge confirm that the small fluctuations captured are related to a trailing edge instability during an initial stage of flow separation, as reported by the experiments, and are in part responsible for the initial discrepancy in terms of C_L verified between numerical and experimental results.

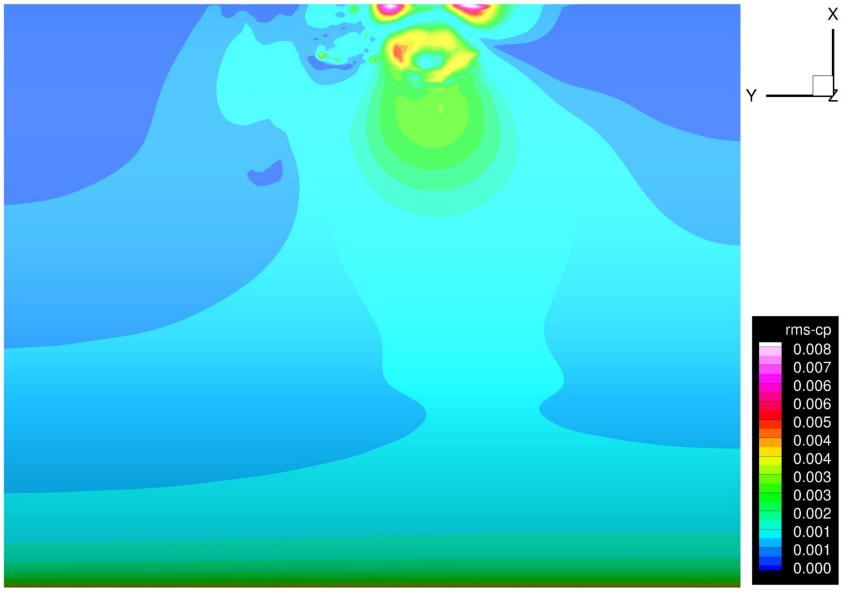

Figure 5.13: Cp_{rms} on suction side for $\alpha = 8°$.

5.2.2.2 $\alpha = 12°$

The differences obtained when switching to unsteady, for the $\alpha = 12°$ case, can be consulted in figure 5.14, where the mean Cp values from the unsteady run are plotted together with the Cp distributions for the steady and experimental results. Albeit a significant gap still exists between the unsteady results and the experimental, the time resolving method managed to narrow it in comparison with the steady. Although a small difference is visible on the pressure side, the suction side is still the more affected region of the wing in terms of the difference to the experimental results. The constant Cp values on the suction side that are associated with flow separation were predicted further upstream ($x/c = 0.6$) than in the steady simulation, indicating a better prediction of the separation position. Given the force coefficient's evolution over time (shown in figure 5.10), one has to consider that URANS is not able to capture the flows physics at medium scales, which might be a possible reason for the observed numerical error.

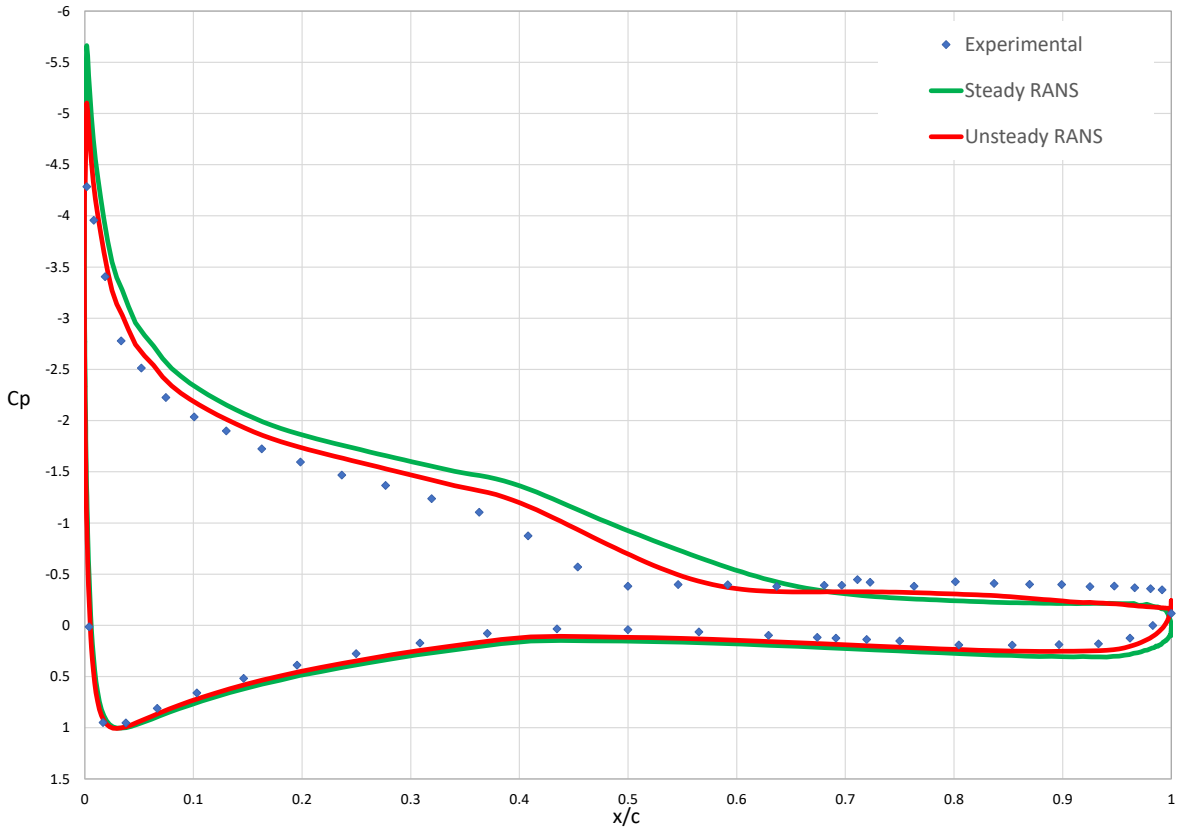

Figure 5.14: RANS vs URANS Cp distribution at midspan for $\alpha = 12°$

The Cp_{rms} distribution along the chord at the midpsan position for the unsteady run depicted in figure 5.15, reveals the suction peak and mid-chord areas as the ones with a higher deviation from the mean values. The peak observed at $x/c = 0.5$ is possibly associated with with the movement of the separation location and the higher values between $x/c = 0.7$ and $x/c = 1$ are probably due to fluctuations of the separated flow. It must also be taken into account the highly three dimensional behaviour of the flow in these conditions, for that matter, the Cp_{rms} was plotted on the suction side of the wing, along with the mean separation line (depicted in black), as is shown in Figure 5.16. The values on the surface reveal a higher deviation from the mean near the center of the suction side (in accordance with the results from figure 5.15) and overall, the right-hand side of the wing shows higher Cp_{rms} values than the left one. The differences in the Cp distribution between the maximum registered C_L value ($C_{L_{max}} = 1.413$ at $t = 1.3129s$) and the minimum ($C_{L_{min}} = 1.312$ at $t = 1.8088s$) are shown together with the separation line in Figure 5.17 where again, we can see the highest deviations occurring at the center of the wing and on the right-hand side, where the more accentuated shift of the separation line takes place.

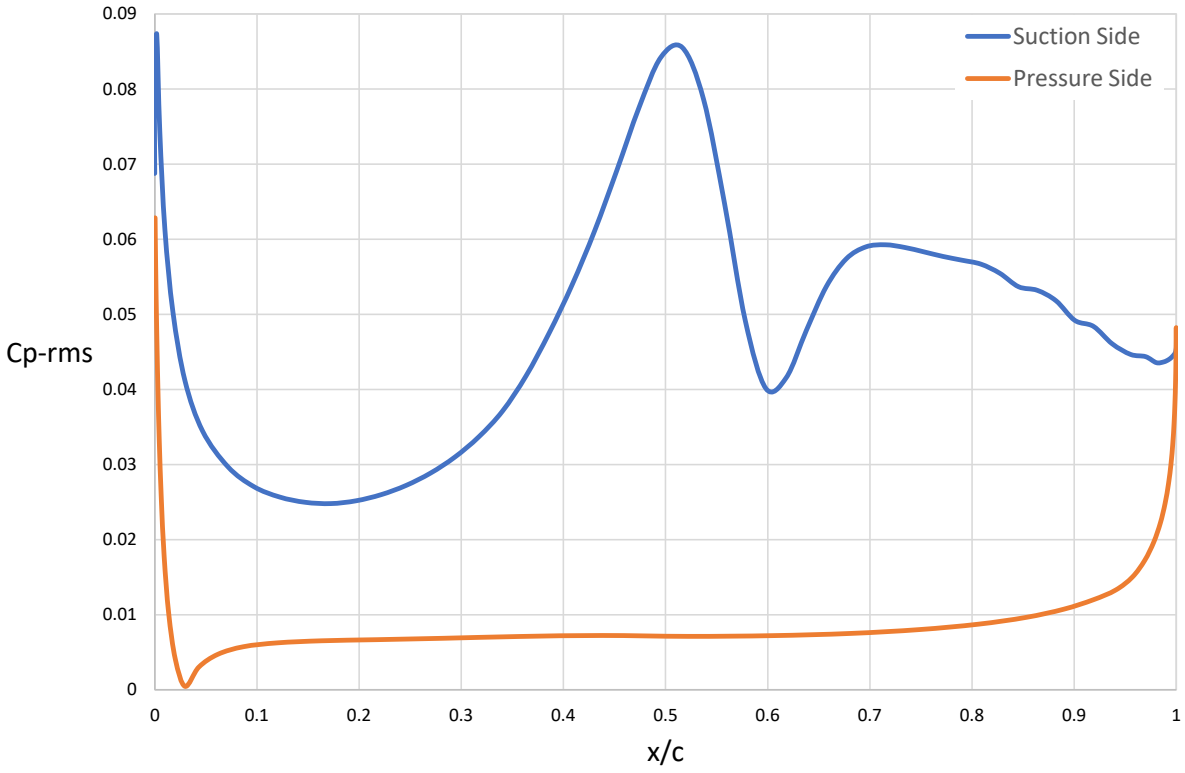

Figure 5.15: Cp_{rms} along chord at midspan for $\alpha = 12°$

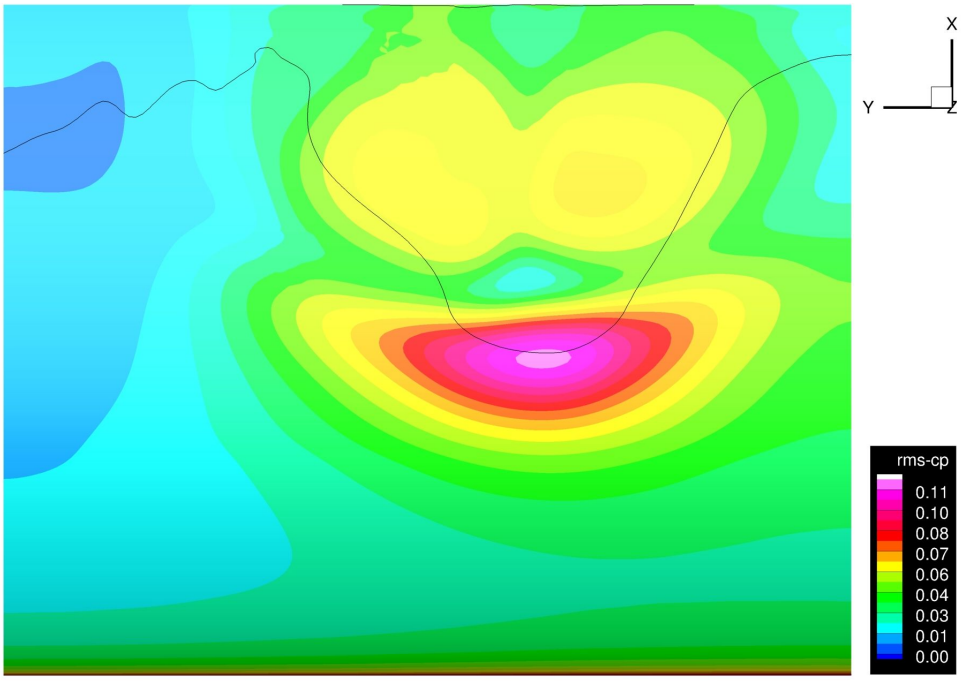

Figure 5.16: Cp_{rms} on suction side and mean separation line for $\alpha = 12°$.

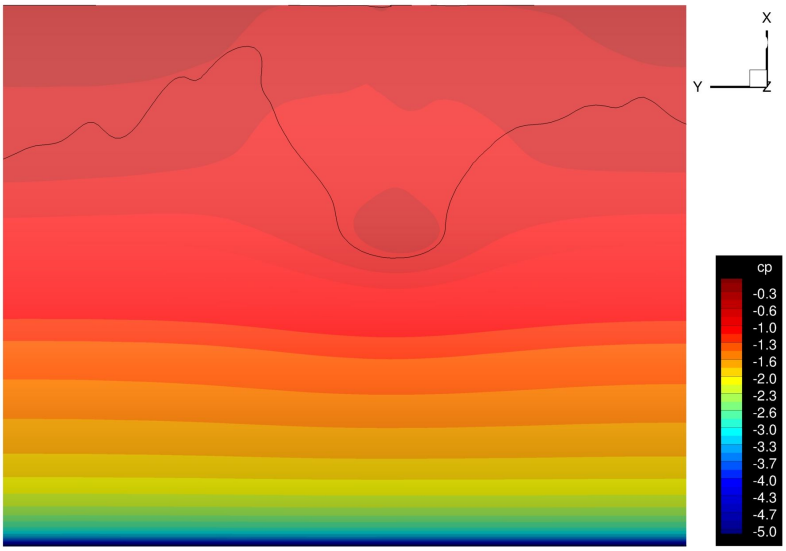

(a) $C_{L_{max}}$

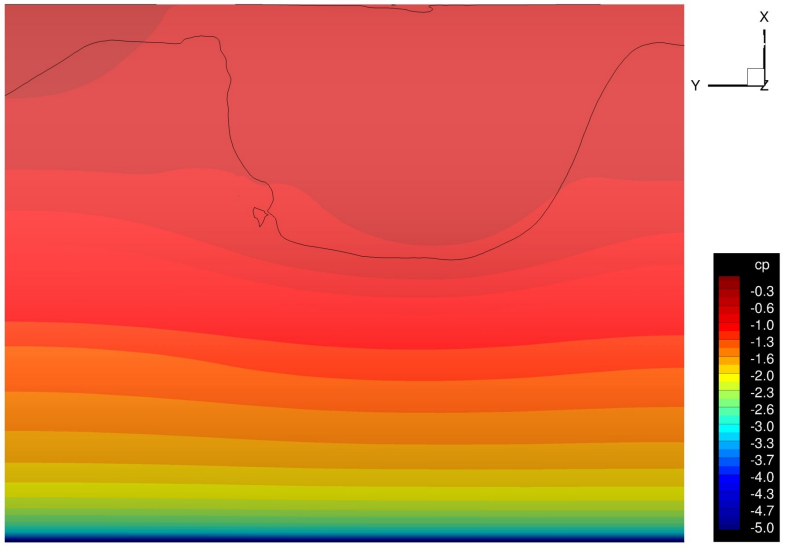

(b) $C_{L_{min}}$

Figure 5.17: $C_{L_{max}}$ and $C_{L_{min}}$ Cp distributions and separation line for $\alpha = 12°$

5.2.2.3 $\alpha = 16°$

For the $\alpha = 16°$ case, a better agreement was reached as well for the Cp distributions at the midspan position. Figure 5.18 shows the results for the unsteady, steady and experimental runs. The mean suction peak value for the unsteady case ($\overline{Cp} = -6.7$), although still higher than the experimental one, improved when compared with the steady simulation.

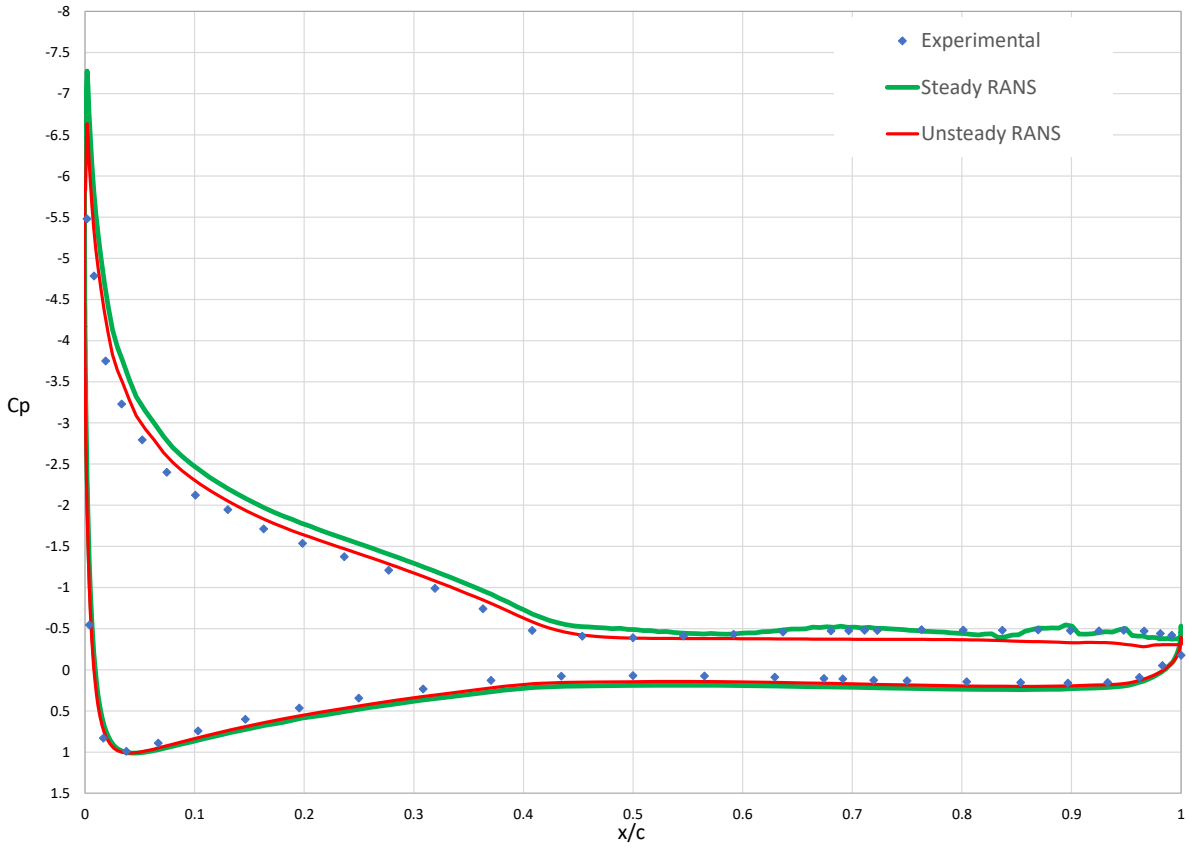

Figure 5.18: RANS vs URANS Cp distribution at midspan for $\alpha = 16°$

In terms of the pressure side distribution, there was a slight improvement as well but the more distinctive one took place on the suction side. The gap existent between $x/c = 0$ and $x/c = 0.6$ was shortened when switching to the time resolving method however, some accuracy was lost from $x/c = 0.6$ onwards. As is shown, the position associated with flow separation and at which the $\overline{Cp}$ values become constant, was predicted very closely to the experimental. The fact that the $\alpha = 16°$, unlike the former case, managed to capture a periodic motion, indicates the possibility of a smaller numerical error thus the better correlation when compared with the $\alpha = 12°$ case.

Figure 5.19 shows the root mean square values of the Cp at the midspan position. As expected, taking into account the previous results, the areas were unsteadiness reveals a stronger presence are the leading edge and throughout the suction side. Peaks in the Cp_{rms} values are distinguishably visible at the suction peak and at $x/c = 0.4$ on the suction side. The latter is near where the separation front is located and the strong unsteady nature of this region is most responsible for the higher oscillations of the Cp. From $x/c = 0.5$ to $x/c = 1$, the Cp_{rms} values on the suction side show some oscillations also due to the separated flow's unsteadiness in that area.

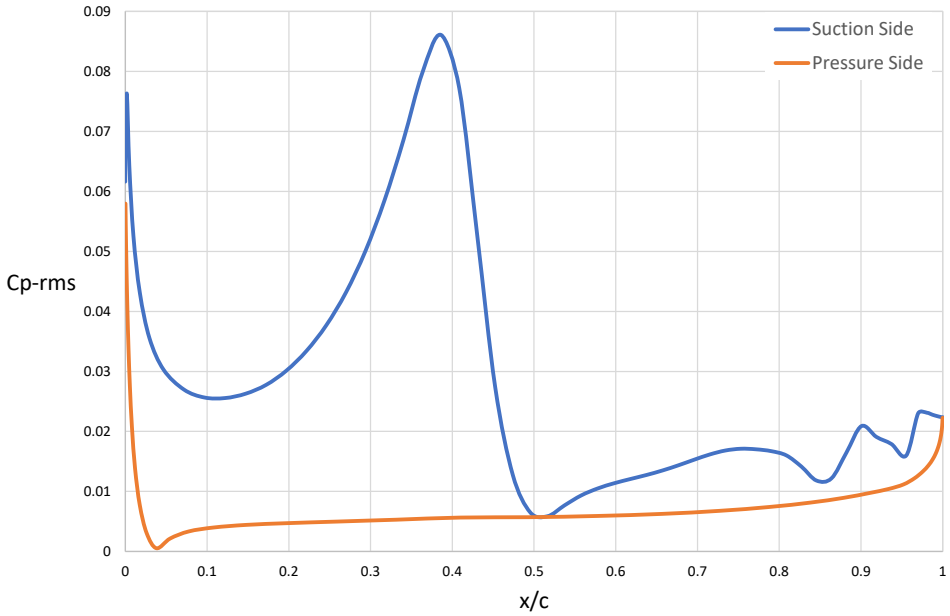

Figure 5.19: Cp_{rms} along chord at midspan for $\alpha = 16°$

However, it must also be considered as in the previous case, the highly three dimensional behaviour of the flow in these conditions, as reported in the experiments. For a better insight in how the Cp is changing, a plot depicting the Cp_{rms} on the suction side of the wing, together with the mean separation line (in black), is shown in figure 5.20.

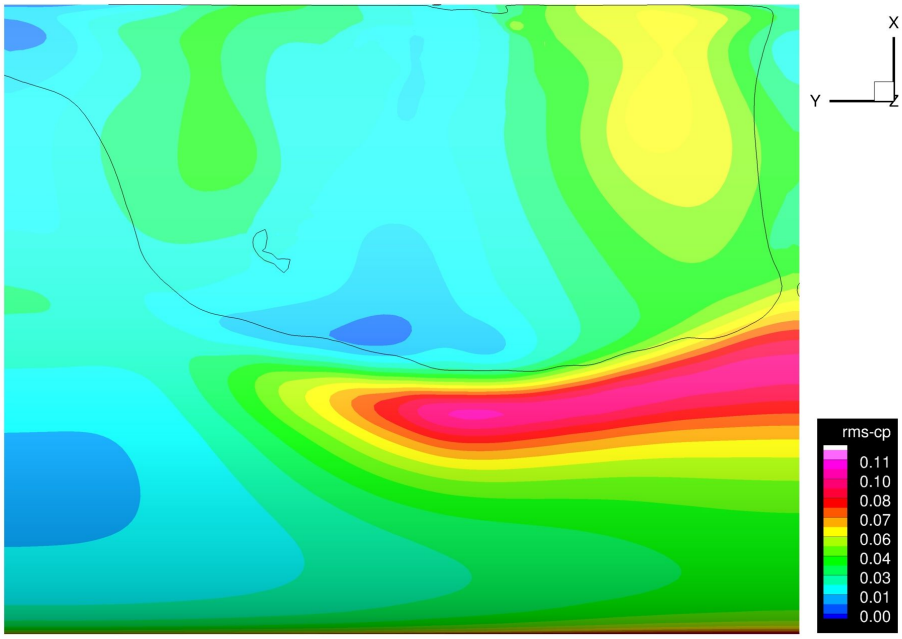

Figure 5.20: Cp_{rms} on suction side and mean separation line for $\alpha = 16°$.

The three dimensional behaviour previously mentioned is verified with stronger changes in the Cp values on the right-hand side of the wing and approximately at $x/c = 0.4$. In order to better understand the magnitude of the changes from one span position to the other, in Figure 5.21 the Cp_{rms} was plot-

ted along the chord for three different span positions. It is clear by this figure now, that in addition to the suction peak region, the right-hand side of the wing is more subjected to the flow's unsteadiness. After the $x/c = 0.4$ point, the midspan region becomes more stable in comparison with the outer span areas, mostly due to the stall cell and separation line behaviour found in those locations, which will be addressed in the following section.

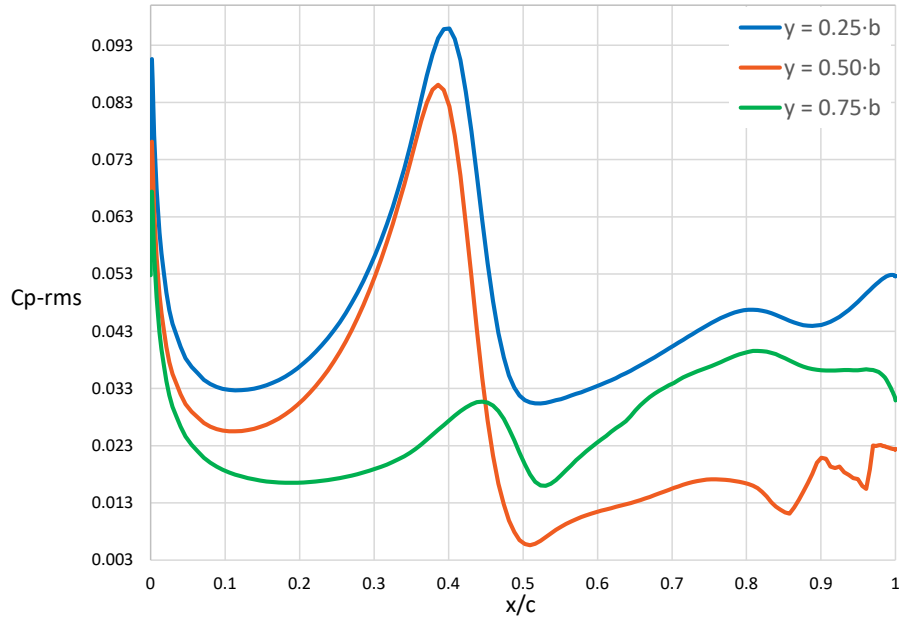

Figure 5.21: Cp_{rms} on suction side at different spanwise positions for $\alpha = 16°$.

The $\overline{Cp}$ was also plotted for each span position and can be seen in figure 5.22. The low Cp_{rms} verified for $y/b = 0.75$ at approximately $x/c = 0.4$ is accompanied by a higher sectional Cp distribution when compared with the two other midspan positions.

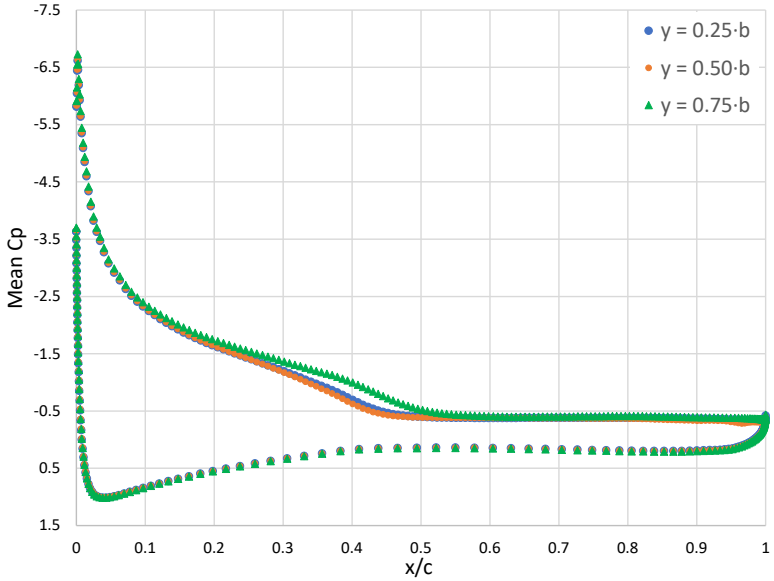

Figure 5.22: Mean Cp on suction side at different spanwise positions for $\alpha = 16°$.

It is also possible to verify the different influence of each section on the periodical behaviour of the C_L by looking at the Cp distributions for the minimum C_L (≈ 1.336 at $t = 1.73223s$) and maximum (≈ 1.418 at $t = 1.78885s$) obtained during the simulation. Figure 5.23 shows this distribution at the midspan location and barely any significant difference is visible in this section.

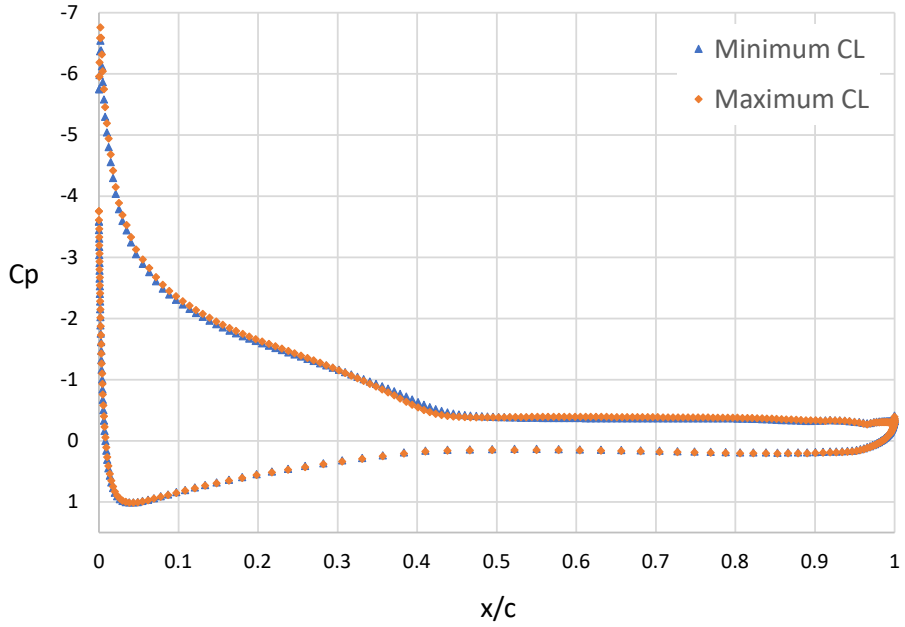

Figure 5.23: $C_{L_{max}}$ and $C_{L_{min}}$ Cp distributions at midspan position for $\alpha = 16°$.

However, the same analysis at $y/b = 0.25$ reveals a more accentuated gap between the suction side Cp distributions due to the larger changes in Cp taking place in this region.

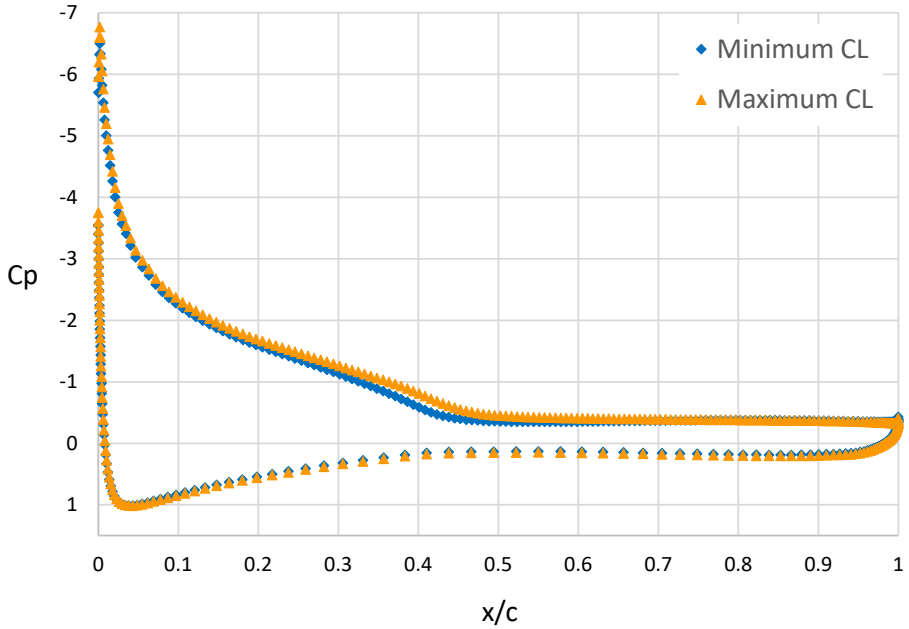

Figure 5.24: $C_{L_{max}}$ and $C_{L_{min}}$ Cp distributions at quarterspan position for $\alpha = 16°$.

In 5.25 the Cp distributions for the minimum and maximum lift obtained in a cycle are plotted, together with the separation line, on the suction side and, again, the most visible difference in the values takes place on the right-hand side of the wing where a higher decrease in Cp values takes place from the minimum C_L to the maximum thus accompanying the movement of the separation line. The separation line fluctuations and pattern will be addressed in the following section.

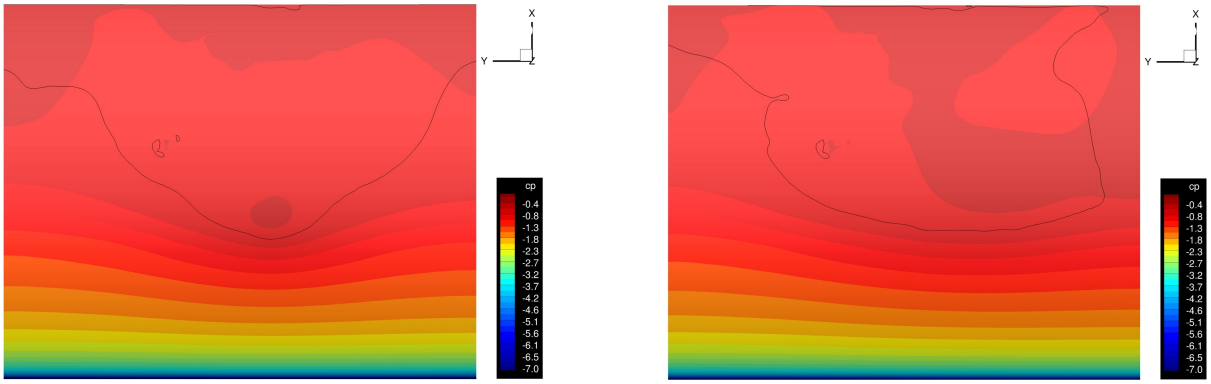

(a) $C_{L_{max}}$ (b) $C_{L_{min}}$

Figure 5.25: $C_{L_{max}}$ and $C_{L_{min}}$ Cp distributions and separation line for $\alpha = 16°$

5.2.3 Flow Separation and Stall Cells

5.2.3.1 $\alpha = 12°$

Starting with an inspection of the mean Cf_x values obtained at the last time step of the run (figure 5.26 (c)), it is clearly visible that the separation area increased in comparison with its steady counterpart, moving the maximum, at $x/c = 0.55$, closer to the one encountered in the oil flow visualization experiment ($x/c = 0.5$). However, there is still a big gap between its minimum position and the experimental one. The Cf_x distributions for the minimum and maximum C_L values obtained throughout the time series show that the biggest changes occurring are taking place on the right-hand side of the wing. This side is where the most unstable vortex is located as is shown by the displacement of its center between the maximum and minimum C_L points, falling in agreement with the Cp_{rms} values documented in the previous section. The further downstream formation of the stall cell, when compared with the experimental case, is the most likely reason for the displacement of the separation line near the wall and the consequently higher C_L values predicted.

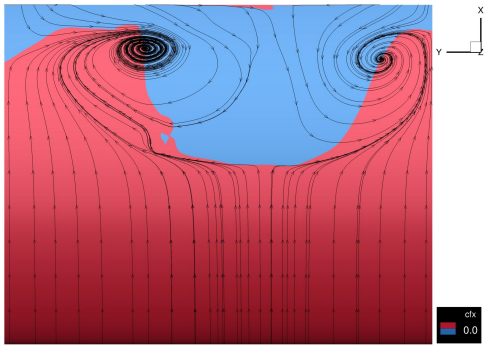

(a) $C_{L_{min}}$ at $t = 1.3129$

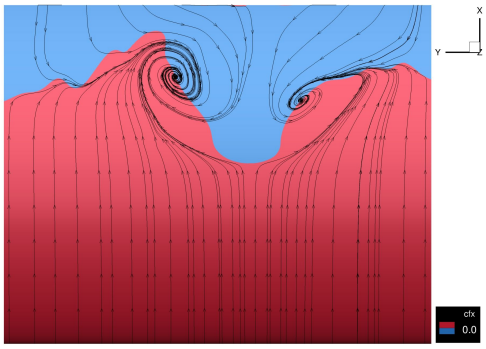

(b) $C_{L_{max}}$ at $t = 1.8088$

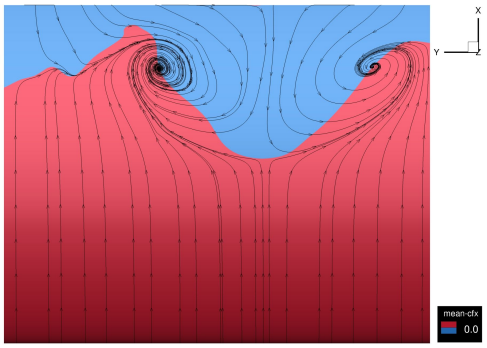

(c) Mean Cf_x

Figure 5.26: Cf_x and streamlines on suction side for $\alpha = 12°$

5.2.3.2 $\alpha = 16°$

As mentioned in the previous sections, the unsteady run for the symmetry plane/SST combination at $\alpha = 16°$ revealed a strong periodic behaviour. The separation pattern for this case is shown in 5.27 for the local maxima and minima C_L values obtained in one cycle as well as for the mean friction coefficient, $\overline{Cf_x}$, obtained at the last time step of the run. Starting with an analysis of the mean values in 5.27 (a),

the time resolving approach was able to ”eliminate” the third vortex structure captured by the steady simulation and predict the formation of the counter rotating pair of vortices in the near wall region. The shape of the separation line remains similar to a one wave pattern, as in the experiments, however, it is pushed further downstream as we move closer to walls, like in the $\alpha = 12°$ case. The maximum of the separation line is located at $x/c = 0.42$ in the midspan region, as in its steady counterpart. An inspection of the Cf_x values for the local maximum and minimum C_L points within a cycle (in (b) (c) and (d)) allows for a better understanding of the flow behaviour responsible for the pumping motion verified in the C_L value over time (figure 5.11). No distinctive differences were found in the position of the separation line maximum however, in the near wall region, the unsteady nature of the stall cell is quite visible when comparing the evolution of the vortex centres. Once the minimum value of C_L is attained, the stall cell progresses upstream while accompanying the curving of the separation line and increasing the C_L value until its maximum is reached, from where on, the inverse behaviour takes place. Although the predicted separation pattern is similar, the unsteadiness of the separation line differs from the steady like behaviour found in the experiments, manifesting itself in a more intense manner on the right-hand side of the wing, reason why the Cp_{rms} values shown in 5.20 take higher values in this area. Overall, the stall cell behaviour predicted on the wing, unlike in the experiments, pushes the separation line further downstream in the near wall region and is, like in the previous case, in part responsible for the high C_L values verified in this regime.

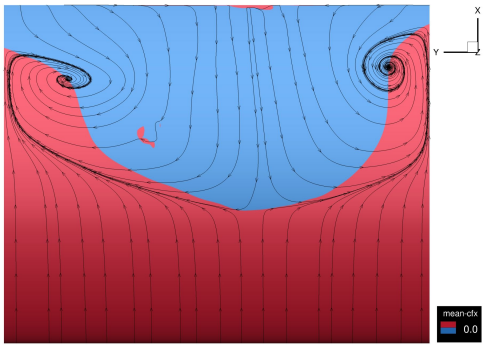

(a) Mean Cf_x

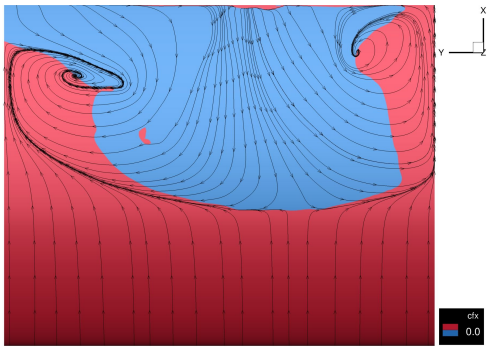

(b) $C_{L_{min}}$ at $t = 1.73185s$

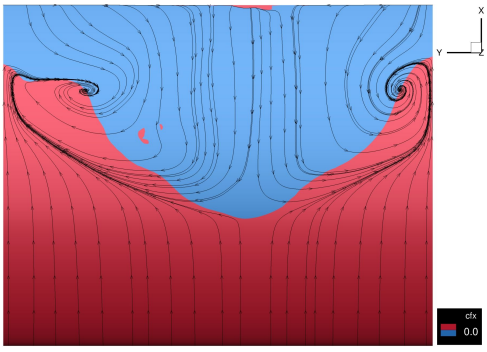

(c) $C_{L_{max}}$ at $t = 1.78885s$

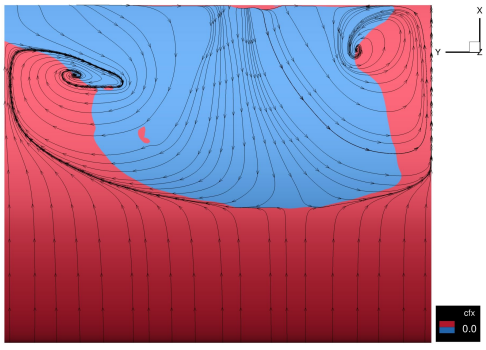

(d) $C_{L_{min}}$ at $t = 1.82495s$

Figure 5.27: Cf_x and streamlines on suction side for $\alpha = 16°$

5.2.4 Wake Velocity and Reynolds Stresses

The streamwise velocity and Reynolds stresses recorded during the wake hot-wire measurements at $\alpha = 15°$ were plotted, for each x position, together with the mean streamwise velocity ($\overline{u}$) profiles and Reynolds stresses from the unsteady symmetry plane/SST simulation at $\alpha = 16°$. For the 6 available x positions, two are located within the early shear layer, one near the trailing edge, two other in the middle part of the wake and the last one the furthest downstream. An illustration of the hot-probe positions is shown in Figure 5.28 and the results are depicted below from figures 5.29 to 5.34.

Before evaluating the results, it is necessary to keep in mind that this experimental technique is only capable of measuring absolute streamwise velocities, thus preventing a comparison within the separated flow region given that negative velocities are taken as positive. Furthermore, it should noted that the quantities obtained with URANS are ensemble averages while the ones available from the experiments were obtained by means of a time averaging method, this allows only for a qualitative analysis given the difference in the approaches.

Starting by the furthest downstream position located at $x = 0.914m$ and shown in Figure 5.29, the experiments reported a velocity deficit with a magnitude and position that could be measured and two maxima present in the profile of Reynolds stresses that were likely associated with the upper and lower shear layers that delimit the extents of the recirculation region. The numerical results, were able to predict the wake streamwise velocity peak closely at the same position as the experiments, with $y = -26.8mm$ in the experiments versus $y = -37mm$ for the numerical however, the velocity deficit was over predicted with a thinner velocity profile and stronger wake peak. In terms of Reynolds stresses, the numerical solution was able to predict the two peaks, with the stronger located closely at the same y position. The areas were the maxima of the Reynolds stresses are located, correspond to the higher velocity gradient, $\partial\overline{u}/\partial y$, in the velocity profiles, showing the outcome of a high turbulent shear. However, in quantitative terms, the numerical results show a more stable shear layer, revealing a consequence of the URANS approach in not being able to predict the smaller scale eddies present in the flow.

Moving closer to the wing and into the middle wake region in figures 5.31 and 5.30, the experiments reported that both profiles showed, the same trends as the previous one in 5.29 and this trend was followed by the numerical results, but again with a thinner, more intense wake and lower Reynolds stresses values. As in the experimental profiles, it is possible to see the wake velocity deficit recovering as the distance to the wing increases, accompanied by a consequent decrease in the streamwise Reynold stresses.

The following position at $x = 0.409m$ depicted in figure 5.32 distances $37mm$ to the trailing edge, being the closest one to it. The experimental results showed a strong velocity deficit but concluded that it was most likely outside of true backflow. However, the numerical results predicted otherwise, positioning the once again stronger wake peak in a reversed flow area. The velocity deficit recovery follows a trend similar to the experimental. Regarding the streamwise Reynolds stresses, two peaks were identified in the hot wire measurements with significant shear that was almost double as the one in the previously mentioned positions. The numerical solution managed to predict the stronger peak with a very good quantitative agreement, however this is most likely due to the reversed flow condition verified

in the numerical wake peak translating into stronger shear values thus invalidating it.

The last two positions, $x = 0.311m$ and $x = 0.211m$, shown in figures 5.33 and 5.34 respectively, are located within the early separated shear layer. The experimental profiles were reported as reasonable and the numerical ones follow similar trends from a qualitative point of view. The Reynolds stress peaks are both located in the positions where the velocity gradient, $\partial\overline{u}/\partial y$ is higher, and the numerical ones appear to be shifted by $7.5mm$ for the $x = 0.311m$ position and $12mm$ for the $x = 0.211m$ one. In comparison with the trailing edge that was addressed previously, the increase in the thickness of the shear layer is visible as reported in the experiments.

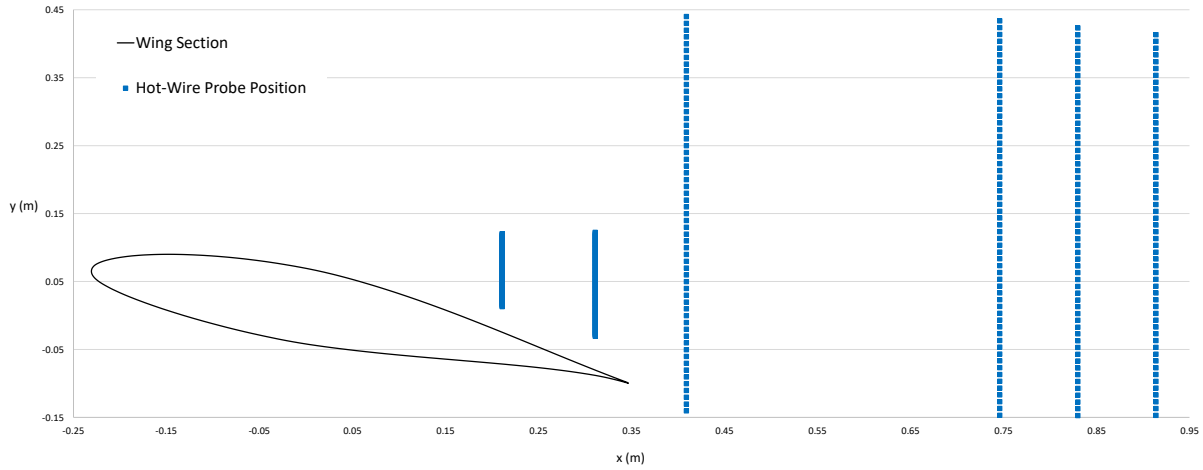

Figure 5.28: Hot-wire probe positions.

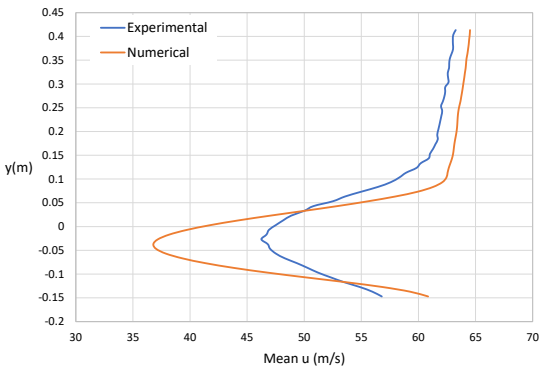

(a) $\overline{u}$

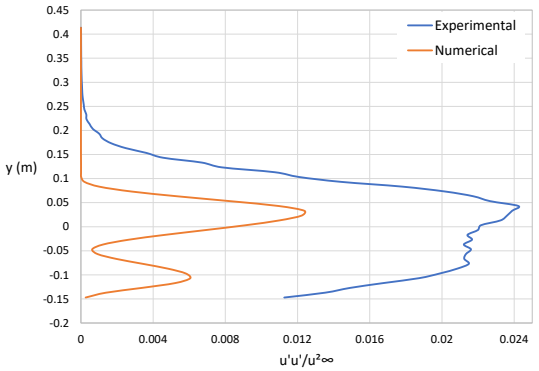

(b) $\overline{u'u'}/u_\infty^2$

Figure 5.29: Wake profiles at $x = 0.914m$

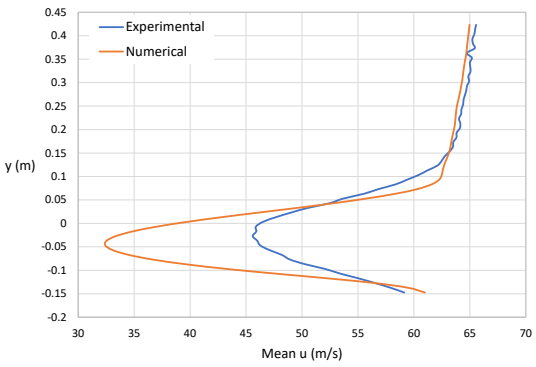

(a) $\overline{u}$

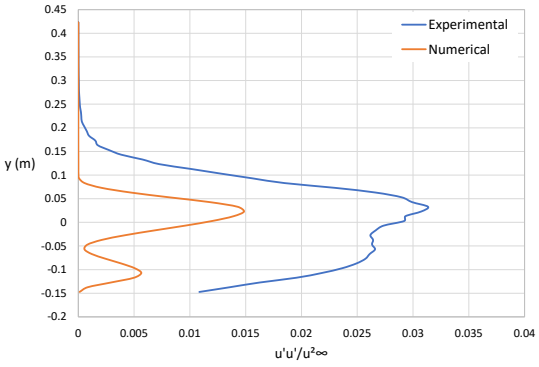

(b) $\overline{u'u'}/u_\infty^2$

Figure 5.30: Wake profiles at $x = 0.83m$

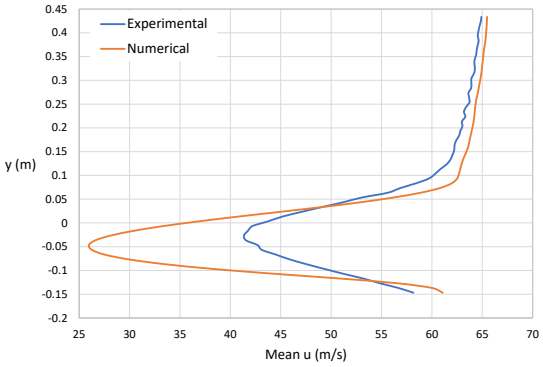

(a) $\overline{u}$

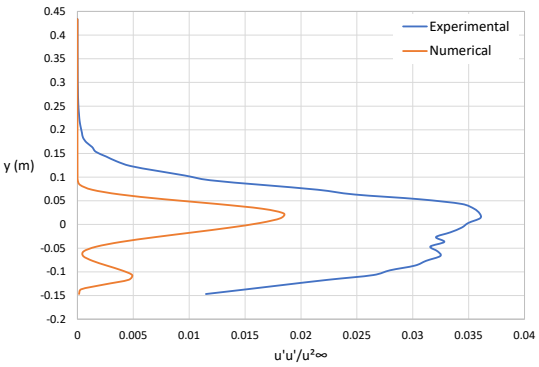

(b) $\overline{u'u'}/u_\infty^2$

Figure 5.31: Wake profiles at $x = 0.746m$

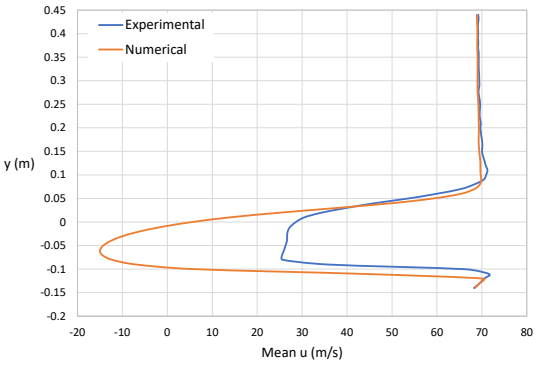

(a) $\overline{u}$

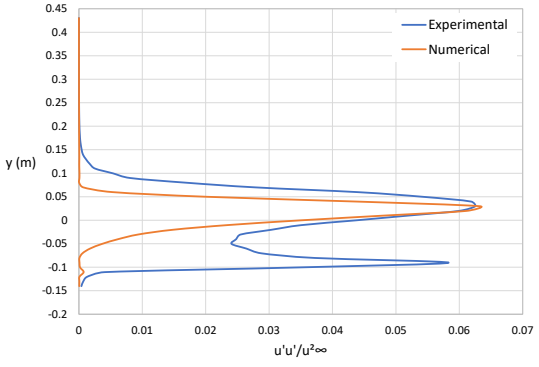

(b) $\overline{u'u'}/u_\infty^2$

Figure 5.32: Wake profiles at $x = 0.409m$

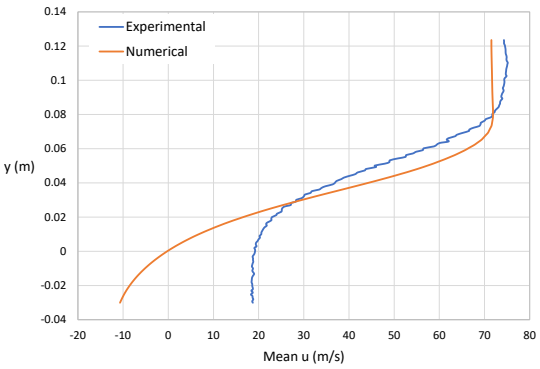

(a) $\overline{u}$

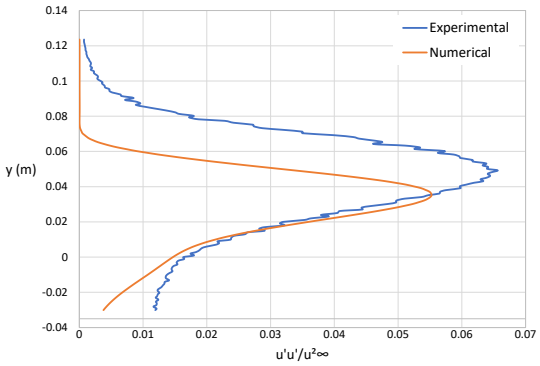

(b) $\overline{u'u'}/u_\infty^2$

Figure 5.33: Wake profiles at $x = 0.311m$

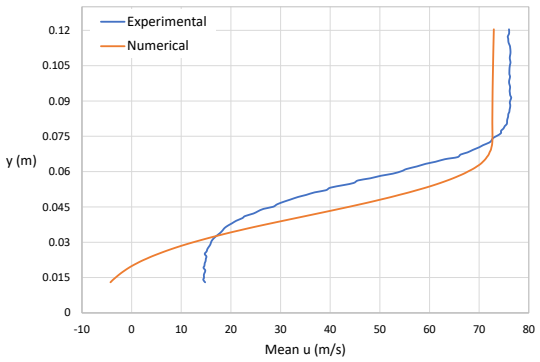

(a) $\overline{u}$

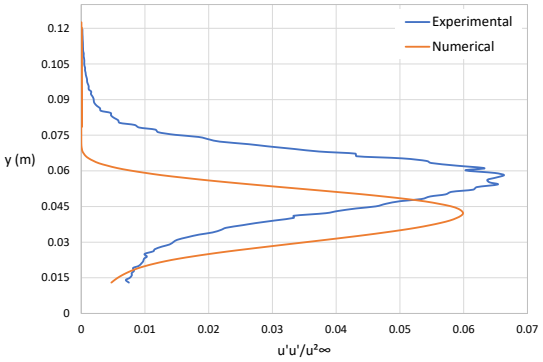

(b) $\overline{u'u'}/u_\infty^2$

Figure 5.34: Wake profiles at $x = 0.211m$

Overall, the symmetry plane/SST combination with the URANS approach showed a good qualitative agreement with the experimental results by managing to correctly predict the trends in some positions. However, in quantitative terms, the wake's intensity is overpredicted in a sense that from $x = 0.409m$ on, a sharper peak was obtained in comparison with the experiments and the reversed flow area is larger. This over prediction of the wake intensity might indicate that at those locations the numerical wake is still underdeveloped due to lower mixing with the free stream flow in comparison with the experimental one. It must be noted though, that during the hot wire measurements, strong oscillations were observed in the hot wire mount, with increased intensity as the distance to the separating shear layer on the suction side of the wing decreased. These oscillations were particularly strong for the $x = 0.211$ position and were due to the rod being moved far from its clamping point as the probe moved closer to the wing. The question then arises if the results were indeed affected by these oscillations and, if they were, how.

For illustrative purposes, the position of the maximum velocity deficit in the wake was taken for each profile and plotted. As is shown in figure 5.35, the good agreement in the prediction of the velocity profile trends is well illustrated by the evolution of the wake's maximum velocity deficit point. It must be noted that the first two points depicted $x = 0.211$ and $x = 0.311$ do not have the same meaning as the others since they are located within the early separated shear layer.

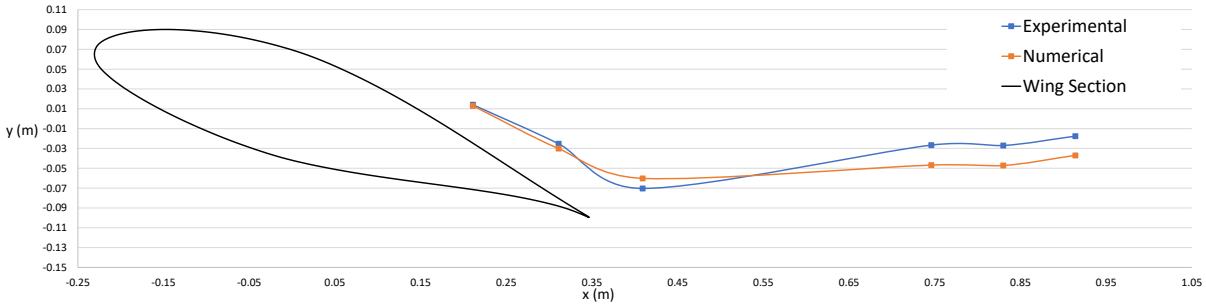

Figure 5.35: Maximum streamwise velocity deficit position.

In Figure 5.36, the normalized streamwise velocity component was plotted within a full cycle between the maximum and minimum C_L points, together with the line where $u/u_\infty = 0m/s$ (in black). From the maximum C_L point to the minimum, the maxima of the separation line is shifted from $x/c = 0.40$ to $x/c = 0.42$. The further upstream maximum of the separation line for the minimum C_L point translates into a more intense wake whose direction is shifted upwards. It is also possible to verify the large reversed flow area in the trailing edge and in the early separated shear layer that was responsible for the negative values in the mean streamwise velocity profiles from figures 5.32 to 5.34.

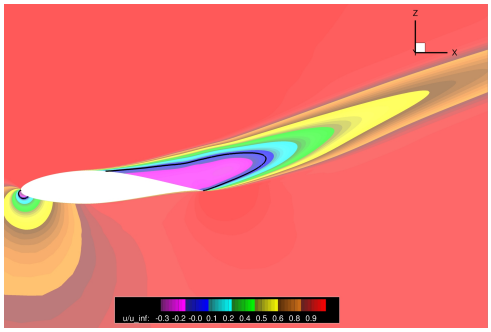

(a) $C_{L_{min}}$ at $t = 1.73185s$

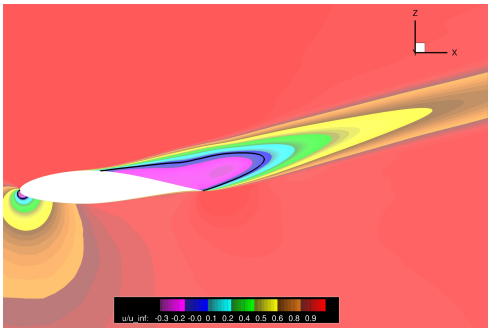

(b) $C_{L_{max}}$ at $t = 1.78885s$

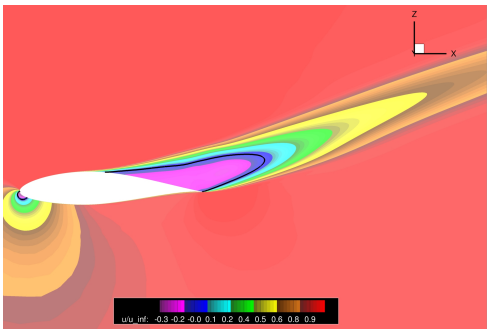

(c) $C_{L_{min}}$ at $t = 1.82495s$

Figure 5.36: u/u_∞ distribution within a cycle at midspan position.

5.2.5 Spectral Analysis

Welch's method, performed on the streamwise velocity, was used as a way to estimate the power spectral density (PSD). This approach presents some advantages in comparison with the more traditional fast Fourier transform method (FFT) given that it implements an averaging method to eliminate noise as much as possible. A consequence of this averaging is that the peaks are not as narrow as they would be when using the FFT method. In the spectral analysis performed on the experimental streamwise velocity for $\alpha = 15°$, the points were placed at $y = 0$ for the 3 hot wire locations further away from the wing, and at the vertical positions where the maximum streamwise Reynolds stresses were recorded for the measurements performed closer to the wing. It should be noted, that none of the experimental spectra was normalized. For comparison purposes, 3 points were selected to perform the same analysis on the $\alpha = 16°$ numerical case: the one furthest away from the wing at $x = 0.914m$, the one closest to the trailing edge at $x = 0.409m$ and the one further upstream within the early separated shear layer at $x = 0.211m$. The y and z positioning was set to match as closely the one from the experiments and 8800 time samples were used (from $t = 1.1001s$ to $t = 1.9361s$). The results were plotted in terms of power spectral density (PSD) over the Strouhal number (Sr). The Strouhal number is an adimensional quantity that describes oscillating flow mechanisms and is defined as:

$$Sr = \frac{fL}{U_\infty} \tag{5.1}$$

Where f is the frequency, L is the characteristic length (0.6 m) and U_∞ is the flow reference velocity ($62.9322m/s$).

The spectral analysis for the experimental data reveals in all cases a PSD plateau located in the low Sr range. Starting by the position further away from the wing and depicted in figure 5.37, the experimental results shows some peaks located in the range of $Sr = 0.96$. At the intermediate position near the trailing edge ($x = 0.409m$) depicted in figure 5.38, the experimental spectrum revealed very low frequency amplifications between $Sr = 0.01$ and $Sr = 0.05$ that were linked, most likely, to the hot wire mount oscillations verified during the experiment. In the early separated region at $x = 0.211m$ shown in figure 5.39, the experimental spectrum shows low frequency peaks again, that were linked as well with the hot wire mount oscillations. The -5/3 slope of the inertial subrange of the turbulent cascade was well captured for all the depicted experimental runs. In terms of numerical results, the PSD values take lower orders of magnitude than the experimental ones, this can correlate with the higher Reynolds stresses values captured in the experiments reflecting stronger fluctuations thus a higher PSD value. For all positions, a strong amplification was verified at $Sr = 0.10258$, that increased slightly as it moved into the early separated shear layer. This peak translates into a frequency of $10.7584Hz$ and consequently a period of approximately $\Gamma = 0.0929s$, matching the average period $\overline{\Gamma}$ verified for the cycles in the time series (figure 5.11) which is associated with the movement of the stall cells thus reflecting the dominance of this stall cell pumping motion in the flow field. The following peaks represent the 2^{nd}, 3^{rd} and 4^{th} harmonics of this amplification and slight differences can be found in the intermediate $Sr = 1$ range. The captured peak at $Sr = 0.10258$ in the numerical simulations as a result of the SC induced

pumping motion, differs from the plateau found in the experiments that, albeit revealing an elevation of the PSD in the same region, did not show any dominant frequency. This, together with the fact that an essentially stationary separation line was verified during the experiments, raises the question if weather the predicted periodic motion is realistic or not. It is also possible that, in the experiments, different low frequency phenomena that was not predicted by the numerical approach overlapped, with its superimposition resulting in the reported PSD plateau. Further, for the numerical results, as expected, the -5/3 slope of the inertial subrange of the turbulent cascaded was not captured given that some of the frequencies are filtered by URANS.

It is evident that the numerical scale of frequencies shown fall short of the ones presented by the experimental spectra. The numerical spectral analysis reveals frequencies up to approximately $Sr = 5$, being a region where the frequencies depicted most likely represent just noise thus not being within the field of interest. On the other hand, the experimental series presents values above $Sr = 100$. This difference might be associated not only with the inability of URANS to capture higher frequencies but also with the PSD method and time sampling. The larger differences in the experimental results were obtained at lower Sr values and are therefore associated with lower frequency phenomena. The time samples were collected for approximately 10 seconds while the simulation time for this case was of approximately 1.94 seconds. Thus, the experimental time series will be able to capture larger scale events than the numerical one.

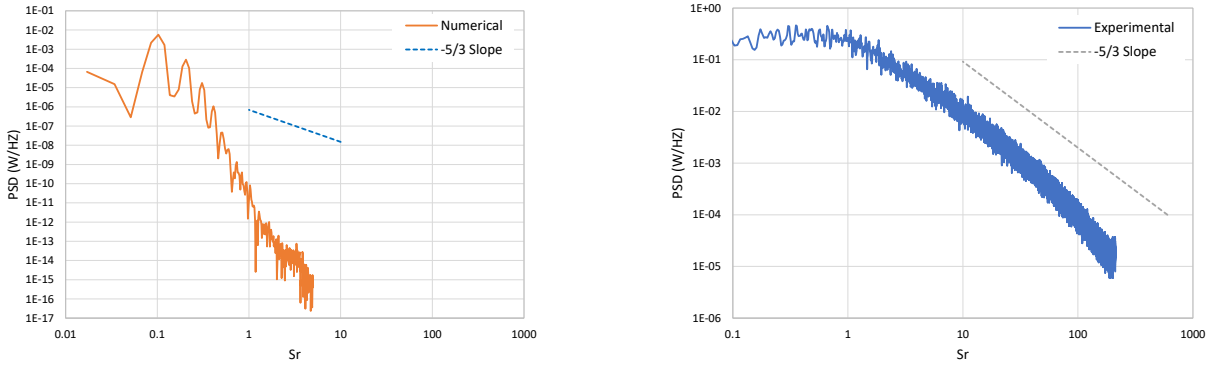

(a) (b)

Figure 5.37: PSD of the streamwise velocity at $x = 0.914m$

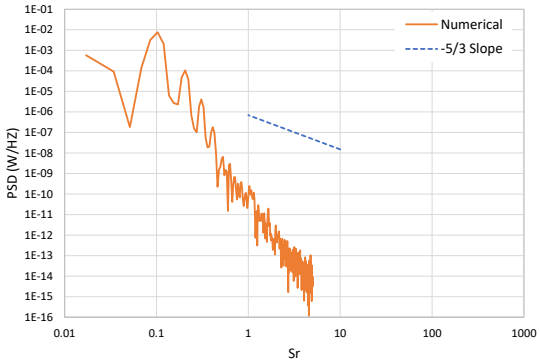

(a)

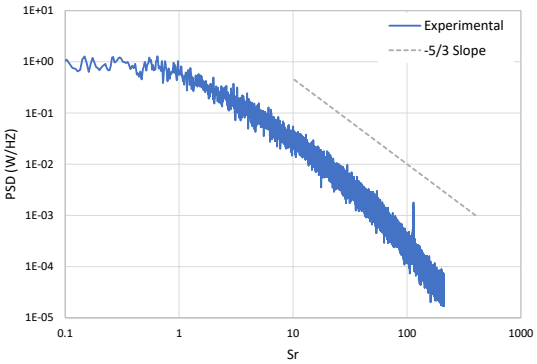

(b)

Figure 5.38: PSD of the streamwise velocity at $x = 0.409m$

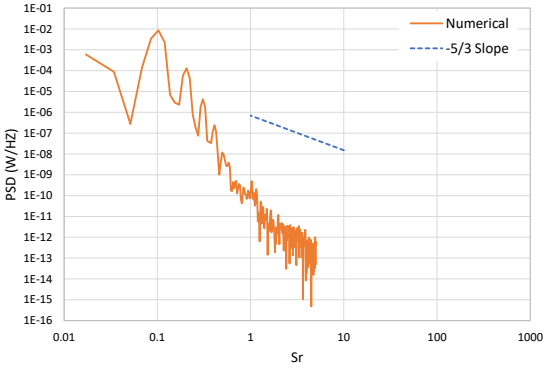

(a)

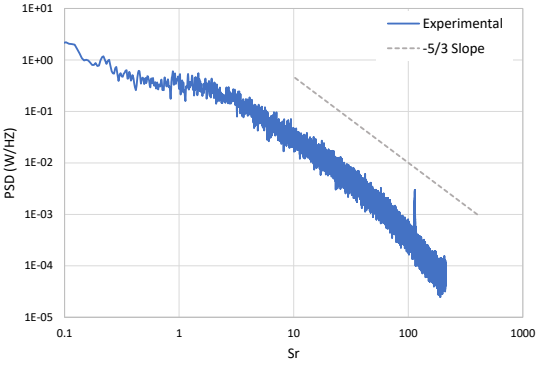

(b)

Figure 5.39: PSD of the streamwise velocity at $x = 0.211m$

For comparison purposes, a spectral analysis of the pressure coefficient was conducted for the $\alpha = 12°$ and $\alpha = 16°$ cases. The analysis was performed at the midspan position, on top of the suction side and upfront of the separation line maximum. Given the highly non periodic oscillations verified in the $\alpha = 12°$ case, it is important to understand which frequencies the URANS approach is being able to resolve in this case. The results are shown in figures 5.40 and 5.41. For both cases, as in the previous, the -5/3 slope of the inertial subrange of the turbulent flow was not captured, in part due to the same reason as in the previous cases. The range of frequencies for the $\alpha = 12°$ falls very short as well with a maximum of $Sr = 5$. This case shows an amplification peak for $Sr = 0.068$ while the $\alpha = 16°$ case has an amplification peak located at $Sr = 0.094$ with the following peaks for $\alpha = 16°$ being clearly more distinguishable. This frequency peak for the former, matches closely the average period of the SC pumping motion. In terms of energy decay, the $\alpha = 16°$ case reveals a slower decay towards the higher frequencies than the $\alpha = 12°$ one.

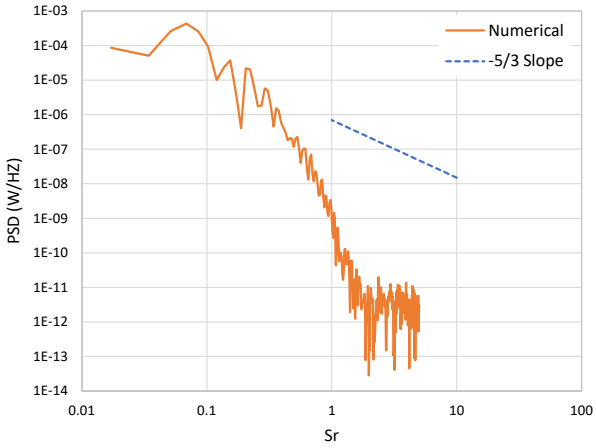

Figure 5.40: PSD of the Cp at $\alpha = 12°$.

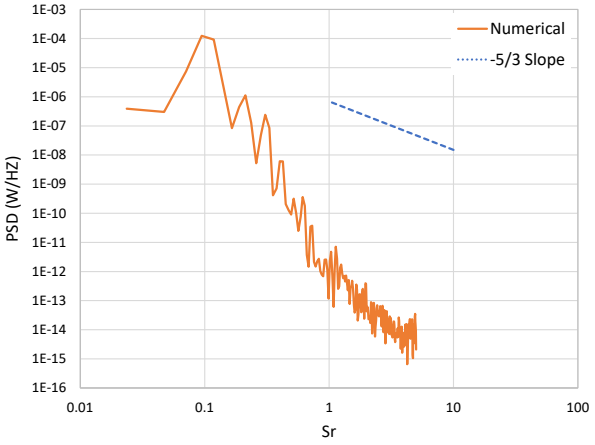

Figure 5.41: PSD of the Cp at $\alpha = 16°$.

Overall, given the oscillations captured in the low frequency range as well as the fast decay of energy towards higher frequencies (which hints at the presence of a spectral gap between resolved and modelled turbulence), it can be stated that the URANS approach is valid.

5.2.6 Time Step Evaluation

As mentioned in 4.5.4, an assessment of the time step size's suitability was performed using the results obtained from the URANS approach for the symmetry plane/SST combination with $\alpha = 16°$, and it will serve as a reference for future hybrid RANS/LES methods . The local Courant number was computed for the cells in the near wing and wake region at the midspan position and the results are depicted in Figure 5.42 below.

A first look at the figure shows two distinct areas where the Courant number exhibits higher values ($C > 3$), namely the leading edge and trailing edge areas. The leading edge region, given that it is characterized by high flow velocities related to the suction peak and attached flow, it is not an area of concern within this flow case. The trailing edge most likely exhibits such highs values due to the low grid

spacing used in this area accordingly to the Drag Prediction Workshop. Particular regions of interest for this flow case are the wake and separated shear layer regions that involve areas of resolved turbulence when using hybrid RANS/LES methods. These areas assume values approximately equal to 1 or below, indicating a good correlation between time step size and grid spacing. Some regions located in the transition between grid blocks exhibit slightly higher values of approximately $C = 2$ as does the region upstream of the separated shear layer, where $1 > C > 3$, hinting that a finer time step or an increase in grid cell size might be necessary.

Overall, a good correlation between time step and grid spacing is visible by the $C < 1$ values present in the regions of particular interest for this flow field. However, the existence of some areas with a higher Courant number in their vicinity indicates that a good approach to evaluate the time step size could be reducing it to half of its current value ($\Delta t = 4.75e^{-5}s$) and compare the results.

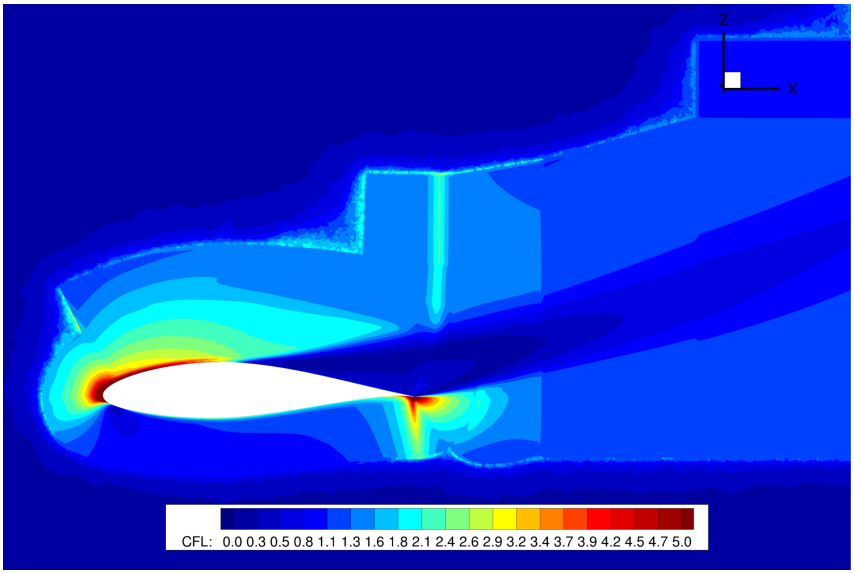

Figure 5.42: Local Courant number at midspan for symmetry plane/SST combination with $\alpha = 16°$

5.3 Remarks on Euler Walls and Viscous Walls

Due to the time frame of this work, enough investigation into some of the particularities associated with the euler walls and viscous walls boundary conditions was not possible to be performed. Thus, minimum satisfactory results that would allow a comparison with the experimental data were not able to be obtained unlike with the symmetry plane condition case. These results refer namely to the euler wall case when switching to the time resolving approach and to the viscous wall case with the initial steady approach. However, some of the results where deemed relevant enough in a sense that they might lay some fundamentals into the next steps that must be taken when using these modelling approaches and therefore they will be addressed in this section.

5.3.1 Euler Walls

An attempt to implement the combination of Euler Walls with the URANS approach using both the SST and SA model was made for the cases of $\alpha = 12°$ and $\alpha = 16°$. When using this setup, the solution, over time, reflected the absence of barely any fluctuations. When strong unsteady behaviour was expected at the highest angles of attack, this combination was unable to capture them even with a considerable simulation time. The reason for this behaviour remains unkonw, but an attempt to tackle this problem and verify the setup conditions was made by switching to a higher resolution method: hybrid RANS/LES. Applying this mode to the same conditions allowed to capture fluctuations within the flow field as depicted in figure 5.43 hinting that the damping of the solution was not a setup problem but it instead originated in the combination of the boundary condition with the turbulence model. From the beginning, the model used was URANS SST, and from around $t = 2.8s$ onwards, the flow field was solved using the hybrid method and fluctuations were captured as expected in these conditions. Although not many conclusions can be drawn from the small time series captured with the hybrid mode, it does indicate an initial better suitability of this higher resolution method when compared with URANS, in terms of capturing time dependant phenomena for this particular combination.

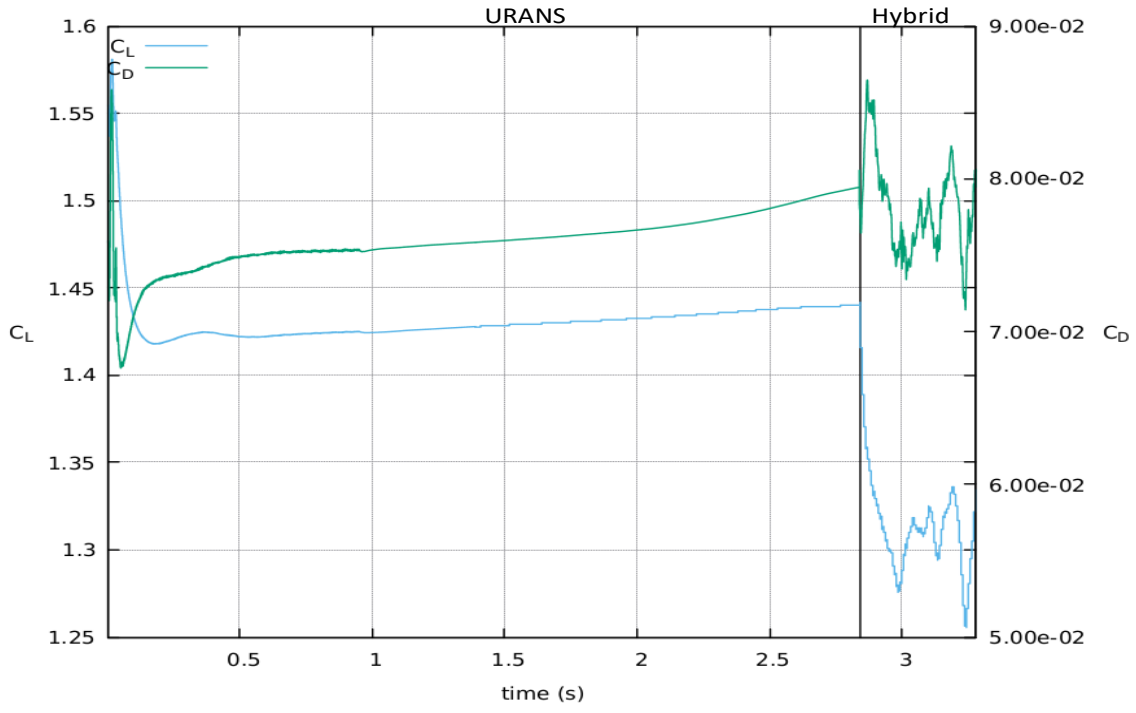

Figure 5.43: C_L and C_D over time for $\alpha = 16°$

5.3.2 Viscous Walls

As mentioned in section 4.3, different approaches were taken regarding the grid to enable the modelling of the wind tunnel walls as viscous walls. The initial approach, performed by reusing the circular shape of the domain, revealed strong convergence issues. To account for the interaction between the boundary layer on the walls and the wing, a new solver parameter was introduced, the QCR extension, which

takes into account the turbulence's anisotropy. A solution was able to be attained however, a large near wall separation area for a low angle of attack ($\alpha = 8°$) was captured, shown in figure 5.44, as the result of the interaction between the incoming wall boundary layer and the wing. The C_L value recorded was of 0.605, very low when compared with the experimental value of approximately 1.142. Thus, the importance of considering the boundary layer thickness when reaching the wing became evident, and an implementation of the estimation reported from the wind tunnel, $\delta = 30mm$ at the wind tunnel model's leading edge, was done by performing a cut on the original grid so that the inlet distance between the wall and the wing matched the distance required theoretically ($1.975m$), for the boundary layer to reach the estimated thickness. This new approach revealed strong convergence issues as well, especially when switching to a central differentiation scheme, probably due to the large cell size, and its increasing aspect ratio towards the edge of the domain, as can be seen in figure 4.1. It might also be possible, that the combination of the farfield boundary condition with a semi-circular domain caused some issues. Firstly, a refinement of the unstructured area was performed, by decreasing the cell growth ratio, but the convergence issues persisted.

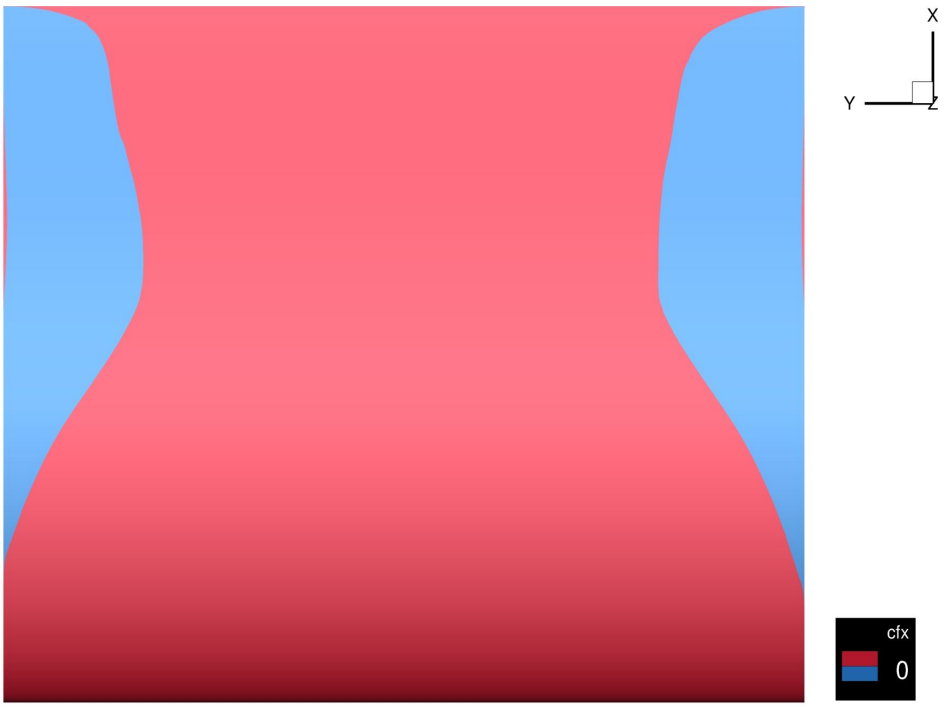

Figure 5.44: Cf_x on suction side for $\alpha = 8°$

The final approach consisted in starting by a lower angle of attack flow case ($\alpha = 5°$), reshaping the domain and using different boundary conditions at the inlet, outlet, top and bottom walls as described in section 4.3. As in the initial approach, the junction flow problem consequences between the wing and the walls is still very present by also revealing a large separated flow region in this area as depicted by the streamwise friction coefficient plotted in figure 5.45. In (a) the suction side perspective is shown and in (b) the wall's perspective at $y/b = 1$. Unlike in the experiments, the separation is still strongly influenced by the walls. An evaluation of the boundary thickness size revealed a value of approximately

$80mm$, which is quite large when compared with the estimated experimental value of $30mm$. The large separated region verified in these conditions, reflected itself on the low lift coefficient obtained of $C_L = 0.51$ when compared with the experimental of $C_L = 0.91$. However, in percentual terms, we see an improve from the original grid were the deviation to the experimental lift was approximately 47% whereas in this case it is of 43%. The assumption of fully turbulent conditions made by the model, raises the question of their suitability when dealing with this type of conditions, due to the fact that the transition from the laminar to turbulent regime is most likely taking place at a much earlier point that in real conditions. Unfortunately, there is no way to know where it is actually taking place in the experiments because no tripping methods were used as the experiments focused mainly on separation at higher angles of attack. The assumption of isotropic turbulence and modelling of the Reynolds stresses also has a strong influence in the outcome of the simulations.

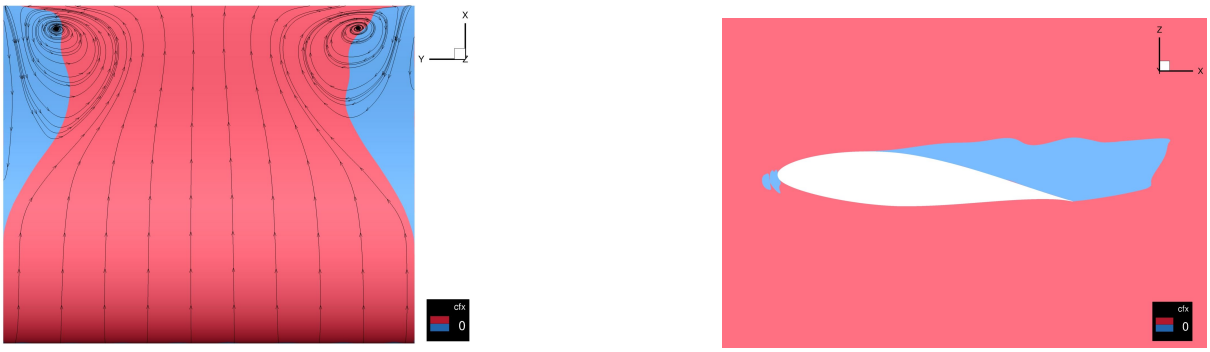

(a) Suction Side

(b) Wind Tunnel Wall

Figure 5.45: Cf_x for $\alpha = 5°$.

Although not much advancement was made in terms of the flow prediction due to the large separated region for the $\alpha = 5°$ case, the time frame of the thesis work allowed to develop a grid which enables the control of the distance from the inlet to the wing, and identify parameters which are relevant to computing this flow field. To develop the work in this case, the boundary layer resolution on the wall requires further investigation as well as its interaction with the wing. This interaction prediction might be improved with the implementation of Reynolds Stress Transport models which, unlike the RANS SST approach, directly compute the values of the Reynolds stresses.

Chapter 6

Conclusions and Recommendations for Future Work

The goal of this work was to investigate the comparability between numerical results and experimental data, and the results obtained are of interest to evaluate the performance of different boundary conditions and turbulence models implemented in the DLR TAU Code.

From the results in the previous chapter, it was observed that RANS yields very satisfying predictions for low angles of attack were flow separation is not taking place, but once the angle of attack increased to values where unsteady motion related with flow separation occurs (from $\alpha = 7^{\circ}$ and above), the results differ from the experimental ones, thus meeting trends found in [5]. However, the use of steady RANS, given its faster computation time, revealed to be a good approach in terms of parametric studies for the selection of boundary conditions and turbulence models. The most significant changes between the different boundary condition/turbulence model combination were found in the separation pattern, where the symmetry plane/Menter SST $k\omega$ combination yielded the most satisfying results as a reference for the subsequent time resolving approach.

The need of using time resolving methods when dealing with flow conditions involving large separation regions was shown by means of the increasing agreement between simulations and experiments when switching from RANS to URANS. Both the C_L values and the mean Cp distributions became closer to the experimental ones, as well as the separation pattern. The time resolving approach, particularly for the $\alpha = 16^{\circ}$ case, performed reasonably well by managing to capture a periodical flow behaviour, unlike in the $\alpha = 12^{\circ}$ one. Both cases revealed the unsteady nature of stall cells, but in the former it was possible to identify it as the reason for the pumping motion verified in the time series. The wake analysis of the flow managed to predict some of the trends in the wake streamwise velocity and Reynolds stresses profiles but revealed a strong discrepancy in quantitative terms. The spectral analysis showed the validity of the URANS approach by revealing the captured fluctuations as a low frequency behaviour and predicting a fast decay towards the higher frequencies which hints at a spectral gap between resolved and modelled turbulence. A few of the differences found are a consequence of some modelling limitations by part of the URANS approach, in which the under-predicted Reynolds stresses due to artificial

dissipation yield a more stable shear layer and a faster energy decay as was shown in sections 5.2.4 and 5.2.5 as well as its inability to capture smaller scale phenomena. Further comments can be made in the regard of possible origin for the results discrepancies. Firstly, although it might exist, it is difficult to determine the effect that starting the time resolving simulations from their steady counterparts has on the solution. In terms of time sampling, the experimental time series is approximately 5 times larger than the one that was able to be recorded for the simulations. Also, fully turbulent conditions were assumed which cause the transition point to differ from the experimental, when dealing with the lower angles of attack and consequently the model cannot as well predict the formation of the laminar separation bubble that occurs in the combination of this airfoil with these flow conditions. Overall, URANS combined with the symmetry plane/SST case, revealed itself to be useful in predicting qualitative aspects of the flows physics, namely the maximum of the separation line and its pattern, stall cell formation and wake profiles trend, but higher resolution methods are necessary to achieve a better agreement with the experimental data.

Some time consuming difficulties were encountered in combining the euler wall boundary condition with URANS and in investigating a suitable approach for modelling viscous walls as shown in section 5.3. The former case showed that URANS was unable to capture a suitable range of the flow's unsteadiness when using the euler wall boundary condition either with the SST or SA models. This problem was solved by switching to the higher resolution method hybrid RANS/LES with which fluctuations began being captured. The viscous wall case posed the particularity of having to account for the boundary layer that is formed on the walls and its interaction with the wing. Several iterations of the numerical setup were made with particular parameters of TAU revealing itself useful for this case, namely the "QCR extension". However, the junction flow condition between the walls and the wing still shows poor resolution.

Given the results found, future work on the experimental side should involve an experimental technique that allows to measure the separated flow regions, as opposed to the hot-wire technique used in this work. On the numerical side, firstly further investigation on the three dimensionality of the flow with the RANS calculations should be made with the next step being the development of the setup for the viscous walls conditions in order to bring the setup closer to the conditions found in the wind tunnel. Also the possibility of using a Reynolds Stress Transport model should be contemplated given that it directly resolves the Reynolds stresses instead of modelling them, which can be a huge advantage when dealing with the junction flow problem. At last, moving to higher resolution methods, i.e. hybrid RANS/LES as a way to deal with the frequencies that URANS cannot capture. The ability of the former method to resolve wake turbulence up to higher frequencies can present a huge advantage in terms of simulating shear layer development and the decay/breakdown of large scale eddies to small scale turbulence. The results obtained for the local Courant number suggest that investigating the time step size by decreasing it to half of the value used for this work should also be considered in order to gain a better understanding on how it effects the solution.

Bibliography

[1] A. E. Winkelman and J. B.Barlow. Flowfield Model for a Rectangular Planform Wing beyond Stall. *AIAA Journal*, 18(8):1006–1008, August 1980.

[2] D. Weihs and J. Katz. Cellular patterns in poststall flow over unswept wings. *AIAA Journal*, 21(12): 1757–1759, December 1983.

[3] D. Rodriguez and V. Theofilis. On the birth of stall cells. *Theoretical and Computational Fluid Dynamics*, 25(1–4):105–117, March 2010. doi:10.1007/s00162-010-0193-7.

[4] T. Zarutskaya and R. Arieli. On Vortical Flows Structures at Wing Stall and Beyond. In *AIAA 35th Fluid Dynamics Conference and Exhibit*, Toronto, Ontario, Canada, June 2005.

[5] M. Manolesos, G. Papadakis, and S. G. Voutsinas. Experimental and computational analysis of stall cells on rectangular wings. *Wind Energy*, 17(6):939–955, June 2014.

[6] D. Ragni and C. Ferreira. Effect of 3D stall cells on the pressure distribution of a laminar NACA64-418 wing. *Experiments in Fluids*, 57(127), July 2016.

[7] DLR Tau-Code. `https://www.dlr.de/as/desktopdefault.aspx/tabid-395/526_read-694/`. Accessed: 16-07-2020.

[8] D. Schwamborn, A. D. Gardner, H. von Geyr, A. Krumbein, H. Lüdeke, and A. Stürmer. Development of the dlr tau-code for aerospace applications. In *International Conference on Aerospace Science and Technology*, Bangalore, India, June 2008.

[9] D. Schwamborn, T. Gerhold, and R. Heinrich. The dlr tau-code: Recent applications in research and industry. In *European Conference on Computational Fluid Dynamics*, TU Delft, Delft, The Netherlands, 2006 2006.

[10] A. Jameson. Time dependent calculations using multigrid, with applications to unsteady flows past airfoils and wings. In *AIAA 10th Computational Fluid Dynamics Conference*, Honolulu, HI, USA, June 1991.

[11] J. John D. Anderson. *Computational Fluid Dynamics: The Basics With Applications*. McGraw-Hill Series in Mechanical Engineering, 1995.

[12] D. C. Wilcox. *Turbulence Modeling for CFD*. DCW Industries, Inc., 1993.

[13] *TAU-Code User Guide*. Deutsches Zentrum fur Luft- und Raumfahrt e.V - Institute of Aerodynamics and Flow Technology, release 2018.1.0 edition, July 2018.

[14] O. Reynolds. On the Dynamical Theory of Incompressible Viscous Fluids and the Determination of the Criterion. *Philosophical Transactions of the Royal Society of London*, 186(3):123–164, 1895.

[15] M. Leschziner. *Statistical Turbulence Modelling for Fluid Dynamics - Demystified: An Introductory Text for Graduate Engineering Students*. Imperial College Press, 2015.

[16] A. Favre. Equations de Gaz Turbulents Compressibles. *Journal de Mecanique*, 4(3):361–390, 1965.

[17] P. R. Spalart and S. R. Allmaras. A one-equation turbulence model for aerodynamic flows. In *AIAA 30th Aerospace Sciences Meeting and Exhibit*, Reno, NV, USA, January 1992.

[18] F. R. Menter. Zonal two equation k-ω turbulence models for aerodynamic flows. In *AIAA 24th Fluid Dynamics Conference*, Orlando, FL, USA, July 1993.

[19] W. Würz, A. Herrig, M. Kamruzzamann, and A. Ivanov. *Measurements of normal-to-wall and spanwise integral correlation lengths at the trailing edge of the NACA 643-418*. Institute of Aerodynamics and Gas Dynamics - University of Stuttgart, Pfaffenwaldring 21 D-70550 Stuttgart, Germany, January 2008.

[20] D.Althaus. Tunnel-wall corrections at the laminar wind tunnel. Technical report, Institute of Aerodynamics and gas Dynamics - University of Stuttgart, Pfaffenwaldring 21 D-70550 Stuttgart, Germany, 2003.

[21] P. R. Spalart. Young-person's guide to detached-eddy simulation grids. Contractor Report NASA/CR-2001-211032, Boeing Commercial Airplanes, Seattle, WA, USA, July 2001.

[22] 6th AIAA Cfd Drag Prediction Workshop. `https://aiaa-dpw.larc.nasa.gov/`. Accessed: 13-12-2020.

[23] L. Capsada. Simulation of atmospheric effects with the dlr code tau. Master's thesis, Universitat Politecnica de Catalunya, 2015.

[24] C. Wolf. *A Chimera Simulation Method and Detached Eddy Simulation for Vortex-Airfoil Interactions*. PhD thesis, Georg-August-Universität Göttingen, 2010.

[25] C. B. Laney. *Computational Gasdynamics*. Cambridge University Press, 1998.

Appendix A

Standard Wind Tunnel Corrections

$$K_{C_L} = (1 - 2\lambda \cdot (\sigma + \epsilon) - \sigma) \tag{A.1}$$

$$K_{C_D} = (1 - 2\lambda \cdot (\sigma + \epsilon)) \tag{A.2}$$

$$K_{C_M} = (1 - 2\lambda \cdot (\sigma + \epsilon) - \sigma) \tag{A.3}$$

$$K_{C_\alpha} = (1 + \sigma) \tag{A.4}$$

Where the constant σ regards the dimensions of the model with respect to the wind tunnel height, λ represents the shape of the pressure distribution on the model and ϵ the upstream influence on the static pressure port of the wind tunnel [19]. Table A.1 lists the values for all the constants and correction factors for the specific case of the NACA64418 airfoil.

Table A.1: Laminar Wind Tunnel corrections

λ	σ	ϵ	K_{C_L}	K_{C_D}	K_{C_M}	K_{C_α}
0.34	0.00989	-0.0012	0.9842	0.9941	0.9941	1.0099

Appendix B

TAU Parameter File - URANS

```
# TAU
Type : farfield
Markers: 0
Angle alpha (degree): 16
block end
----------------------------------

Type : viscous wall
Markers: 3
Subtype: turbulent
Name: airfoil_ps
Write surface data (0/1): 1
block end
----------------------------------

Type : viscous wall
Markers: 4
Subtype: turbulent
Name: airfoil_ss
Write surface data (0/1): 1
block end
----------------------------------

Type : viscous wall
Markers: 5
Subtype: turbulent
Name: airfoil_te
```

```
Write surface data (0/1): 1
block end
----------------------------------


Type : symmetry plane
Markers: 1
Name: symmetry_left
Write surface data (0/1): 1

block end
----------------------------------

Type : symmetry plane
Markers: 2
Name: symmetry_right
Write surface data (0/1): 1

block end
----------------------------------


Markers: 6
Type: chimera
Name: midplane
Write surface data (0/1): 1

block end
---------------------------

Markers: 7
Type: chimera
Name: midplane_ch
block end
---------------------------

Markers: 8
Type: chimera
Name: midplane_sp
```

```
block end
---------------------------


------------------------------------------------------
Required Parameters
------------------------------------------------------
Boundary mapping filename: (thisfile)
Primary grid filename: /lustre/nec/ws2/ws/iagantun-NACA64418/grid/NACA64418/grid_v4_432/NACA64418_Tau

Grid scale: 1.0
------------------------------------------------------
IO
------------------------------------------------------
Grid/Solution-------------------------------------: -
Grid prefix: /lustre/nec/ws2/ws/iagantun-NACA64418/grid/NACA64418/grid_v4_432/NACA64418_Tau_DES_v4_d
Output files prefix: sol/NACA64418_S_URANS
Controls-----------------------------------------: -
Automatic parameter update (0/1): 1
Automatic parameter update mode (0/1): 0
Accumulate queue time (0/1): 1
Write pointdata dimensionless (0/1): 0
Output level: 25
Enable logfile output on all domains (0/1): 0

Monitoring ---------------------------------------: -
Monitor history (0/1): 1
Residuals to normalize: (none)
Monitoring values: Rrho_Max-Rrho_Rrhonue_C-lift_C-drag_C-my_Max-y+_Max-eddyv_Res-lift_Res-drag
#Monitoring significant figures: 5_5_5_5_5_5

Suppress error on orphaned points (0/1): 1
Chimera new implementation (0/1): 0

------------------------------------------------------
PREPROCESSING
------------------------------------------------------

Partitioning -------------------------------------: -
```

```
Type of partitioning (name): private
Zoltan imbalance tolerance: 1.01
Zoltan partitioning approach: partition
Zoltan partitioning method: hypergraph
Use parallel initial partitioner (0/1): 0
Number of domains: 432
Number of primary grid domains: 432
Preprocessing ------------------------------------: -
Number of multigrid levels: 5
Grid metric: Cell_Vertex
Runtime optimisation ----------------------------: -
Cache-coloring (0/max_faces in color): 0
Bandwidth optimisation (0/1): 0
Compute lusgs mapping (0/1): 1
-----------------------------------------------------
SOLVER
-----------------------------------------------------
Central convective meanflow flux: Skew_symmetric_kok
Relaxation solver: Backward_Euler
Linear solver: Lusgs
Inviscid flux discretization type: Central
Central dissipation scheme: Matrix_dissipation
Upwind flux: Van_Leer
Order of upwind flux (1-2): 1
Order of additional equations (1-2): 1
Increase memory (0/1): 1
Reconstruction of gradients: Green_Gauss
Solver/Dissipation ------------------------------: -
2nd order dissipation coefficient: 0.5
Inverse 4th order dissipation coefficient: 128
Limiter freezing convergence: 0
Mach number limit for limiter: 0
Minimum artificial dissipation for acoustic waves: 0.2
Minimum artificial dissipation for velocity: 0.2

Timestepping Start/Stop -------------------------: -
Maximal time step number: 10000
Minimum residual: 1e-8
Timestep Settings -------------------------------: -
```

```
CFL number: 2
CFL number (coarse grids): 1
CFL number (large grad p): 0.9
MG-------------------------------------------: -
MG description filename: 4w
SG start up steps (fine grid): 3000
Turbulence equations use multigrid (0/1): 1
Skip dissipation update for forcing function (0/1): 0
Full multigrid ---------------------------------: -
Multigrid start level: 1
Maximal time step number (coarse grids): 100
Minimum residual (coarse grids): 0.0001
MG-Smoothing -----------------------------------: -
Residual smoother: Point_explicit
Residual smooth epsilon: 1.8
Residual smoothing steps: -3
Smoothing relaxation steps: 2
Geometry ---------------------------------------: -
Reference relation area: 0
Reference length (pitching momentum): 0.6
Reference length (rolling/yawing momentum): 0.365
Origin coordinate x: 0.15
Origin coordinate y: 0
Origin coordinate z: 0
Turbulence -------------------------------------: -



Turbulence mode: RANS
Central convective turbulence flux: Roe
Turbulence model equations eigenvalue correction: 0.15
SA boundary condition type: smooth
Version of cell stretching coefficient: HyperFlex



Turbulence model version: k-w
SA model version: Menter_SST.1994
```

```
General ratio mue-t/mue-l: 0.5
Maximum limit mue-t/mue-l: -1
Turbulent intensity: 0.001
Reference bl-thickness: 1e+22




References ------------------------------------: -
Reynolds length: 0.6
Reference temperature: 288
Reference Mach number: 0.185
Reynolds number: 2.5e+6

Unsteady Parameters----------------------------: -
Unsteady time stepping: dual
Unsteady show pseudo time steps (0/1): 1
Unsteady physical time step size: 9.5e-5
Unsteady physical time offset: 0
Unsteady computational time step size: -1
Unsteady physical time steps: 150
Unsteady inner iterations per time step: 100
Minimum number of inner iterations per time step: 100
Unsteady implicit scheme order: 2
Unsteady extrapolation order: 0
Compute harmonics of global forces (0/1..n): 0
Error for Cauchy convergence control: 1e-7

-----------------------------------------------------
eXtra field pointdata output
-----------------------------------------------------
Field output description file: (thisfile)
Field output values: cp_eddy_strain_gradu_gradv_gradw_muetmue_sa_des_Rrho_l2_volume

-----------------------------------------------------
Surface output
-----------------------------------------------------
Surface output description file: (thisfile)
```

```
Surface output values: xyz_cp_cfxyz_yplus_v_mean_variance_mean-cp_mean-cf


-----------------------------------------------------
Statistic Tool
-----------------------------------------------------
Flow time averaging ------------------------------: -
Compute flow statistics: mean_meanturb_variance
#                     Reinitialize flow averaging (0/1): 0 0 0
-----------------------------------------------------
Output period: 10000000
Surface output period: 10
-----------------------------------------------------
tau2plt
-----------------------------------------------------
Bounding Box -------------------------------------: -
Bounding x coordinate range (3D): (none)
Bounding y coordinate range (3D): (none)
Bounding z coordinate range (3D): (none)
Volume element options --------------------------: -
Volume data output (0/1): 1
Element types for zone: (none)
One zone for all volume elements: 0
Surface element options -------------------------: -
Surface data output (0/1): 1
Create surface zone for surface element: (none)
Create surface zone for boundary marker: (none)
Create one boundary: 0
Output Control ----------------------------------: -
Output format: tecplot
Ascii (0/1): 0
Precision : 9
Title of output file: (none)
Other -------------------------------------------: -
Variable list: (none)
```

Appendix C

TAU Parameter File - Viscous Wall Condition

```
# TAU
Type : euler wall
Markers: 3
Name: top_bottom_wall
Write surface data (0/1): 1
Monitor forces (0/1): 0
block end
---------------------------------

Type : viscous wall
Markers: 0
Subtype: turbulent
Name: airfoil_ps
Write surface data (0/1): 1
block end
---------------------------------

Type : viscous wall
Markers: 1
Subtype: turbulent
Name: airfoil_ss
Write surface data (0/1): 1
block end
```

```
---------------------------------

Type : viscous wall
Markers: 2
Subtype: turbulent
Name: airfoil_te
Write surface data (0/1): 1
block end
---------------------------------


Type : viscous wall
Markers: 6
Subtype: turbulent
Name: wall_left
Write surface data (0/1): 1
Monitor forces (0/1): 0

block end
---------------------------------

Type : viscous wall
Markers: 7
Subtype: turbulent
Name: wall_right
Write surface data (0/1): 1
Monitor forces (0/1): 0

block end
---------------------------------

Type : engine exhaust
Markers: 4
Name: tunnel_inlet
Engine number: 1
Monitor mass flow (0/1): 1
Write surface data (0/1): 1
Monitor forces (0/1): 0
```

```
block end
----------------------------------

Type : engine inflow
Markers: 5
Name: tunnel_outlet
Inflow condition type: Fixed_pressure
Type of mass coupling: Pressure_coupling
Regulator (0/1): 1
Relaxation factor: 0.00625
Matching iteration period: 150
Measurement coordinates: 0 0.365 6
Monitor mass flow (0/1): 1
Write surface data (0/1): 1
Monitor forces (0/1): 0


Current pressure: 97923.1

block end
----------------------------------


Markers: 8
Type: chimera
Name: midplane
Write surface data (0/1): 1

block end
----------------------------

Markers: 9
Type: chimera
Name: midplane_ch
block end
----------------------------

Markers: 10
```

```
Type: chimera
Name: midplane_sp
block end
---------------------------




-----------------------------------------------------
Required Parameters
-----------------------------------------------------
Boundary mapping filename: (thisfile)
Primary grid filename: /scratch/ws/ws1/iagantun-NACA64418/navier_stokes/grids/v6/alpha_5/scaled/NACA

Grid scale: 1.0
-----------------------------------------------------
IO
-----------------------------------------------------
Grid/Solution-------------------------------------: -
Grid prefix: /scratch/ws/ws1/iagantun-NACA64418/navier_stokes/grids/v6/alpha_5/scaled/NACA64418_NS_a
Output files prefix: sol/NS_RANS_alpha_5
Controls-----------------------------------------: -
Automatic parameter update (0/1): 1
Automatic parameter update mode (0/1): 0
Accumulate queue time (0/1): 1
Write pointdata dimensionless (0/1): 0
Output level: 25
Enable logfile output on all domains (0/1): 0

Monitoring ---------------------------------------: -
Monitor history (0/1): 1
Residuals to normalize: Density
Monitoring values: Rrho_Max-Rrho_Rrhonue_C-lift_C-drag_C-my_Max-y+_Max-eddyv_Res-lift_Res-drag
#Monitoring significant figures: 5_5_5_5_5_5

Suppress error on orphaned points (0/1): 1
Chimera new implementation (0/1): 0

-----------------------------------------------------
PREPROCESSING
```

```
-------------------------------------------------

Partitioning ------------------------------------: -
Type of partitioning (name): private #zoltan
Zoltan imbalance tolerance: 1.01
Zoltan partitioning approach: partition
Zoltan partitioning method: hypergraph
Use parallel initial partitioner (0/1): 0
Number of domains: 216
Number of primary grid domains: 216
Preprocessing -----------------------------------: -
Number of multigrid levels: 1
Grid metric: Cell_Vertex
Runtime optimisation ----------------------------: -
Cache-coloring (0/max_faces in color): 0
Bandwidth optimisation (0/1): 0
Compute lusgs mapping (0/1): 1
-------------------------------------------------
SOLVER
-------------------------------------------------
Central convective meanflow flux: Skew_symmetric_kok
Relaxation solver: Backward_Euler
Linear solver: Lusgs
Inviscid flux discretization type: Central
Central dissipation scheme: Matrix_dissipation
Upwind flux: Van_Leer
Order of upwind flux (1-2): 1
Order of additional equations (1-2): 1
Increase memory (0/1): 1
Reconstruction of gradients: Green_Gauss
Solver/Dissipation ------------------------------: -
2nd order dissipation coefficient: 0.5
Inverse 4th order dissipation coefficient: 128
Limiter freezing convergence: 0
Mach number limit for limiter: 0
Minimum artificial dissipation for acoustic waves: 0.2
Minimum artificial dissipation for velocity: 0.2

Timestepping Start/Stop -------------------------: -
```

```
Maximal time step number: 20000
Minimum residual: 1e-8
Timestep Settings ------------------------------: -
CFL number: 2
CFL number (coarse grids): 1
CFL number (large grad p): 0.9
MG-Smoothing -----------------------------------: -
Residual smoother: Point_explicit
Residual smooth epsilon: 1.8
Residual smoothing steps: -3
Smoothing relaxation steps: 2
Geometry ---------------------------------------: -
Reference relation area: 0
Reference length (pitching momentum): 0.6
Reference length (rolling/yawing momentum): 0.365
Origin coordinate x: 0.15
Origin coordinate y: 0
Origin coordinate z: 0
Turbulence -------------------------------------: -

Turbulence mode: RANS
Central convective turbulence flux: Roe
Turbulence model equations eigenvalue correction: 0.15
SA boundary condition type: smooth
Version of cell stretching coefficient: HyperFlex

QCR extension (0/1): 1



Turbulence model version: k-w
SA model version: Menter_SST.1994
General ratio mue-t/mue-l: 0.5
Maximum limit mue-t/mue-l: -1

Turbulent intensity: 0.001
Reference bl-thickness: 1e+22

References -------------------------------------: -
Reynolds length: 0.6
```

```
Reference temperature: 288

Reference Mach number: 0.185
Reynolds number: 2.5e+6
SGS Coefficient: 0.13
-----------------------------------------------------
eXtra field pointdata output
-----------------------------------------------------
Field output description file: (thisfile)
Field output values: cp_eddy_strain_gradu_gradv_gradw_muetmue_sa_des_Rrho_l2_volume #_mean_variance

-----------------------------------------------------
Surface output
-----------------------------------------------------
Surface output description file: (thisfile)
Surface output values: xyz_cp_cfxyz_yplus_v #bldelta #_mean_variance_mean-cp_mean-cf_strain_gradu_gra
-----------------------------------------------------
Output period: 100000000
Surface output period: 100000000

-----------------------------------------------------
tau2plt
-----------------------------------------------------
Bounding Box ------------------------------------: -
Bounding x coordinate range (3D): (none)
Bounding y coordinate range (3D): (none)
Bounding z coordinate range (3D): (none)
Volume element options -------------------------: -
Volume data output (0/1): 1
Element types for zone: (none)
One zone for all volume elements: 0
Surface element options ------------------------: -
Surface data output (0/1): 1
Create surface zone for surface element: (none)
Create surface zone for boundary marker: (none)
Create one boundary: 0
Output Control ---------------------------------: -
Output format: tecplot
Ascii (0/1): 0
```

```
Precision : 9
Title of output file: (none)
Other ------------------------------------------: -
Variable list: (none)
--------------------------------------------------
```

Appendix D

Data Points Location for Pressure Distributions

In chapter 3, a brief description of the pressure taps position was presented. The task of extracting the data from the computational solution precisely at the same positions for each case revealed some problems caused by the COVID-19 pandemic situation which complicated the ability to properly access the necessary software. As a mean to assess alternatives to this approach, two data sets of the pressure coefficient (Cp) distribution on the suction side were extracted. One was extracted at positions approximated by a linear regression from the most upstream and downstream experimental data points positions and the other one from a plane located at the midspan position. The results are shown in figure D.1 below.

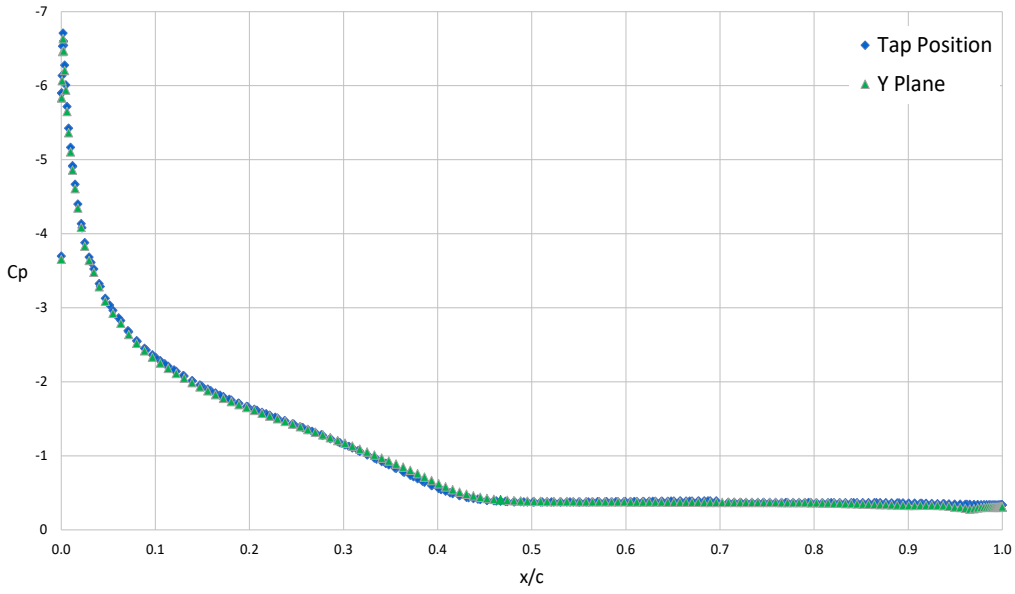

Figure D.1: Cp distribution on suction side at midspan for symmetry plane/SST case with $\alpha = 16°$

By inspection of the figure, it is clear that in terms of extracting the coefficient of pressure following an

approximate line to the one used in the experimental testing versus extracting them from a plane along the wing's midspan, the difference is barely existent. Therefore, the extraction of the Cp distribution from the numerical result was performed through the use of a y plane instead of an approximate line.